

REPORT NO.
UCB/EERC-91/07
JULY 1991

EARTHQUAKE ENGINEERING RESEARCH CENTER

ESTIMATION OF SEISMIC SOURCE PROCESSES USING STRONG MOTION ARRAY DATA

by

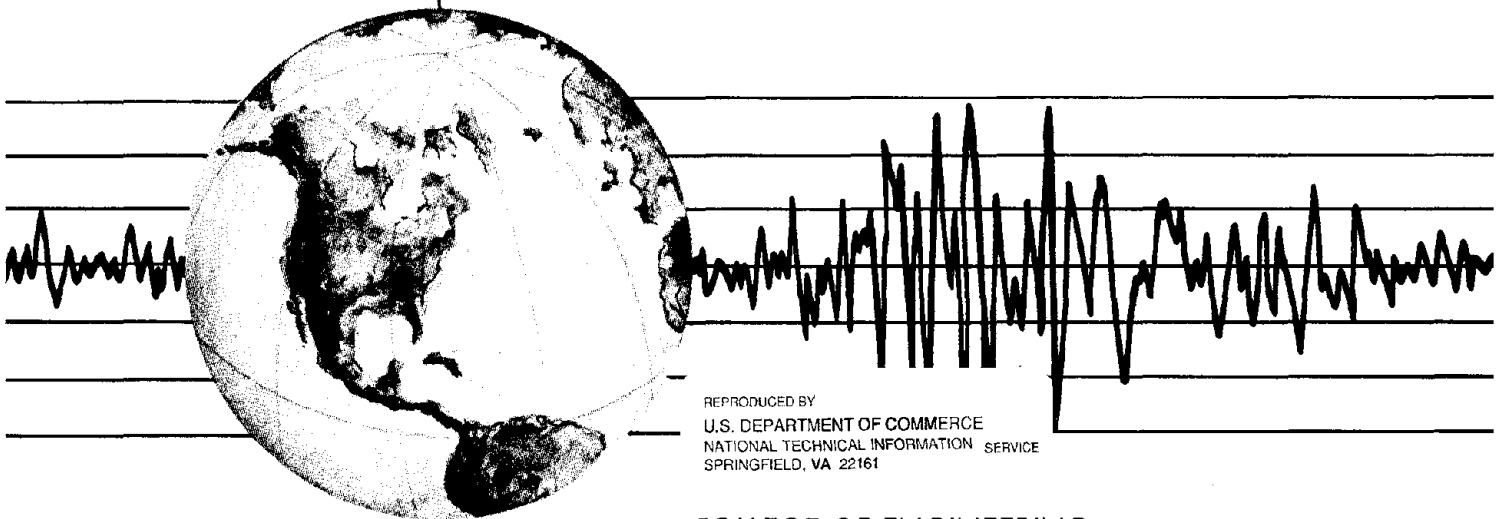
SHYH-JENG CHIOU

PREFACE

by

BRUCE A. BOLT

Report to the National Science Foundation



REPRODUCED BY
U.S. DEPARTMENT OF COMMERCE
NATIONAL TECHNICAL INFORMATION SERVICE
SPRINGFIELD, VA 22161

COLLEGE OF ENGINEERING

UNIVERSITY OF CALIFORNIA AT BERKELEY

For sale by the National Technical Information
Service, U.S. Department of Commerce, Spring-
field, Virginia 22161

See back of report for up to date listing of EERC
reports.

DISCLAIMER

Any opinions, findings, and conclusions or
recommendations expressed in this publication
are those of the author and do not necessarily
reflect the views of the National Science
Foundation or the Earthquake Engineering
Research Center, University of California at
Berkeley.

ESTIMATION OF SEISMIC SOURCE PROCESSES
USING STRONG MOTION ARRAY DATA

by

Shyh-Jeng Chiou

Preface

by

Bruce A. Bolt

Report to the National Science Foundation

Report No. UCB/EERC-91/07
Earthquake Engineering Research Center
University of California at Berkeley
Berkeley, California

July 1991

PREFACE

This study is the fifth in a series based on earthquake records from the dense array of accelerometers in Taiwan, called SMART1. Work on strong motion arrays, spatial variability of ground motion, and input for multisupport structures flourished after the large SMART1 data set started to become available after 1980.

The SMART1 array was installed in September 1980 and through June 1991 has recorded strong ground motions (with some accelerations exceeding 0.3 g) from over 55 local earthquakes. The first two reports in the series are: UCB/EERC-82/18 by B.A. Bolt, C.H. Loh, J. Penzien, Y.B. Tsai and Y.T. Yeh and UCB/EERC-85/82 by N.A. Abrahamson. In 1988, R.B. Darragh published "Analysis of Near Source Waves: Separation of Wave Types Using Strong Motion Array Recordings" in Report UCB/EERC-88/08. A research summary through 1986 was published in "Earthquake Spectra", 3, 263-287, 1987 by N.A. Abrahamson, B.A. Bolt, R.B. Darragh, J. Penzien and Y.B. Tsai. Two additional recent reports are: UCB/EERC-89/06 by Hong Hao, entitled "Effects of Spatial Variation of Ground Motions on Large Multiply-Supported Structures" and UCB/EERC-90/17 by M. Niazi, "Behavior of Peak Values and Spectral Ordinates of Near-Source Strong Ground Motion over the SMART1 Array".

The main thrust of the SMART1 research has been directed, previously, to the measurement of spatial wave fields from earthquakes of many source types, hypocentral depths, and propagation distances. The aim has been to understand more clearly the variation of amplitude, phase, and attenuation of strong ground motion with engineering applications in mind. From the beginning of the research program, another theme has been the use of arrays to map the rupture process on the fault source of each earthquake. Acoustic and electromagnetic arrays have long been steered to follow the moving energy source and it may be expected that the same utility can be made of seismic arrays. Such a mapping of the spatial and time history of the fault rupture is not only of fundamental seismological importance but also has crucial applications in engineering considerations of seismic haz-

ard. For example, in design of critical engineered structures near active faults, a realistic suite of synthetic time histories is now usually required as input motions. Confidence in such synthetics depends on clear understanding of the fault rupture process and reliable assessments of fault dislocation parameters.

In this report, Dr. Shyh-Jeng Chiou has used SMART1 array measurements to estimate the rupture pattern in a large nearby Taiwan earthquake (July 30, 1986, $M_L=6.2$). The work is important in that sources of uncertainty in such estimation are thoroughly analyzed and particular algorithms for source mapping are developed.

The research program based on the SMART1 array in Taiwan has been supported by National Science Foundation (U.S.) grants (CES 88-00457, DF 90-16813, and DMS 88-10192). Essential financial support has been forthcoming from the National Research Council (R.O.C) in Taiwan. Maintenance and operation of the array and data processing are carried out by the Institute of Earth Sciences, Academia Sinica, Taipei, and this basic work is warmly acknowledged.

B.A. Bolt

ABSTRACT

The problem of estimating fault rupture processes using seismic strong motion array data recorded at near-source distances is addressed in this report. Practical algorithms for source mapping and uncertainty assessment are developed. The parameters that define the rupture process in this study are the origin time and location of the fault rupture subevents that are responsible for the recorded near-source ground acceleration. The developed procedures are applied to the strong motion array data of the July 30, 1986 Taiwan earthquake (Event 43) recorded at the SMART1 (Strong Motion Array Taiwan, 1) array. This earthquake has a suitable magnitude (M_L 6.2) and distance (epicentral distance 7 km) for the application of array measurement of source processes using the developed theory.

The wavefield recorded at the prototype array, such as SMART1, is represented as the superposition of propagating plane waves whose horizontal slowness vectors and arrival times are functions of the subevent positions and origin times. This plane-wave assumption provides the physical model relating the source rupture-process parameters and the array recordings of wave motion generated by a moving seismic source. The slowness vectors, measured by a broad-band processing method called the Coherent Signal Subspace (CSS) method, are inverted for the source rupture times and locations by ray-tracing through a given three-dimensional crustal velocity model. The additional quantities needed in this inverse problem are the independent parameters of the crustal velocity model and fault plane, which are estimated from data independent of the strong motion array.

The array processing method CSS is shown to be more suitable for the present purpose in the following ways: (1) CSS uses phasing information in a broad frequency band to improve the slowness estimation precision; (2) first-order evaluation of the estimation uncertainties is practical; (3) CSS does not require special array symmetry.

The validity of the plane-wave model for the SMART1 recordings of Event 43 is examined critically. It is inferred that a crustal slab, with higher seismic velocity than in

the surrounding crust, underneath the array may contribute to the partial failure of the plane-wave model when applied to the complete SMART1 recordings. A subarray has to be selected which provides reliable slowness estimates. The seismic rays that travel through the proposed slab structure experience counterclockwise rotation and refraction, so they reach the free surface at different azimuths and at steeper incidence angles than those that do not travel through the slab. These results demonstrate the potentially large bias of source estimation that may occur because of unknown lateral inhomogeneities in the underlying crust.

The performance of the source mapping algorithms for Event 43 is similar to that of the traditional procedures of earthquake location using a seismographic station array with poor azimuthal coverage; the down-dip distance of the source estimate is ill-constrained and a strong correlation exists between the down-dip distance and the rupture time. The estimation uncertainties increase with the source depth, suggesting that this procedure is most suitable for shallow earthquake sources.

The level of sensitivity of the source-parameter estimates to the slowness vector and independent parameters varies with the wave type used in the inversion. The numerical results from the study of Event 43 indicate the following: (1) P-derived parameters are more susceptible to estimation errors inherent in the slowness measurements than are the S-derived parameters; (2) P-derived parameters are less sensitive to the uncertainties in the adopted crustal velocity model and fault plane; (3) for seismic waves radiated from two neighboring fault patches, the recorded P-phases at the array are more closely spaced in arrival time and wave slowness than are the S-phases. The last property suggests that an array with the capability of lower uncertainties and higher resolution for multiple P-waves is needed to attain similar precision of source estimation to that attained by multiple S-waves.

In the particular case of Event 43, the uncertainties of the independent parameters produce large systematic errors in the source-parameter estimates of individual subevents.

However, the relative subevent locations and rupture times are not subject to such large errors. The conclusion is that, based on the S-derived rupture times, the rupture of Event 43 nucleated at depth and propagated up-dip from the northeast to the southwest for a distance of about 12 km at an average rupture speed of 3.94 ± 0.23 km/sec. The differences in the P-derived rupture times are less than one standard error of the estimation and therefore do not provide a reliable estimate of the rupture speed. The estimated rupture times suggest a faster rupture speed, perhaps greater than the local shear velocity, at the deeper portion of the fault during the early stage of rupturing. The rate of rupture propagation slows down to less than the local shear velocity in the later stages of rupture.

ACKNOWLEDGMENTS

I would like to thank Professor Bruce Bolt for introducing me to strong motion seismology and for his continuous support throughout the duration of this work. I would also like to thank Professors David Brillinger and Lane Johnson for their comments.

The careful review by Ann Becker is particularly appreciated. Thanks are due to Ann Becker, Hong Hao, Nick Gregor, Michael Leonard, Anthony Lomax, and Cathy Stark, who helped me in many respects during my study at Berkeley. Special thanks to Debbie Aoki, who has always been kind and helpful. Dr. Uhrhammer provided the earthquake joint location program used in this study. The array processing code is modified from a program originally written by Dr. Norman Abrahamson. The useful information provided by Dr. Robert Darragh and Dr. K.L. Wen is greatly appreciated.

The staff in the Seismographic Station provided valuable technical support for the computers on which the numerical computations in this study were performed. The continued excellent maintenance of the SMART1 array by the Institute of Earth Sciences in Taiwan is gratefully acknowledged. This research was supported by the National Science Foundation (NSF grants CES 88-00457, FD 90-16813, and DMS 88-10192).

TABLE OF CONTENTS

Preface	i
Abstract	iii
Acknowledgements	vi
Table of Contents	vii
Chapter 1: Introduction	1
Chapter 2: Plane-Wave Model for Array Recording	9
Chapter 3: The July, 1986 Earthquake Sequence, Taiwan	14
Chapter 4: Available Strong Motion Array Data	25
4.1 Description of the SMART1 Array	25
4.2 Recorded Acceleration Data of Event 43	26
4.3 Selection of an Optimal Subarray	27
4.4 Selection of a Time Window and Alignment of Records	30
Chapter 5: Slowness Estimation from Broad-band Data	39
5.1 Coherent Signal Subspace Method	41
5.1.1 Equivalence to the Least-Squares Estimate of the Single Signal Case	46
5.2 Implementation of CSS	48
5.3 Uncertainties in Estimation	51
5.3.1 Asymptotic Mean and Covariance of Slowness Perturbation	52
5.3.2 Single Signal Case	54
Chapter 6: Estimation of the Seismic Source Rupture Process	58
6.1 Source Mapping in a Gradient-Velocity Crustal Model	58
6.2 Uncertainties of Estimation	61
6.3 The Three-Dimensional Velocity Model Adopted	61
6.4 Effects of the Basin and the Proposed Slab	62

Chapter 7: The Source Process of the July 30, 1986 Earthquake	72
7.1 Slowness Vector Estimates	72
7.1.1 S Windows	73
7.1.2 P Windows	75
7.1.3 Summary of Estimated Slowness Vectors	76
7.2 Precision of Slowness Vector Estimates	77
7.3 Estimation of the Source Parameters of the July 30, 1986 Taiwan Earthquake	77
7.3.1 Estimation Sensitivities and Uncertainties	79
7.3.2 Uncertainties Associated with Fault Strike, Dip, and Focal Depth	82
7.3.3 Uncertainties Associated with the Velocity Contrast and the Dipping Interface	83
7.4 Estimation of the Source Dimension and Rupture Speed	83
7.4.1 Source Dimension	84
7.4.2 Rupture Duration and Rupture Speed	85
Chapter 8: Summary of Results and Recommendations for Future Research	122
8.1 Summary of Results	122
8.1 Recommendations and Future Work	126
References	130

CHAPTER 1

INTRODUCTION

Understanding the mechanical processes that generate earthquakes is one of the most important fields in geophysics and geology. Considerable progress has been made since the 1906 San Francisco earthquake, which led to Reid's elastic rebound theory (1911). In this theory, the fault rupture initiates in a small region and spreads out quickly to a larger region. However, his hypothesis of a moving seismic source was not observed seismologically in a convincing way until the occurrence of the 1960 Chilean earthquake (Benioff *et al.*, 1961). Since then, studies of numerous large earthquakes at teleseismic distances have been made and the rupture speed, along with other parameters such as the rise time and the seismic moment, were recovered by matching long period seismic data to the ground motion predicted from a simple source model, such as the Haskell model. The range of rupture velocity inferred in these studies varied (see Kasahara, 1981) but most of them are less than the shear velocity at the source region.

At the near-source distance, Aki (1968) successfully modeled with a simple dislocation model the displacement record that was recorded only 80 meters from the ruptured fault that generated the 1966 Parkfield earthquake. The effects of the propagating rupture of the same Parkfield earthquake were observed at Berkeley, California (Filson and McEvilly, 1967). The estimated fault rupture velocity of the 1966 Parkfield earthquake was 2.2 km/sec. Because of the relatively long period data used, the above studies resolved only the broad, average properties of the rupture process.

The 1979 Imperial Valley seismic source generated the first large earthquake that was well recorded at both teleseismic and near-source distances. The large number of near-source ground motion records made detailed mapping of the rupture process of a large earthquake become feasible for the first time. The results clearly indicated the heteroge-

neous nature of the rupture process (Olson and Apsel, 1982; Hartzell and Heaton, 1983; Archuleta, 1984). The rupture velocity estimated by Archuleta (1984) was, on the average, 94% of the shear wave velocity, but was supershear in one segment of the fault. Using the P- and S- wave slowness data measured at a small linear array, Spudich and Cranswick (1984) found that the rupture velocity of the 1979 Imperial Valley earthquake was near the P-wave velocity over a 7 km long section of fault, and the average over the entire ruptured section was 2.7 to 3.2 km/sec.

Interest in earthquake studies is not limited only to the geophysical and geological communities. Earthquakes are also of great importance to civil engineers, who design in seismic areas critical facilities such as nuclear power plants, hospitals, large dams, bridges, and life lines. The heavy damage suffered during the 1986 Mexico earthquake and the 1989 Armenia earthquake, for example, together with documented historical earthquakes during the past thousands of years (Bolt, 1988), is clear testimony of earthquake hazards to human life and economic well-being. The relatively smaller damage during the 1989 Loma Prieta earthquake ($M_L = 7.0$) in California, which is approximately the same size as the Armenia earthquake, is a recent example of the success of modern seismically-resistant design in reducing earthquake losses. Seismology enters the risk reduction field because seismically-resistant design is critically dependent upon the near-source ground motion, needed as input for structural analysis. Recent progress in the field of strong motion seismology has provided much more confidence in the use of synthetic near-source seismograms to predict future large strong ground motions.

Indeed, the numerical prediction of site-specific strong motion records is an important task for present-day earthquake resistant design, especially while it remains true that the number of strong ground motion seismograms near a large earthquake is limited. A useful approach in such circumstance is to use a point seismic source to predict the near-source ground motion. Seismologists have, however, long recognized the important effects of source finiteness on the ground motion during a large earthquake (see Boore and Joyner,

1978; Boatwright and Boore, 1982). Yet, because there are few reliable and well-resolved source process parameters (such as the rupture velocity and the distribution of fault inhomogeneities) available, the prediction procedures and their results remain subject to close scrutiny.

A difficulty with the observational side is that reasonably high resolution is needed in measuring with confidence the basic defining properties of the earthquake source process. Fortunately, in recent years, the enhanced availability of strong motion data recorded near to the seismic source region, not only in California but in Japan, Chile, Italy, Taiwan, and elsewhere, has allowed spatial and temporal resolution of the fault rupture process of several large and moderate earthquakes. The details of such processes have provided important insights into the geological and wave generation mechanism.

The best approach to near-source seismic source studies developed over the last decade is to construct an inverse problem in which the seismic waveforms, recorded at various near-source locations are used to compute the coseismic-slip time function along the fault plane (for examples, see Olson and Apsel, 1982; Hartzell and Heaton, 1983; Archuleta, 1984; and Hartzell, 1989). Such inverse estimation not only requires heavy computation but also key *a priori* assumptions about source parameters (such as the rupture velocity) which may bias the final source image. For example, Archuleta (1984) found, through forward modeling, that the estimated slip distribution of the 1979 Imperial Valley earthquake source is sensitive to the specified value of rupture velocity. In another case, in the study of the 1984 Morgan Hill earthquake, Beroza and Spudich (1988) included rupture time as an unknown and then inverted for it directly from the observed strong motion data, along with the slip distributions. However, because the inverse problem becomes nonlinear when rupture times are unknown, iterations starting from an initial model are required. Their result is therefore model dependent.

In the studies mentioned, because relatively long period (≤ 3 Hz) ground motion records were inverted, only broad spatial averages of the rupture process can be inferred. Most

published studies to date have used widely spaced recording stations. In such cases, discrepancies between predicted and observed ground motions are to be expected because significant variations in shallow crustal properties under each receiver are not usually included in the simplified earth structure adopted. Moreover, questions of resolution and uncertainty in these source parameter estimates are not addressed in depth in any of the above mentioned studies. To my knowledge, the only detailed and systematic studies of the accuracy and the resolution of the waveform inversion approach is based on synthetic data of a homogeneous half space by Iida (1990) and Iida *et al.* (1990a,b). Because of the state of the subject, it seems valuable to explore an alternative estimation method, which involves less computation and assumptions, and which becomes feasible when recordings are available from a small strong motion array.

It is now accepted that the source process of a large earthquake is composed of a mosaic of subevents distributed over the total faulted area (e.g. see Aki, 1981). It follows from this physical concept that ground motions can be represented as a superposition of arrivals of seismic waves from each rupturing subevent. Radiated waves from different subevents may arrive almost simultaneously at a station. But under favorable conditions, such as when subevents are well separated in time and space, differences in arrival times are large enough to make them recognizable on a seismogram.

The concept of multiple events has long been used to explain multiple phases recorded from large earthquakes at teleseismic distances (e.g. Wyss and Brune, 1967; Kanamori and Stewart, 1978; Rial, 1978; Choy, 1985). At near source distances, similar inferences have been drawn. Abrahamson and Darragh (1985), for example, were able to identify paired arrivals from the 1984 Morgan Hill earthquake on a Berkeley broad-band seismogram (BKS). They interpreted these seismic wave onsets as due to two subevents. The identification of subevents of larger earthquakes by visual inspection remains, however, a difficult and hence an uncommon practice. In most cases, the receiver-subevent geometry does not guarantee well-separated arrivals such as the ones in the 1984 Morgan Hill

earthquake, and identification is ambiguous. This problem can be substantially improved by considering the phasing of the wavefield across a small, densely-spaced array. Because array analysis can, in principle, discriminate and quantify (i.e. estimate the azimuth and horizontal phase velocity) seismic wave arrivals from various subevents, it is possible to estimate the rupture time and location of each subevent after correcting for wave propagation effects. The procedure of estimating the subevent location and its rupture time is similar to the earthquake location problem which is dependent upon a small local array of seismometers.

The use of a small aperture seismic array to follow the rupture process of an earthquake was suggested in Bolt *et al.* (1982). Subsequently a number of array studies of seismic source processes has been published. Spudich and Cranswick (1984) studied the rupture process of the 1979 Imperial Valley, California earthquake based on the time delays measured by the cross-correlation between 5 elements of the linear El Centro Array that extends over a 213 meter length. Although limited by the one-dimensionality of this array, they were able to trace the rupture propagation and observe changes in rupture velocity. Spudich and Oppenheimer (1986) considered the ability of a two-dimensional array to resolve the rupture process of a hypothetical Parkfield earthquake, using synthetic data.

Abrahamson (1985), Darragh (1987), and Goldstein and Archuleta (1991b) studied the same January 5, 1981 Taiwan earthquake (M_L 6.3) recorded at the two-dimensional SMART1 (Strong Motion Array Taiwan, 1) array, using different analysis procedures and different subsets of the strong motion data. It is of interest that some key conclusions reached in these three pioneering works using SMART1 data were different. Abrahamson interpreted the observed azimuthal rotation of the position of the energy peak in the high resolution frequency-wavenumber (f-k) spectra (Capon, 1969) as due to propagation of a line-source from the southwest to the northeast and estimated the rupture speed to vary between 2.1 to 4.9 km/sec, assuming a homogeneous medium. Darragh's analysis method was different; he used the conventional f-k spectra and slowness stacking at several

frequencies. He concluded that the observed changes in computed slowness are statistically insignificant at the 90 percent confidence level. Goldstein and Archuleta (1991b) used an alternative array analysis method called MUSIC (Multiple Signal Characterization) (Schmidt, 1981, 1986; Goldstein and Archuleta, 1986) and seismogram alignment and subarray smoothing were introduced to improve the estimation. They found that the rupture of the January 5, 1981 Taiwan earthquake propagated up-dip from the northeast to the southwest. One important improvement in their study was the use of ray tracing to take into account the propagation effects of a one-dimensional earth model.

Note that the seismic source process defined in this study includes only the kinematic aspects of the fault rupture process; the source parameters estimated are the subevent locations and the subevent rupture times. Other source parameters such as the coseismic slip and stress drop along the ruptured fault were not considered.

The quantities needed for the array measurement of the source process are the wave slowness vector at the array, geometrical parameters of the fault plane (including the fault strike, fault dip, and focus), and the subsurface crustal velocity structure. The plane-wave assumption for array recording is the physical model that relates the source parameters to the wave slowness vector measured at the array through a given fault plane and crustal velocity model. In terms of the inverse estimation problem, the measured slowness vector is the 'data' and the source parameters are the 'model parameters'. The model parameters are estimated, given the assumed fault plane and crustal velocity structure, from the slowness data. There are two significant characteristics of this inverse problem. First, the solution is unique if it is assumed that rupture is confined to a fault plane, but this simple mechanism may not be correct. Secondly, the defining parameters of the geophysical model (i.e. the geometrical parameters of the fault plane and the crustal velocity model, which themselves are estimated by standard seismological methods) are not known exactly and are subject to uncertainties. The result of such errors in the assumed fault plane and crustal velocity model will be systematic errors in the source parameter estimates. In addition, there are

random errors in the source parameter estimates due to the random measurement errors of the slowness vectors.

The main objective of this report is to investigate the robustness and resolution of array measurements of source process parameters. The inversion properties are examined, using a large earthquake recorded by the SMART1 array, in terms of the accuracy, precision, and resolution of the estimated source processes, with emphasis given to the following questions: (1) the origins of the estimation error and uncertainties; (2) the resolution of the source process using P- and S- wave data independently; and finally, (3) the confidence in the estimation, given the measurement uncertainties of the adopted seismological techniques.

In Chapter 2, a formal derivation of the plane-wave model for array recording is given. The wavefield recorded at an array is, to the first-order, represented as the superposition of propagating plane waves whose horizontal slowness vector is a function of the source location and the subsurface velocity structure. In Chapter 3, the fault plane and the focus of the July 30, 1986 Taiwan earthquake are determined by the hypocentral joint location procedure and the P-wave first motion data recorded independently from the SMART1 array at regional and teleseismic distances. This earthquake has a suitable size (M_L 6.2) and distance (epicentral distance 7 km) for the array measurement of source process. The associated precision of these earthquake parameters is also estimated.

In the previous array studies of source processes, plane wave propagation was assumed but not validated in detail. In practice, the systematic deviation of the recorded wavefield from the plane-wave model is shown to produce a large systematic bias in the slowness estimation. In the first two sections of Chapter 4, the SMART1 array and the acceleration data used in this study are described. Then in §4.3, the validity of the plane-wave model for the studied earthquake is carefully examined and a SMART1 subarray within which this assumption approximately holds is selected for source process estimation. In §4.4, the general principle for the selection of time windows and the necessity of seismogram alignment are discussed.

A recent slowness estimation algorithm for broad-band data, called the Coherent Signal Subspace (CSS) (Wang and Kaveh, 1985), is described in §5.1. This algorithm effectively combines wave phasing information in a broad frequency band and thus gives a better slowness estimation performance than the conventional beamforming and high resolution method (Capon, 1969; Abrahamson and Bolt, 1987). In §5.2, some aspects of implementing the CSS method are discussed. In §5.3, the approximate first- and second -order moments of the slowness estimate are also given. In §5.3.1, for the single-signal case, the bias and covariance of the slowness estimates introduced by systematic and random phase errors are discussed in detail. A new approach to reduce the estimation bias is proposed.

In §6.1, the inverse procedure for a gradient crustal velocity model is described. A simple way to calculate the approximate covariance matrix of the source parameter estimates is given in §6.2. The effects of the alluvial basin and a crustal slab on the wavefield recorded by SMART1 array are investigated. The results demonstrate the potentially large estimation bias of the source parameters that may be introduced by the unknown heterogeneities in the crustal structure.

In Chapter 7, the procedures described in the previous chapters are applied to the SMART1 acceleration data of the July 30, 1986 Taiwan earthquake. The estimated slowness and the associated uncertainties are given in §7.1 and §7.2. The estimation errors of the source parameters are discussed in §7.3. The source dimension and rupture speed are estimated in §7.4 from the source parameter estimates in §7.3. Finally, the results of this study are summarized in Chapter 8 and future work and possible array design and improvements recommended.

CHAPTER 2

PLANE-WAVE MODEL FOR ARRAY RECORDING

In this chapter, a plane-wave model for ground motion recorded by a two-dimensional, small-aperture surface array is defined. In this model, the two-dimensional seismic wavefield is represented by the superposition of propagating plane waves, whose horizontal slowness vectors are functions of the source locations. This formulation allows the use of a model-based array-processing method to estimate the horizontal slowness vector from near-source broad-band array data. The estimated slowness vectors and observed arrival times can then be used to estimate the sequence of seismic-source locations and the rupture times.

Consider, first, seismic P-waves from an extended source. The direct, far-field P-wave displacement $u(t, \mathbf{x})$ at a point \mathbf{x} in an isotropic, inhomogeneous medium is obtained by integrating the contributions of each fault area element $d\Sigma$. The geometrical-spreading approximation for rays (Aki and Richards, 1980, p.803) then yields,

$$u(\mathbf{x}, t) = \iint_{\Sigma} \Phi(\mathbf{x}, \boldsymbol{\xi}) \dot{D}(\boldsymbol{\xi}, t - T(\mathbf{x}, \boldsymbol{\xi})) d\Sigma(\boldsymbol{\xi}). \quad (2.1)$$

Because the main interest here is in the phasing relationships of the two-dimensional wavefield recorded by the array, factors related to the radiation pattern and geometrical spreading are written collectively as $\Phi(\mathbf{x}, \boldsymbol{\xi})$. $\dot{D}(\boldsymbol{\xi}, t)$ is the slip-velocity function, $T(\mathbf{x}, \boldsymbol{\xi})$ the P-wave travel time from point $\boldsymbol{\xi}$ on the fault plane to the receiver \mathbf{x} (see Figure 2.1). The formulations for SV or SH are obtained by appropriate changes in $T(\mathbf{x}, \boldsymbol{\xi})$ and $\Phi(\mathbf{x}, \boldsymbol{\xi})$.

If the rupture time $\tau(\boldsymbol{\xi})$ is explicitly included, the slip velocity function can be rewritten as $\dot{D}(\boldsymbol{\xi}, t - \tau(\boldsymbol{\xi}) - T(\mathbf{x}, \boldsymbol{\xi}))$. The travel time $T(\mathbf{x}, \boldsymbol{\xi})$ can be further approximated to first-order by a Taylor expansion at the reference point \mathbf{x}_0 , taken at the center of the recording array,

to give

$$T(\mathbf{x}, \boldsymbol{\xi}) = T(\mathbf{x}_0, \boldsymbol{\xi}) + \mathbf{S}(\boldsymbol{\xi}) \cdot (\mathbf{x} - \mathbf{x}_0), \quad (2.2)$$

where $\mathbf{S}(\boldsymbol{\xi})$ is the travel-time gradient evaluated at \mathbf{x}_0 , and, by definition (Bullen and Bolt, 1985), is the ray horizontal slowness vector at \mathbf{x}_0 . The above approximation (2.2) is valid only when the spacing between array sensors is small enough to ensure that ray paths to each station sample the same heterogeneities in the Earth model and the higher-order terms of the Taylor expansion can be neglected. Substitution of (2.2) into (2.1) yields,

$$\mathbf{u}(\mathbf{x}, t) = \iint_{\Sigma} \Phi(\mathbf{x}, \boldsymbol{\xi}) \dot{D}(\boldsymbol{\xi}, t - \tau(\boldsymbol{\xi}) - T(\mathbf{x}_0, \boldsymbol{\xi}) - \mathbf{S}(\boldsymbol{\xi}) \cdot (\mathbf{x} - \mathbf{x}_0)) d\Sigma(\boldsymbol{\xi}). \quad (2.3)$$

We assume that the coseismic slip is distributed inhomogeneously over the faulted area and that the wavefield at the array is the sum of the seismic radiation from a mosaic of patches. This assumption allows a further approximation of (2.3) by summing a sequence of surface integrals over sub-elements, so that

$$\mathbf{u}(\mathbf{x}, t) = \sum_j \iint_{\Sigma_j} \Phi(\mathbf{x}, \boldsymbol{\xi}) \dot{D}(\boldsymbol{\xi}, t - \tau(\boldsymbol{\xi}) - T(\mathbf{x}_0, \boldsymbol{\xi}) - \mathbf{S}(\boldsymbol{\xi}) \cdot (\mathbf{x} - \mathbf{x}_0)) d\Sigma(\boldsymbol{\xi}). \quad (2.4)$$

If Σ_i is sufficiently small so that the integrands in (2.4) are approximately independent of $\boldsymbol{\xi}$ in each Σ_i , then (2.4) can be written as

$$\mathbf{u}(\mathbf{x}, t) = \sum_{j=1}^N \Phi(\mathbf{x}, \boldsymbol{\xi}_j) \dot{D}(\boldsymbol{\xi}_j, t - \tau(\boldsymbol{\xi}_j) - T(\mathbf{x}_0, \boldsymbol{\xi}_j) - \mathbf{S}(\boldsymbol{\xi}_j) \cdot (\mathbf{x} - \mathbf{x}_0)) \Sigma_j, \quad (2.5)$$

where $\boldsymbol{\xi}_i$ is the position vector at the center of Σ_i .

By (2.5), the P-wave far-field displacement is expressed as the superposition of N plane waves with slowness vectors $\mathbf{S}(\boldsymbol{\xi}_i)$, $i = 1, \dots, N$. $\mathbf{S}(\boldsymbol{\xi}_i)$ is measurable by standard array processing methods such as conventional beamforming (CV), or the high resolution method (Capon, 1969).

In the frequency domain, the Fourier coefficient of (2.5) at sensor \mathbf{x}_i and frequency ω_k is

$$\mathbf{u}(\mathbf{x}_i, \omega_k) = \sum_{j=1}^N \Phi(\xi_j) \dot{D}(\omega_k, \xi_j) e^{-i\omega_k(\tau(\xi_j) + T(\xi_j, \mathbf{x}_0) + \mathbf{S}(\xi_j) \cdot (\mathbf{x}_i - \mathbf{x}_0))} + \mathbf{n}(\mathbf{x}_i, \omega_k), \quad (2.6)$$

where $i = 1, \dots, M$, and M is the number of sensors. The last term in (2.6), \mathbf{n} , represents the recorded background noise. In (2.6) it is assumed that $\Phi(\xi_j, \mathbf{x}_i)$ does not vary significantly across the array sensors; hence its dependence on \mathbf{x}_i is dropped. Although this is not a good assumption when the source radiation pattern at ξ_i happens to have a nodal line close to the array, the seismogram normalization procedure described in §4.3 would effectively reduce the resulting spatial variation in ground motion. pattern.

Because this model is based on ray theory, it is more suitable for high frequency wave data. Although given in terms of displacement, equation (2.6) is applicable also to acceleration data, except for a multiplication of $-\omega_k^2$ to account for the second derivative with respect to time. It should be noted that such multiplication does not alter the phasing relationships and, hence, the values of $\mathbf{S}(\xi_i)$. The isochrone formalism used in the ground motion calculation by Spudich and Frazer (1984), which is also a ray method, provides a physical interpretation of the generation of high-frequency accelerations. It was shown by Spudich and Frazer that large-amplitude ground acceleration may be related to the spatial variations of slip velocity (or stress drop) and rupture speed.

The equation (2.6) is adopted here as the forward model for the array recording of near-source ground motion due to a moving seismic source. For the inverse problem, i.e. the estimation of the source positions ξ_i and rupture time $\tau(\xi_i)$, a seismic ray with the horizontal slowness vector opposite to the array-measured slowness vector is drawn from the array center \mathbf{x}_0 . The intersection of this ray with the fault plane Σ gives the source position ξ_i . The rupture time $\tau(\xi_i)$ is evaluated by subtracting the travel time $T(\mathbf{x}, \xi_i)$ from the observed arrival time.

In the above plane-wave model, horizontal slowness vectors $\{\mathbf{S}(\xi_i), i = 1, \dots, N\}$ are a

function of the source positions $\{\xi_i, i = 1, \dots, N\}$ as well as the subsurface velocity structure through which seismic rays traveled. In practice, due to the lateral heterogeneities in the Earth model and the proximity to the fault plane, the measured slowness vector may be a function of array position x_0 also (Capon, 1974). Therefore, the plane-wave model of (2.6) may be not valid for a large aperture array. In § 4.3, the validity of this plane-wave model for the SMART1 array will be examined in detail and an approach which minimizes the effects of small perturbations from the plane-wave model will be proposed in § 5.3.2.

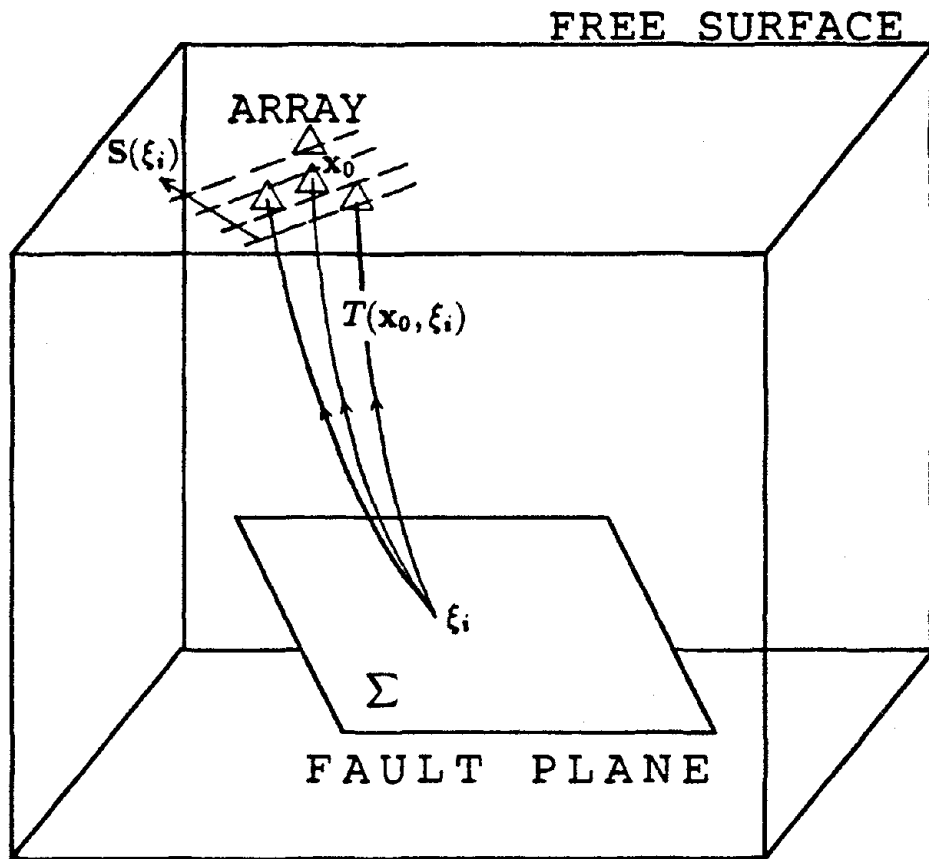


Figure 2.1 Plane wave model for the wavefield recorded by an array. See text for symbols.

CHAPTER 3

THE JULY, 1986 EARTHQUAKE SEQUENCE, TAIWAN

A sequence of earthquakes occurred during the months of July and August, 1986, in northeastern Taiwan. The epicentral area is located at the southern part of an alluvial basin (Ilan plain) (see Figure 4.2). Although the tectonic history of this basin is still not fully understood, one explanation is that it is a spreading basin which is the western extension of the south Okinawa Trough (Yeh *et al.*, 1989). No fault lines are mapped in the epicentral area. However, the extension of the Sanhsing fault (Figure 4.2), which is mapped as a reverse fault (Chiang, 1976), would go into the epicentral area.

In July, 521 events of the sequence were reported by the Earth Sciences Institute, Academia Sinica, in Taiwan. Twenty-seven of them had $M_L \geq 4.0$. The mainshock was $M_L = 6.2$. The magnitudes and moment of the mainshock given in the ISC (International Seismological Centre) bulletin are $m_b = 5.6$, $M_S = 5.6$, $M_o = 2.2 \times 10^{17}$ Nm. This earthquake sequence consisted of three separate groups of activity with the mainshock in the last group (Figure 3.1). Few foreshocks were detected 24 hours immediately before the mainshock. The three largest events triggered the nearby SMART1 (Strong Motion Array Taiwan, No. 1) and LSST (Large Scale Seismic Test) strong motion arrays (see §4.1 for description). The mainshock will be referred to as Event 43 in the subsequent chapters consistent with the SMART1 convention of numbering of recorded events (Table 4.1).

Joint Location. Before the array-based source-process mapping is commenced it is crucial to fix as accurately as possible the orientation and location of the fault plane of Event 43. The first line of evidence comes from the foreshock-aftershock distribution. Using arrival-time data from the local TTSN network (Taiwan Telemetered Seismographic Network), sixteen well-recorded earthquakes in the sequence (eight of which also triggered

the LSSST array) were jointly located (Canas *et al.*, 1977). Figure 3.2 shows the distribution of stations used in the location. Each TTSN station is equipped with a vertical Mark L-4C or Kinematics SS-1 vertical sensor. S readings from only three stations, TWC, TWE and TWZ, were used in the locations. In addition, P and S arrival times, if available, at the LSSST array were also used. Station corrections and perturbations to the initial velocity models were included as unknown parameters in the joint location routine (Canas *et al.*, 1977). The adopted velocity model consisted of a gradient crustal layer over a homogeneous half space with initial properties chosen from the velocity model used for routine earthquake location by TTSN.

Hypocentral locations and origin times, together with their standard errors, of the jointly located events are listed in Table 3.1. The estimated velocity model (Table 3.2) is assumed to be representative of the average crustal structure in the area covered by the TTSN stations used in the joint location. This gradient-velocity model is plotted in Figure 3.3, together with velocity profiles extracted from the 3-D velocity model constructed by the inversion of travel-time data (Yeh, 1987). The velocity gradient obtained in this study agrees with that suggested by Yeh's model, which consisted of homogeneous velocity cells. Compared with the variation of velocity in the 3-D velocity model (Figure 3.3) of the epicentral region, the standard error of the estimated velocity gradient in this study is probably overestimated. This overestimation of the velocity gradient is probably an expression of the large variation of the seismic velocity within the area covered by the TTSN stations used in the joint location.

The hypocenters of the remaining earthquakes in the sequence were located individually using the station corrections and velocity model obtained from the joint location. The epicentral distribution of events, with $M_L \geq 3.0$ and location standard error less than 5.0 km, is shown in Figure 3.4. A lineation in the epicentral distribution consistent with the hypothesis of a fault plane dipping to the east is apparent. The hypocentral distribution along the profile A-A' (perpendicular to the linear trend) is shown in Figure 3.5.

Fault Plane Orientations. The second line of evidence on fault plane orientation is provided by a first-motion fault-plane analysis. The fault-plane solution for the mainshock is based on the P-wave first motion data at both local and teleseismic distances. The computation (Figure 3.6) is performed by the method of Brillinger *et al.* (1980). The result indicates, as one alternative, normal faulting with a strike of $N65.1^{\circ}E \pm 8.2^{\circ}$ and a dip of $60.2^{\circ}SE \pm 8.3^{\circ}$. These values agree, within the standard errors, with the planar trend of the distribution of foreshock-aftershock hypocenters. It thus seems reasonable to adopt this orientation in the following discussion rather than that of the orthogonal plane.

Table 3.1

Earthquake Parameters									
	Origin Time (UTC)	Latitude	S.E.†	Longitude	S.E.	Depth	S.E.	M_D	M_L
1	86/07/11 18:25:25.2	24°37.09' N	0.6	121°48.57' E	0.7	10.7	3.0	3.7	4.5
2	86/07/16 23:50:30.8	24°36.90' N	0.6	121°48.54' E	0.9	10.1	3.4	3.7	4.5
3	86/07/16 23:55:13.0	24°37.59' N	0.7	121°48.91' E	0.7	9.3	3.9	3.7	4.5
4	86/07/16 23:57:30.9	24°37.95' N	0.6	121°49.12' E	0.9	11.3	3.4	3.7	4.5
5	86/07/17 00:03:31.9	24°37.14' N	0.6	121°49.02' E	0.6	11.9	2.7	4.2	5.0
6	86/07/27 22:49:56.8	24°31.63' N	0.9	121°57.48' E	1.7	19.3	3.3	4.2	4.9
7	86/07/30 06:34:33.6	24°38.09' N	0.6	121°48.33' E	0.6	11.0	3.1	3.1	3.9
9	86/07/30 11:31:46.4	24°36.73' N	0.5	121°48.88' E	0.4	9.7	3.4	5.5	6.2
8	86/07/30 11:38:30.7	24°37.53' N	0.5	121°48.09' E	0.8	9.2	3.7	4.9	4.9
10	86/07/30 12:29:23.2	24°37.01' N	0.6	121°48.23' E	1.1	7.8	4.3	3.4	4.3
11	86/07/30 14:57:13.7	24°36.22' N	0.5	121°45.84' E	0.6	8.1	4.6	3.7	4.5
12	86/07/30 15:14:38.1	24°35.44' N	0.6	121°44.64' E	0.5	8.4	4.4	2.9	3.8
13	86/07/31 01:53:26.6	24°34.87' N	0.9	121°44.77' E	0.5	8.4	4.7	3.2	4.0
14	86/07/31 17:41:27.8	24°36.77' N	0.7	121°48.34' E	0.8	9.4	3.5	3.3	4.2
15	86/07/31 23:54:03.9	24°37.15' N	0.6	121°48.67' E	0.8	8.9	3.7	3.7	4.5
16	86/08/05 00:56:22.5	24°36.57' N	0.5	121°47.04' E	0.7	9.0	3.9	4.1	4.9

†: Standard error in km.

M_D is determined by the Institute of Earth Sciences, Taipei, Taiwan.

M_L is determined from the equation $M_L = (1.04 + 0.94M_D) \pm 0.28$.

Table 3.2

VELOCITY MODEL			
P-wave		S-wave	
a	b	a	b
(km/sec)	(1/sec)	(km/sec)	(1/sec)
5.050±1.000	.060±0.067	2.954±0.346	.038±0.029

$V = a + b \times z$, for $z \leq$ crustal thickness

a = surface velocity

b = velocity gradient

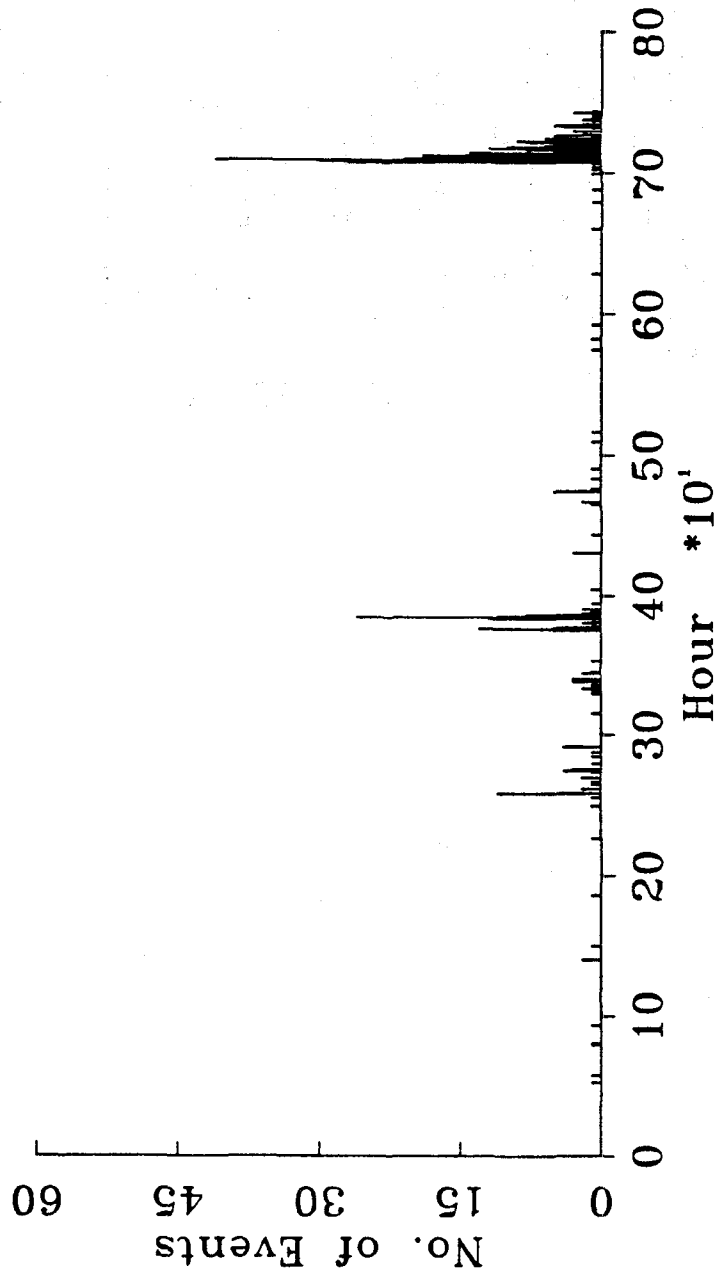


Figure 3.1 Number of events per hour during the July, 1986 sequence, Taiwan.

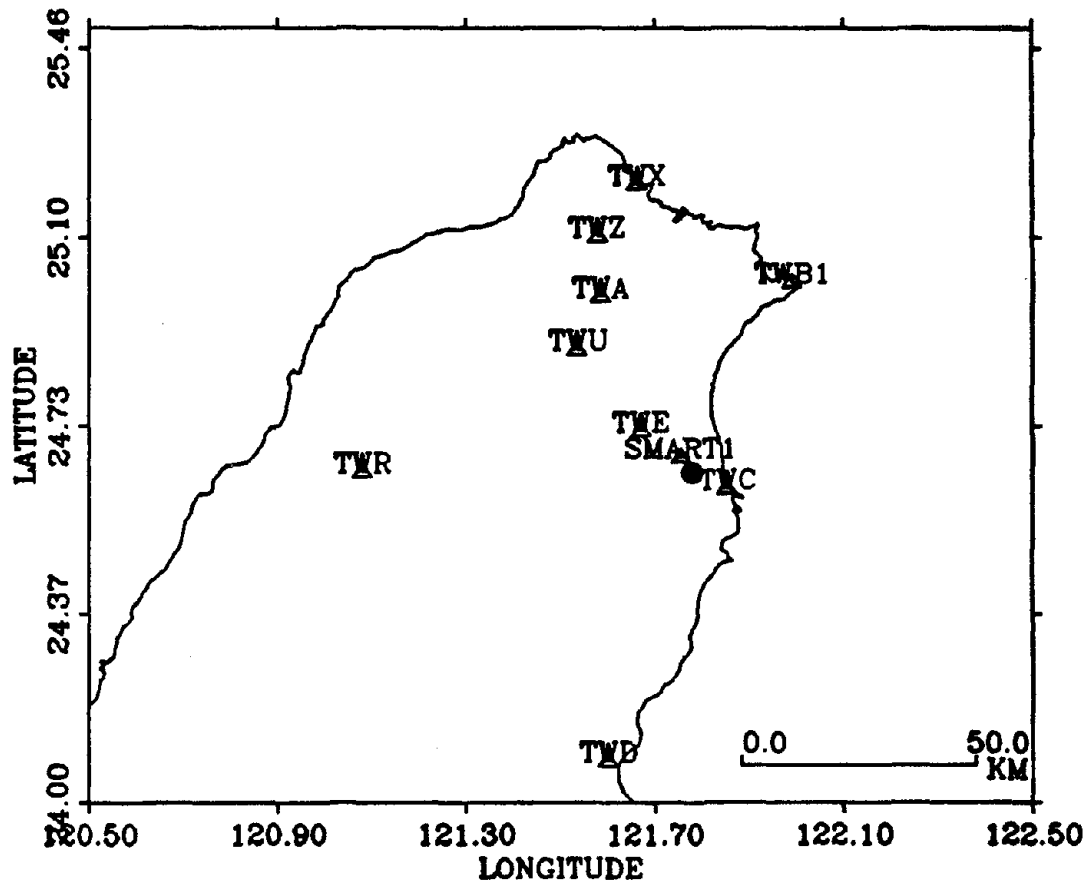


Figure 3.2 Stations used in joint location. The solid circle denotes the epicenter of the July 30, 1986 Taiwan earthquake.

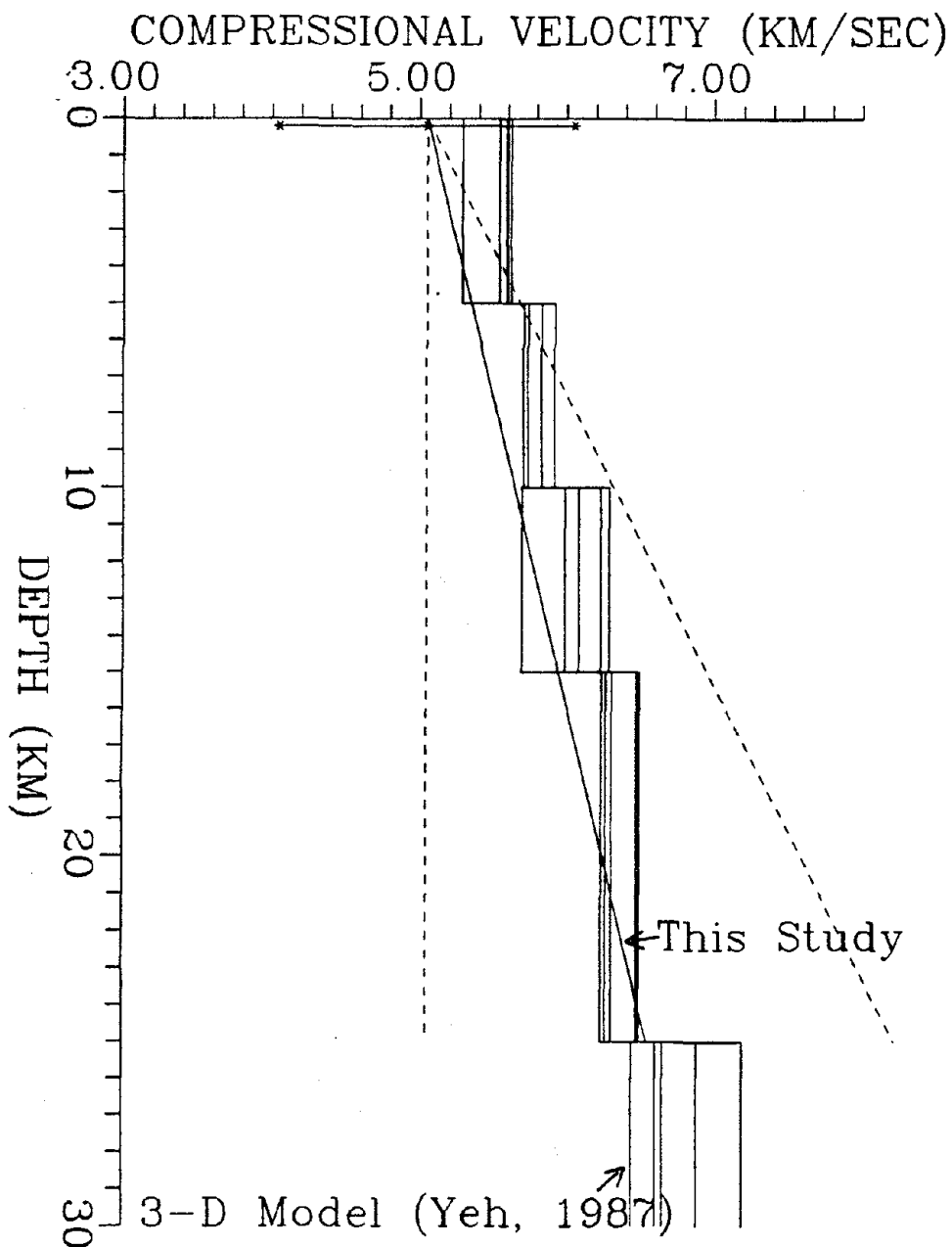


Figure 3.3 (a) Crustal P-velocity model. The solid straight line is the gradient-velocity model inferred from joint location. The two dashed lines indicate the standard error of the velocity gradient. The horizontal bar denotes the standard error of the surface velocity. Also shown in this figure are the P-velocities extracted from the 3-D model of Yeh (1987).

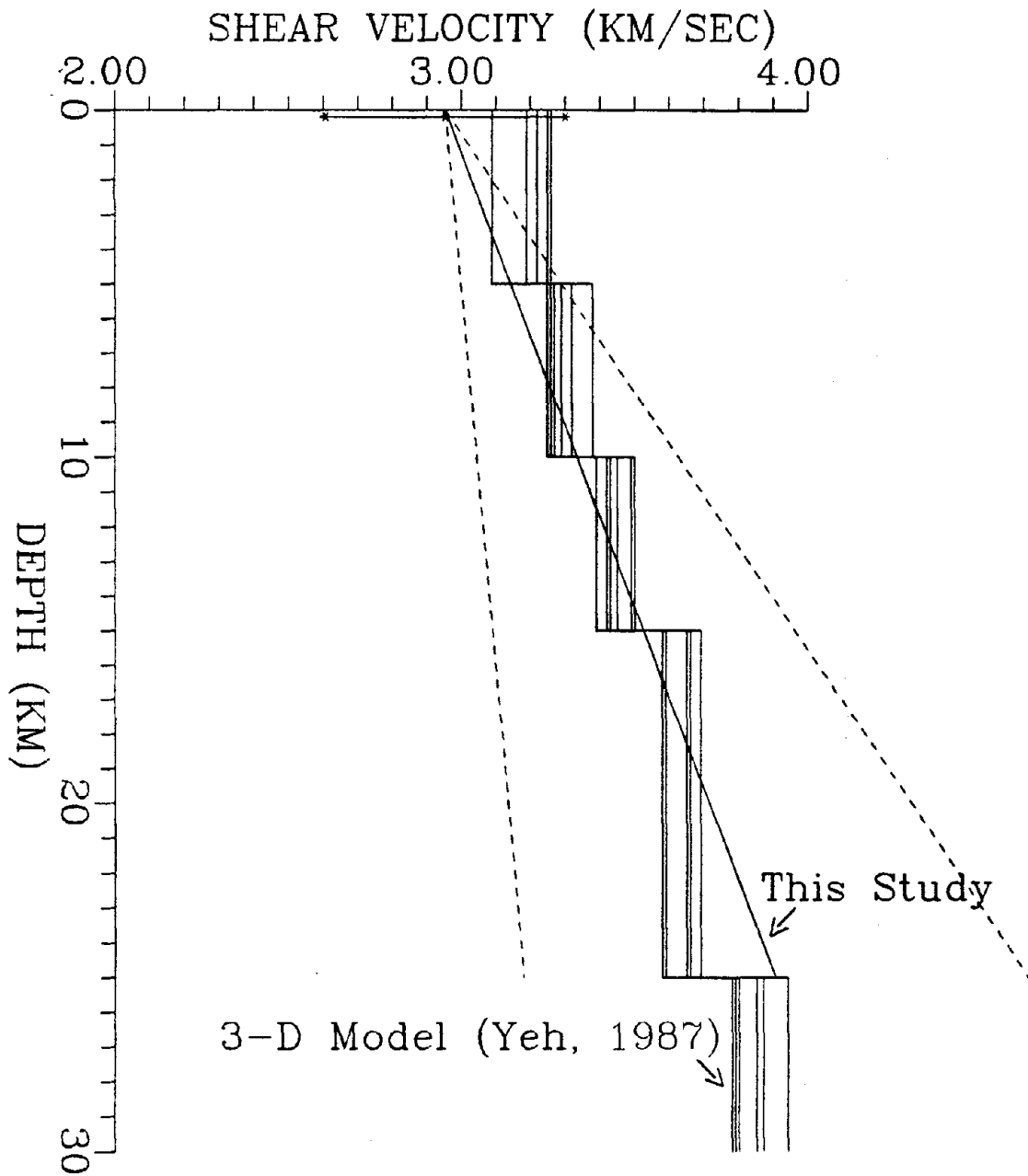


Figure 3.3 (b) Crustal S-velocity model. See Figure 3.3.a for explanation.

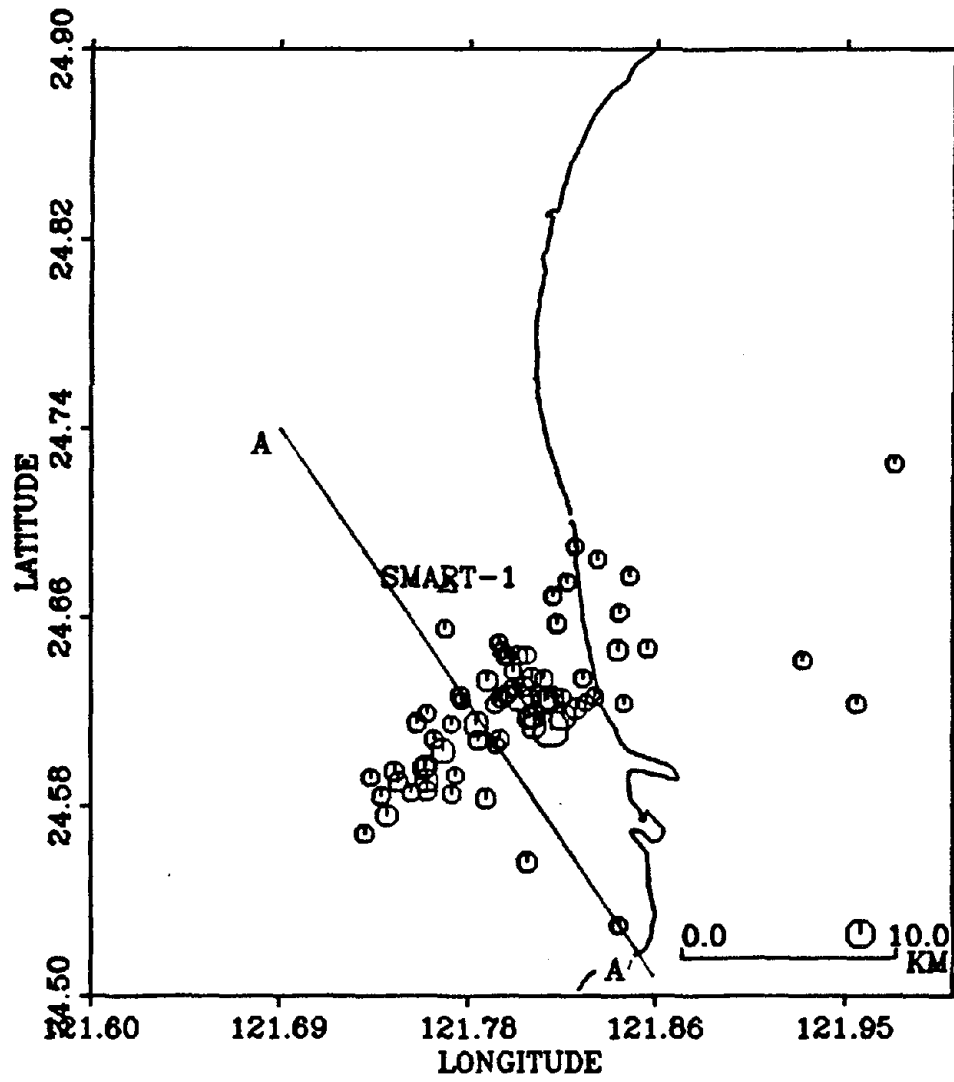


Figure 3.4 Epicenters of the July, 1986 sequence, Taiwan.

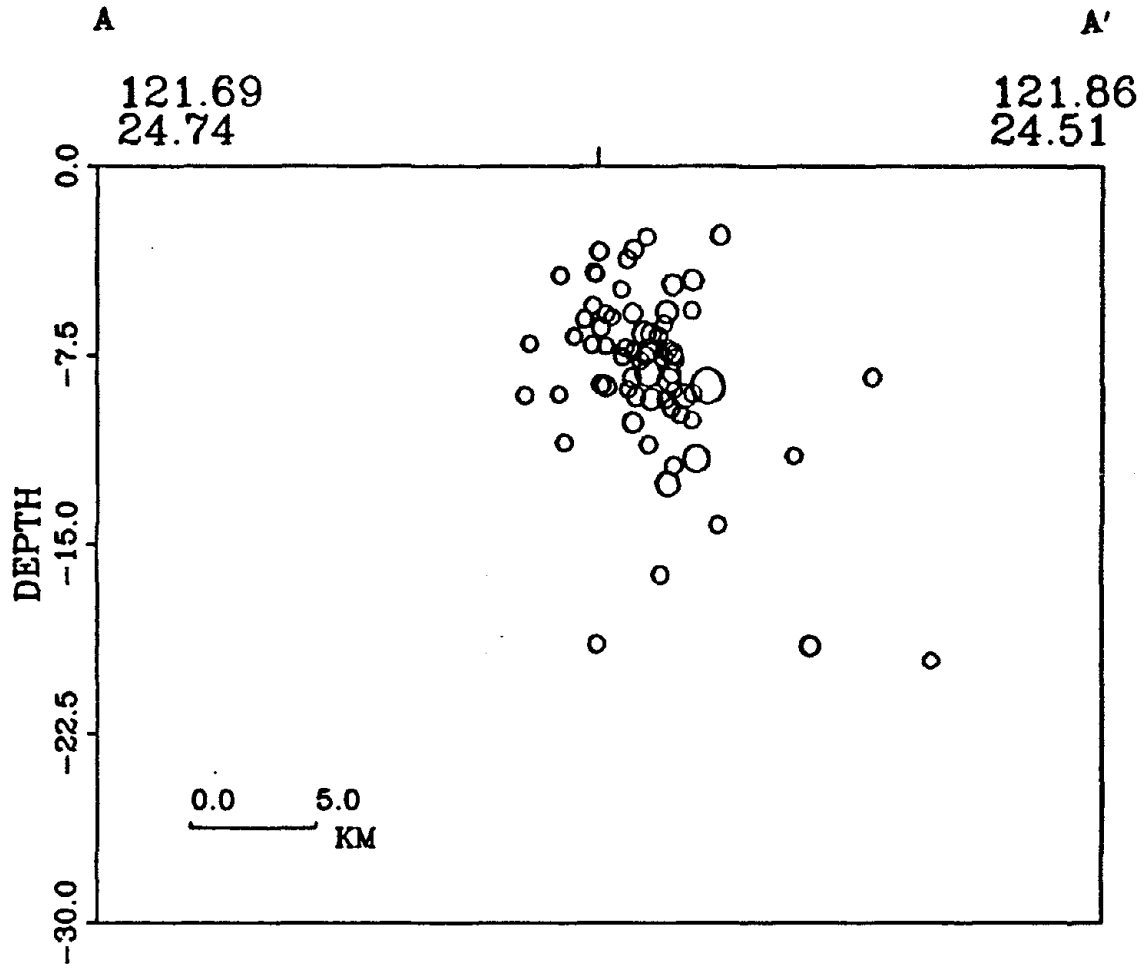


Figure 3.5 Hypocenters of the July, 1986 sequence, Taiwan on the vertical profile AA' shown in Figure 3.4.

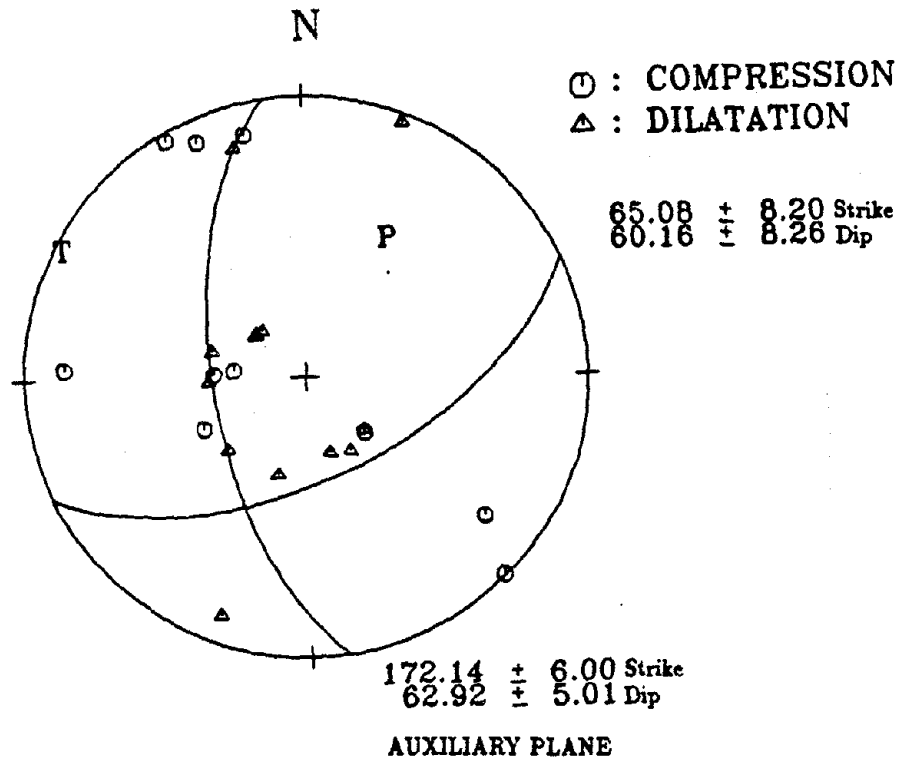


Figure 3.6 Fault plane solution of the July 30, 1986, Taiwan earthquake.

CHAPTER 4

AVAILABLE STRONG MOTION ARRAY DATA

§ 4.1 Description of the SMART1 Array

The SMART1 (Strong Motion Array Taiwan, No. 1) array is located in the northeast corner of Taiwan (Figure 4.1). Installation of this array began in September 1980 and was completed in August 1982. The research project based on SMART1 observations is conducted jointly by the Earth Sciences Institute, Academia Sinica, Taipei, Taiwan and the Seismographic Stations, University of California at Berkeley. The near-source array measurements of seismic waves have been used for both seismological and engineering studies. A detailed review of research results, up to 1987, that have utilized SMART1 array data, can be found in Abrahamson *et al.* (1987).

The SMART1 array consists of 39 stations (Figure 4.1). Each station has three components of broad-band, digital-recording accelerometers. These stations are arranged in three concentric rings of radii 200m, 1000m, and 2000 m, referred to as inner (I), middle (M), and outer (O) rings, respectively. Each ring has 12 stations numbered 1 through 12. There is one station (C-00) located at the center of the circular rings and two additional stations, E-01 and E-02, located 2.8 and 4.8 km south of the station C-00, respectively (Figure 4.1). The sensor used in the SMART1 array is the SA-300 triaxial accelerometer made by Columbia for Sprengnether Instruments Inc. The recorder is a DR-100 digital event recorder that has a 12 bit system. The sampling rate is 100 samples per second. The recording unit has a 5-pole Butterworth low-pass antialiasing filter at 25 Hz. More information on the instrumentation and operation of the SMART1 array is given in Bolt *et al.* (1982) and Abrahamson (1985).

Accurate absolute timing at each sensor of the array is crucial to the present study. Each array station has its own clock and the largest clock drift rate has been found to be

10 msec per day (Abrahamson, 1985). After every significant event, the clock errors were measured and were corrected later when raw data were processed at Berkeley. Abrahamson (1985) estimated that with this practice the timing accuracy should be better than 5 msec. This is a small timing error compared to the maximum time residuals of 0.06 sec estimated in Chapter 7.

The SMART1 array is located on the southern edge of a bowl-shaped sedimentary basin (Figure 4.2). Sediments beneath the array are 200 to 600 meters thick, thickening toward the northern part of the array (Wen and Yeh, 1984) (Figure 4.1). The soft sediments beneath the array consist of 3 to 18 meters of soil and 30 to 60 meters of alluvium. Below the soft sediments is a Pleistocene sedimentary formation with thickness of 170 to 540 meters. The bedrock is mainly composed of Miocene slate, phyllite, and argillite. The P- and S- wave velocity structure underneath the array is summarized in § 6.2 (Figure 6.3).

§ 4.2 Recorded Acceleration Data of Event 43

Fifty-five events have been recorded by the SMART1 array during the past 10 years (Table 4.1). Event 43 is one of the largest and also the closest event recorded. All 39 stations were triggered by this earthquake. Recorded maximum peak ground accelerations were 232, 244, and 300 cm/sec^2 on the vertical, east-west, and north-south components, respectively. None of the SMART1 outer ring stations were used in this study because the wave coherence at the outer ring was too low to render an accurate slowness estimate. The acceleration time histories recorded at the inner and middle rings are shown in Figure 4.3. The plotted time histories were normalized to the peak ground acceleration of each record. Peak ground acceleration, in units of cm/sec^2 , at each station is given at the left hand side of the station name in Figure 4.3.

Despite the close similarity of the waveform at each station, the peak ground acceleration displays a large range of values on the north-south component, from 110.2 to 230.9 cm/sec^2 (Figure 4.3.a). This large variation in peak acceleration for stations a few hundred meters

apart suggests that site conditions played an important role in modifying the ground motions. On the east-west component (Figure 4.3.b), waveform coherence across the inner and middle rings decreases after the 52 sec time mark. The first arrived S-phase is around the 51 sec time mark on both horizontal components. (For a discussion of the wave coherence at SMART1 see Abrahamson and Bolt, 1987).

The vertical component records (Figure 4.3.c) have more complicated acceleration time histories than the horizontal components. A wave packet before the first arriving S-phase is observed on the vertical component. This arrival may be due to the SV to P conversion at the basin-bedrock interface. The S-phases are responsible for the peak ground accelerations on the vertical component at most stations. The incoherence of the S and SV-P arrivals on the vertical component is probably caused by the strong interference with secondary waves generated locally within the basin. The dominance of high frequency resonance at station M-01 and M-02 is a typical example of wave phenomena generated by site effects overshadowing the direct waves originating from the seismic source. The difference in resonant frequencies and wave amplitudes between M-01 and M-02 implies a large variation in soil thickness as well as in soil properties under each station.

§ 4.3 Selection of an Optimal Subarray

In the plane-wave model defined by (2.5) and (2.6), the wavefield recorded by an array is represented by the superposition of propagating plane waves whose slowness vector $S(\xi)$ depends only on the source position ξ and the subsurface velocity structure. In practice, because of lateral inhomogeneities and the proximity to the seismic source, this plane-wave model is not a completely satisfactory approximation to the recorded wavefield. For an array close to the seismic source, the curvature of the spherical wavefront plays an important role in the recorded wavefield. In this study, the SMART1 array is located at a distance greater than several wavelengths from the seismic sources of interest; therefore, the wavefront curvature at the array is not as important as the lateral heterogeneity in contributing to the weakness of the plane-wave model (Aki and Richards, 1980).

Previous studies (Aki, 1973; Capon, 1974) of teleseismic P-waves within a large-aperture array, such as the now-closed LASA array in Montana which extends over a 100 km diameter, showed large spatial fluctuation of arrival time (or phase delay), wave slowness, and wave amplitude within the array. These fluctuations were attributed to lateral inhomogeneities in the crust and upper mantle beneath the array. Similar fluctuations have also been observed within the smaller SMART1 array. These fluctuations cause deviations from the plane wave model for the recorded wavefield at the SMART1 array, bias the slowness vector estimate, and consequently lead to biased estimation of source processes. It will be shown in § 5.3 that the array processing method used in this study gives unbiased slowness estimates if the travel-time deviations from the plane-wave model are small. Therefore, for the present work, it is crucial to select a subarray in which the wavefield approximately satisfies the following two conditions: (1) the wave slowness vector is spatially invariant within the subarray; (2) the wave arrival times within the subarray define plane wavefronts. In the following discussion, an explanation is given of how arrival times of a coherent S-phase were estimated, and how a subarray, in which the arrival times are compatible with the plane-wave model, was selected for further analysis in Chapter 7.

First, a time window which contains the most prominent S-phase on the NS acceleration was selected, as indicated by an arrow in Figure 4.3.a. Travel-time delays of this S-phase between all the station pairs were estimated by cross-correlation, after the acceleration data in the selected time window were band-pass filtered between 0.2 and 5.0 Hz by a 5-pole Butterworth filter. In general, the estimated maximum cross-correlation is above 0.7 for station pairs separated by a distance less than 1 km. The maximum cross-correlation of 0.44 between stations M-07 and M-01 is the smallest value among all the station pairs. A least-squares inversion was applied to these time delays to find the expected relative arrival time at each station (VanDecar and Crosson, 1990).

The S-wave arrival time contours (Figure 4.4) give mixed support to the plane-wave model for the wavefield recorded by the inner and middle rings. Fortunately, estimated

arrival times in the southeast quadrant display a wavefront that is approximately planar. Two distinct features are observed as the wavefront approaches the northwest quadrant. One is the increase of the apparent wave velocity. The other is the counterclockwise rotation of the wave propagation direction. I have observed the same pattern in other earthquakes with sources located at an azimuth similar to event 43. The spatial variation of wave propagation direction and wave slowness are violations of the plane-wave model of (2.6), where the wave slowness vector is not a function of receiver location. As a consequence, it is not experimentally sound to use the entire inner and middle rings for source studies. Because, however, stations in the southwest quadrant approximately satisfy the plane-wave model, the analysis of source processes in Chapter 7 will be restricted to a subarray consisting of stations in this quadrant only.

Because ray paths from the source to the inner- and middle- ring stations stay close together when leaving the fault plane, a large shallow inhomogeneity near the array is likely to be the cause of the wavefront distortion displayed in Figure 4.4. Two previous studies also suggest the existence of such a structure. Darragh (1987) found significant off-azimuth energy in the frequency-wavenumber spectrum of Event 39 (Table 4.1) that occurred 30 km northeast of the SMART1 array. He concluded that the scatterer is located 1 to 1.5 km southeast of C-00 and is estimated to be at a depth between 1.5 and 2.0 km. Furthermore, geomagnetic surveys in this area have revealed an anomalous strip south of the array (Yu and Tsai, 1979; Hsu, 1987). Hsu concluded that this anomaly may be explained by a shallow, thin, slab-like structure dipping 60 degrees to the north. His location of the slab is coincident with the scatterer inferred by Darragh. The northwest quadrant, in which the S-wave changes velocity and propagation direction (see Figure 4.4), would be at the 'illuminated' region of this slab for an earthquake occurring to the southeast of the array (see §6.3). Not enough variation was found, nor expected, in P-wave travel time to give conclusive independent support of the above argument.

To illustrate the possible changes in the slowness estimates that could arise from the

inclusion of stations in the northwest quadrant, slowness vectors that best match the arrival times of two subsets of the SMART1 stations were computed by the least-squares method (see §5.1.1). The first set included all the inner- and middle- ring stations and the second set included stations in the southeast quadrant only. The least-squares procedure gave a slowness vector estimate of (0.0867, -0.0655) for set 1 and, (0.1404, -0.1460) for set 2, in units of sec/km. The former slowness estimate is comparable to the P-wave slowness vector estimated in Chapter 7 and is obviously too high for an S-phase. This slowness estimate would give a source position deeper than 50 km which is contrary to the best hypocentral depth estimate of 12.7 km (see Chapter 3).

§ 4.4 Selection of a Time Window and Alignment of Records

In the present study, due to the limited resolving ability of array analysis methods to distinguish multiple seismic signals that are closely spaced on the slowness plane (Woods and Lintz, 1973) and the transient nature of seismic waves, the recorded time histories were divided into several time segments. Each segment contained one coherent arrival that can be visually identified at each station. With this approach, the number of dominant signals detected in one time segment is limited to one.

Because of the necessity of assigning an arrival time to each detected signal, a shorter time window centered around the seismic phase of interest would be preferable. The trade-off in using a short window is that the time needed by the signal to propagate across the array may be appreciably longer than the window length. Under this condition, the signal in question does not fall completely within the time span of the fixed window at every station. Truncation of the signal may result in false estimation of the slowness vector (Goldstein, 1988). For the SMART1 array, it takes the S-wave typically 0.5 sec to travel across the middle ring. In order to use a time window 0.64 sec or shorter it becomes necessary to shift the seismograms in time so they are aligned to a reference slowness vector. The reference slowness vector was selected so that each time window included the entire seismic arrival of interest without truncation.

The amount of time shift required for each seismogram was determined by the arrival-time difference between that station and the station C-00 predicted by the reference slowness vector. In the present work, the amount of time shift was rounded to the nearest time-sampling interval of 0.01 sec.

All three components at the selected stations were analyzed. The first few seconds of the vertical component were used to infer the P-wave source. The horizontal ground motion was not rotated into transverse and radial components. The S-wave portions of the two horizontal components were selected independently to study the source process responsible for the S energy.

The recorded waveforms at the selected subarray are similar, but the absolute amplitudes are quite different (Figure 4.3). The amplitude difference may be caused by the attenuation effect of soft sediments, the difference in site conditions of each station, and the difference in source radiation coefficients. Thus, before array processing, each acceleration time window was normalized to the peak ground acceleration in that window to reduce the site and attenuation effects.

Table 4.1

EVENTS RECORDED BY SMART-I ARRAY								
Event	M_L	Depth (Km)	Δ (Km)	Azimuth (Deg)	T/I [†]	Maximum Acceleration(gal)		
						V	EW	NS
1	6.1	27	36	192	16/21	15.7	22.3	25.4
2	5.9	78	7	168	16/21	31.7	74.4	83.8
3	5.7	10	28	179	13/21	10.7	22.9	24.6
4	5.6	61	83	185	2/27	2.4	8.1	9.0
5	6.3	25	30	149	29/29	97.4	168.5	259.8
6	5.5	76	9	86	10/27	4.4	13.6	12.2
7	6.2	25	201	189	3/27	2.7	6.4	10.5
8	4.8	10	32	57	19/27	16.0	23.5	34.5
9	4.2	5	5	51	12/28	13.1	22.8	19.1
10	5.1	75	48	88	10/28	16.6	21.0	18.3
11	5.6	10	29	152	8/28	10.1	13.2	15.0
12	4.9	12	35	54	18/36	24.4	24.8	37.8
13	4.4	10	36	67	14/36	14.1	33.8	45.9
14	5.0	20	26	139	31/36	17.7	31.6	43.5
15	3.6	4	3	239	29/37	40.5	71.7	55.7
16	6.2	13	84	182	11/36	9.2	23.7	20.2
17	4.7	11	19	47	8/35	22.3	28.2	26.0
18	5.1	15	22	46	24/36	31.1	75.5	97.1
19	4.9	17	36	107	28/35	21.7	43.0	32.8
20	6.4	88	79	99	33/33	33.8	67.0	68.1
21	6.6	115	88	90	11/36	9.9	49.5	25.2
22	6.4	19	31	212	35/37	39.0	75.2	68.4
23	6.6	43	87	125	23/37	13.2	29.0	42.0
24	6.9	48	84	124	31/39	16.4	53.9	69.4
25	6.8	44	68	134	35/39	18.3	37.5	39.3
26	5.5	69	17	95	10/39	8.6	30.1	45.6
27	6.3	57	100	122	11/39	11.8	17.0	20.0
28	5.9	16	83	72	28/39	19.4	65.2	55.6
29	6.0	28	46	57	30/39	30.1	76.9	68.7
30	6.3	88	28	67	32/39	37.4	70.2	84.1
31	5.9	4	48	79	37/39	39.2	108.6	73.7
32	6.0	5	48	101	21/38	17.2	49.7	39.5
33	6.5	3	45	104	35/38	49.2	157.6	103.9
34	5.8	1	34	160	25/38	21.8	36.2	40.4
35	5.7	8	5	26	37/38	74.8	94.3	141.1
36	6.3	6	47	110	36/38	58.6	121.0	87.8
37	5.3	2	30	167	33/38	43.8	56.6	77.2
38	5.5	74	13	26	14/38	15.1	24.6	32.4
39	6.5	10	22	64	36/39	333.6	258.4	327.5
40	6.5	16	67	195	37/38	77.2	224.2	266.4
41	6.2	22	71	192	37/38	30.2	66.2	80.8
42	5.0	12	5	107	38/39	82.0	140.8	151.1
43	6.2	10	6	150	39/39	232.2	244.5	300.6
44	4.9	9	5	141	37/38	39.8	109.1	103.0
45	7.0	7	79	175	36/39	110.3	178.0	251.0
46		45	75	159	26/39	8.8	25.6	35.2
47		22	84	175	34/39	25.0	54.3	61.2
48		30	86	175	32/39	14.5	31.1	34.2
49	4.5	117	26	357	22/39	21.8	39.1	34.0
50	6.6	41	76	179	34/39			
51	5.8	72	19	133	31/39	18.7	45.7	50.6
52	5.7	31	53	144	26/39	17.3	29.6	39.6
53	5.3	1	42	199	26/39	29.0	41.7	62.5
54	5.2	35	28	189	35/43	39.7	95.2	112.6
55	5.6	63	68	108	22/43	17.8	30.7	29.0

† T/I = Number of stations triggered / Number of stations installed

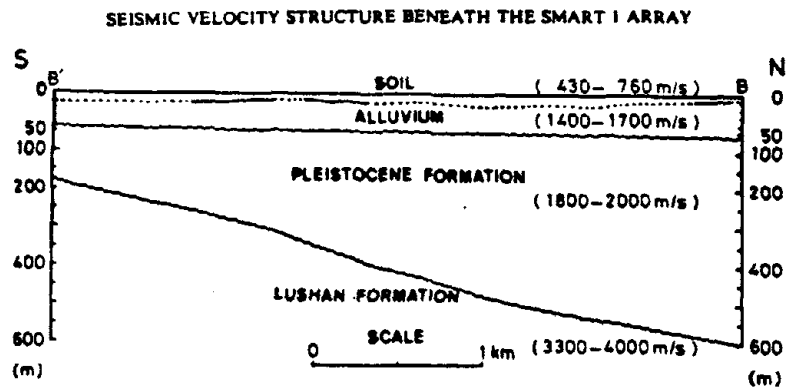
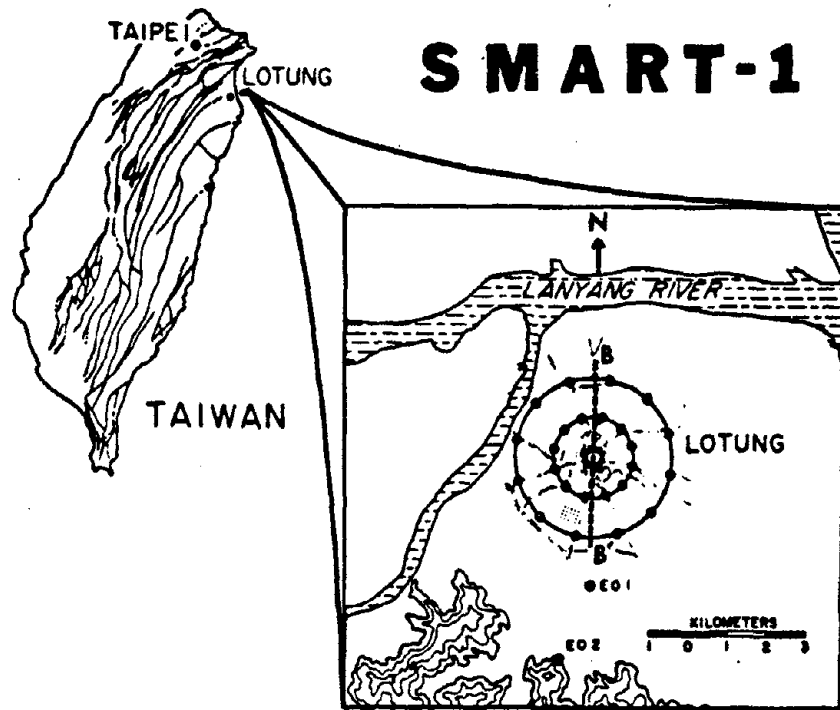


Figure 4.1 (Top left): Location of SMART1 array in northeast Taiwan. (Top right): SMART1 array. The stations are shown as solid circles. (Bottom): Subsurface structure along the profile BB' (from Wen and Yeh, 1984).

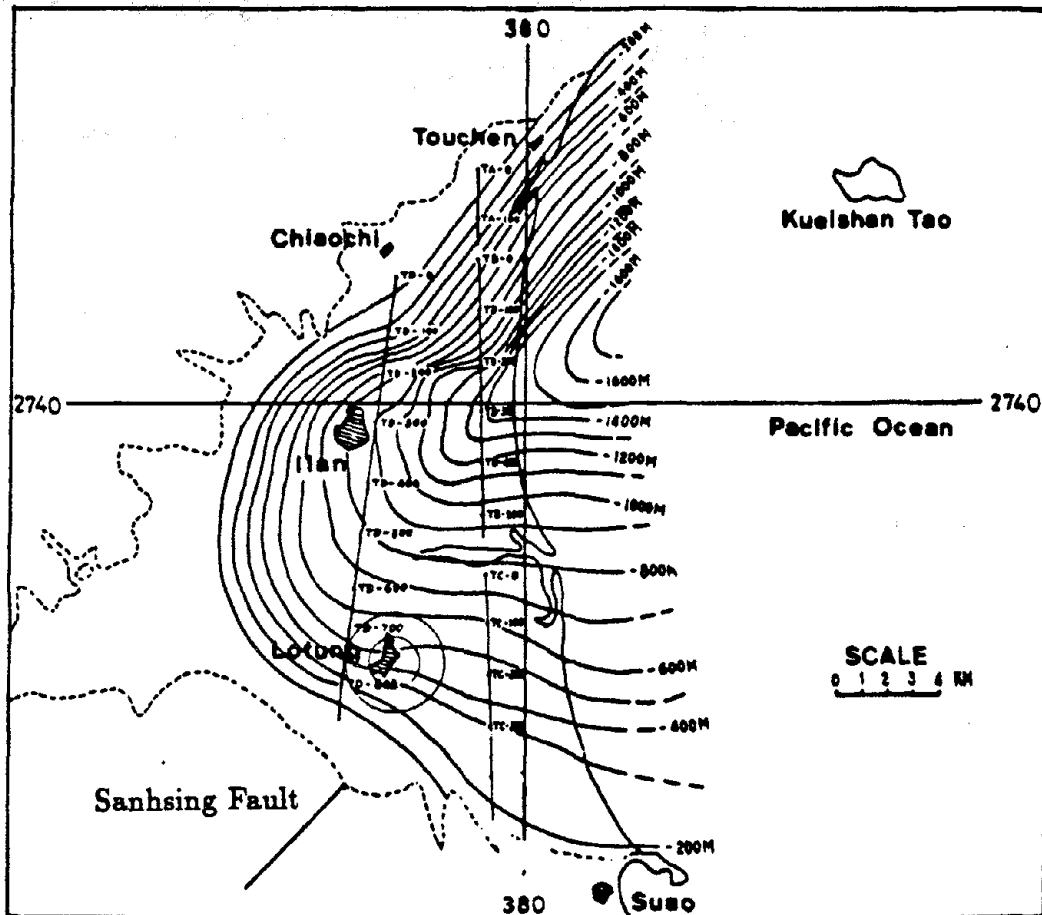


Figure 4.2 Contour map of the basin thickness (Taken from Chiang, 1976). The circles indicate the location of the SMART1 array. Sanhsing fault is south of the basin.

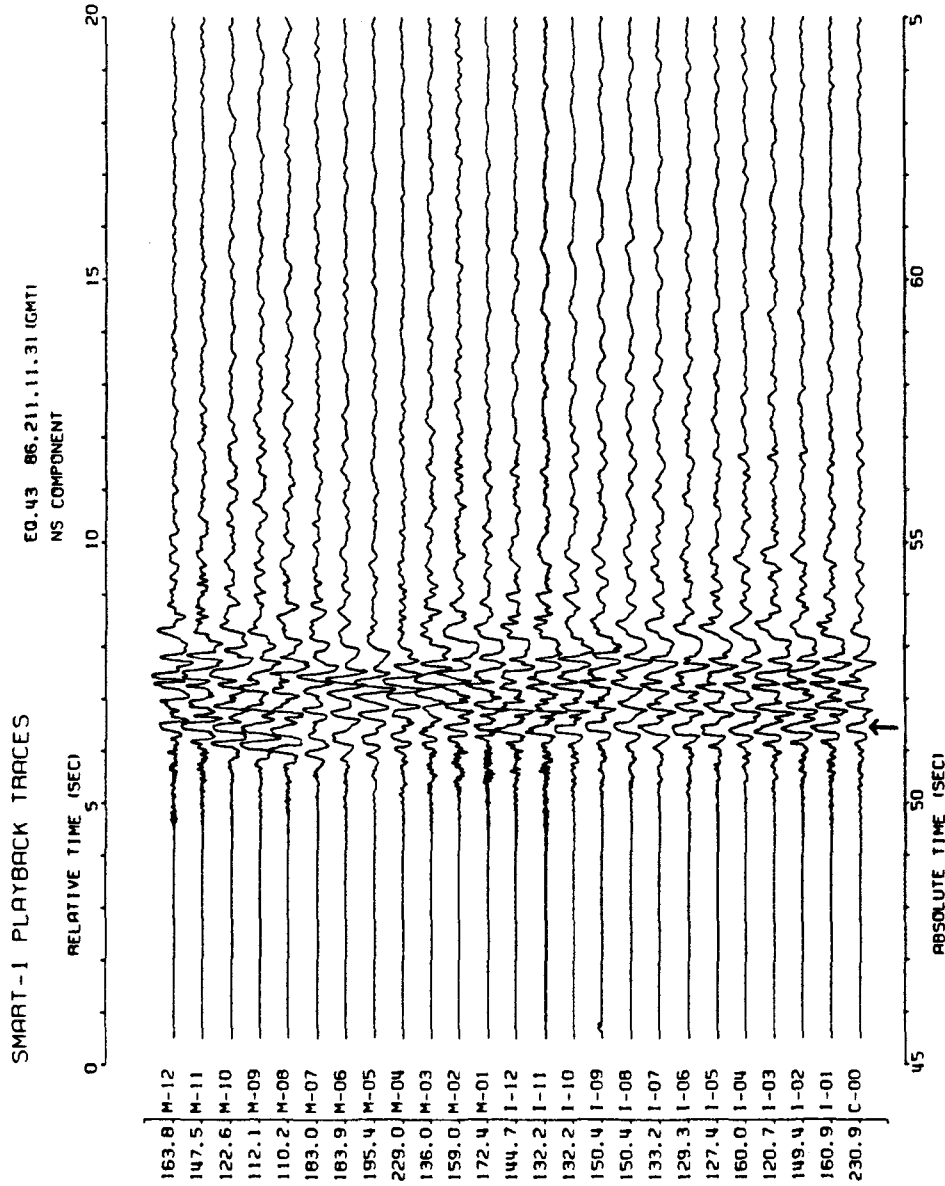


Figure 4.3 (a) North-South component accelerograms recorded at the inner and middle rings during the July 30, 1986 Taiwan earthquake. The records are normalized to peak ground acceleration. The arrow indicates the S phase that was used for arrival-time estimation.

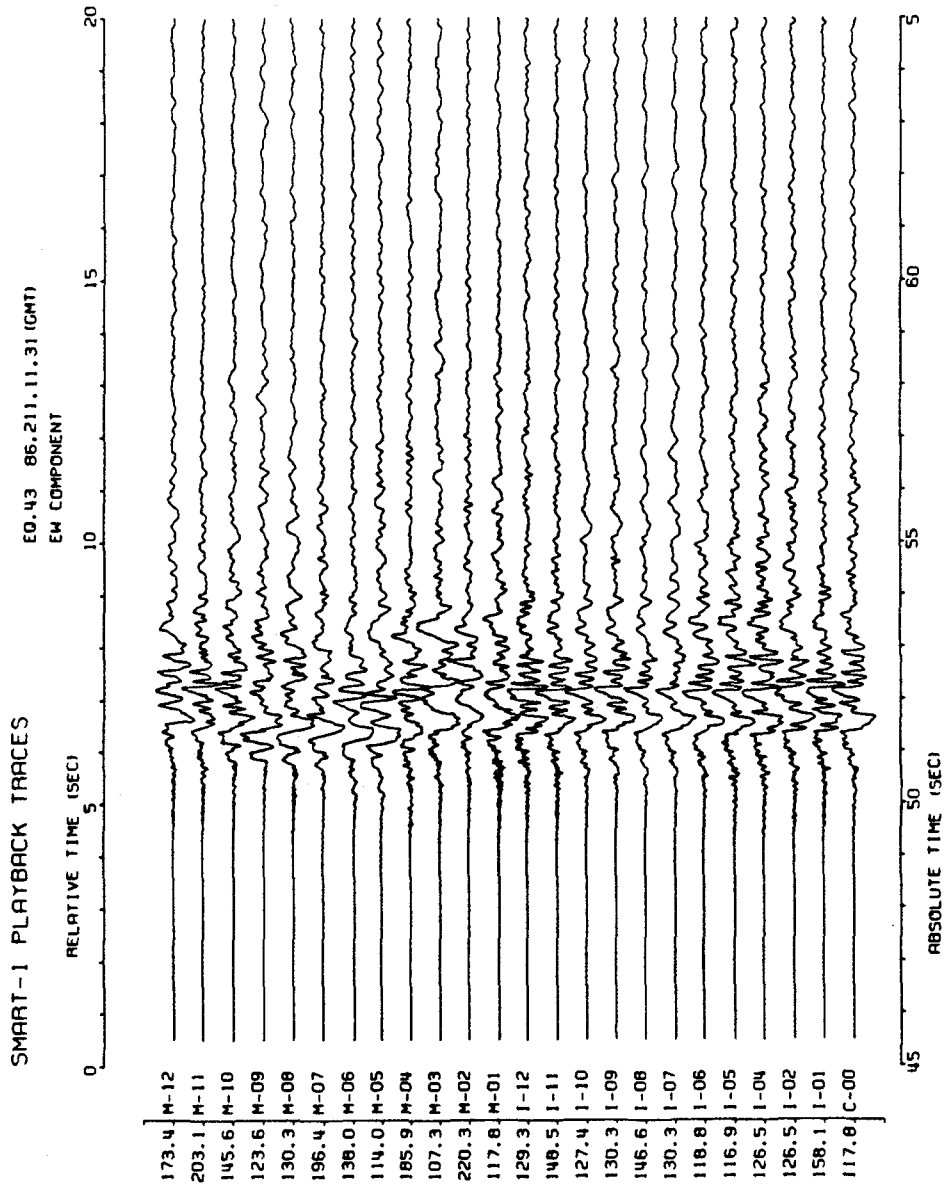


Figure 4.3 (b) East-West component accelerograms.

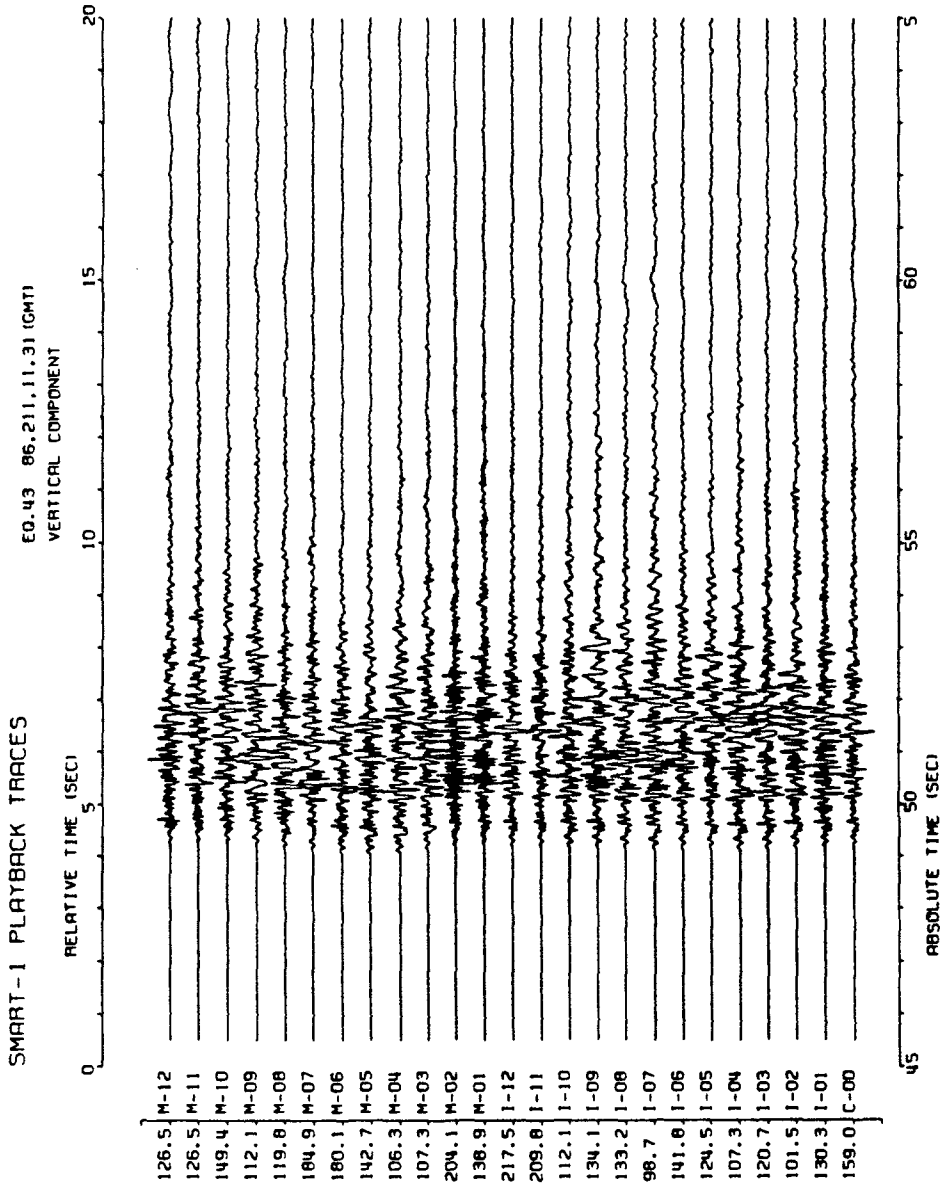


Figure 4.3 (c) Vertical component accelerograms.

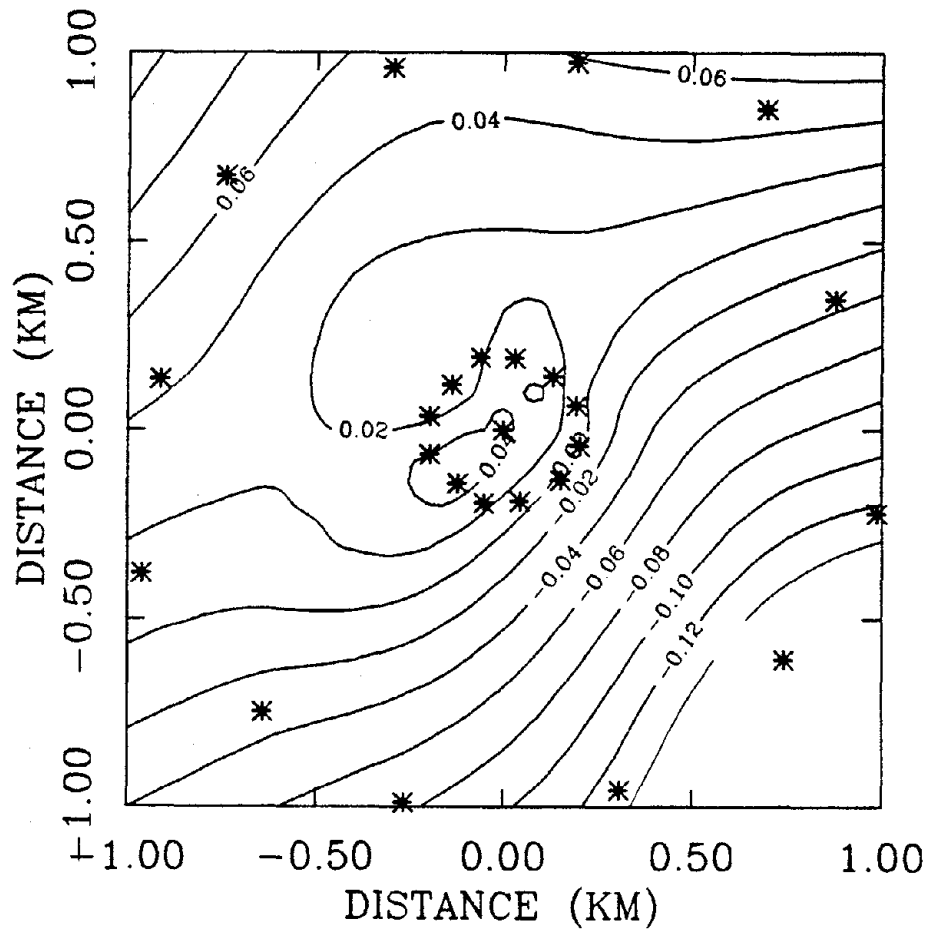


Figure 4.4 Arrival-time contour of the S-wave indicated by the arrow in Figure 4.3.a. Contour interval is 0.02 sec. The star symbols indicate the inner and middle ring stations.

CHAPTER 5

SLOWNESS ESTIMATION FROM BROAD-BAND DATA

Slowness estimation for a non-dispersive broad-band signal can be accomplished through either a time-domain or a frequency-domain method. The time-domain approach uses travel-time delays to estimate the slowness vector, while the frequency-domain approach uses phase delays for slowness estimation. In the first case, the travel-time delay is estimated by generalized cross-correlation methods (Carter, 1981), which incorporate information contained in a broad frequency band of the data. Then, an optimization algorithm, such as the least-squares method (e.g. Bates and Kanasevich, 1985), can be used to invert time delays for the slowness vector. The advantages of this approach are that it is truly a broad-band method, it is conceptually simple, and the uncertainty of the slowness estimates may be assessed. On the other hand, the drawbacks of the time-domain approach are, first, its inability to handle multiple signals and, secondly, the accuracy of the time-delay estimate is limited to one half the time sampling interval if time interpolation is not made. Spudich and Cranswick (1984) used this approach in their study of the 1979, Imperial Valley earthquake.

In the second approach, the phase delay is naturally included in the cross-power spectra matrix and in the spatial cross-covariance matrix of the Fourier coefficients. Therefore, formulations of frequency-domain methods, such as conventional beamforming (CV), the high resolution method (HR) (Capon, 1969), and the narrow-band MUSIC (Multiple Signal Characterization) method (Schmidt, 1981), are based on either one of these two matrices. Another aspect of frequency-domain methods is their capability of resolving multiple signals. Averaging over neighboring time windows is not applicable to most seismograms, because of their non-stationary and transient character. Because only one temporal sample is available to estimate the cross-covariance matrix the variance of the cross-covariance

matrix estimate is commonly large and its matrix rank is deficient. Although the estimated variance and the rank of the cross-covariance matrix estimate can be improved by spatial- and frequency- smoothing, the applicability of smoothing techniques is severely limited in most practical situations. This is because frequency smoothing results in the unwanted mixing of deterministic phase delays for components of different frequencies (Abrahamson and Bolt, 1987). Also, spatial smoothing can be applied effectively only to arrays with special symmetry; most existing seismic arrays do not provide, for example, the required linear subarrays whose sensors are equispaced (Goldstein and Archuleta, 1987). The effective number of array sensors will also be reduced as a result of spatial smoothing. In this study, the SMART1 subarray configuration selected is non-symmetrical, as explained in Chapter 4. One study that utilized spatial smoothing (Goldstein and Archuleta, 1991b) used the entire circular SMART1 array that extends over a 4 km diameter. However, the low coherence at the outer ring and the failure of the plane-wave approximation leads to a large bias in slowness vector estimates, as discussed in Chapter 4.

In summary, the major obstacle in the preferred use of the frequency-domain approach, especially in seismological applications, is its inability to effectively combine information in the broad frequency components to improve estimation performance. Methods such as CV, HR, and MUSIC are narrow-band methods in the sense that phase information from only a few frequency components are used in the process of slowness estimation. In this regard, after-processing schemes, such as slowness stacking (Bostwick *et al*, 1985; Spudich, 1986; Darragh, 1987) which combine results from narrow-band processing, have been used as a substitute for true broad-band processing.

In the following description, a new frequency-domain algorithm called the Coherent Signal Subspace (CSS) method (Wang and Kaveh, 1985) will be used (perhaps for the first time in seismogram array analysis). In § 5.1 and § 5.2, it will be demonstrated that, for broad-band data, CSS is a way to avoid the problems of rank deficiency, large variance, and deterministic phase mixing inherent in frequency smoothing. A comparison of CSS to

CV, HR, and MUSIC will be made. In the case of one dominant signal, CSS will be shown to be equivalent to the least-squares estimation method. In § 5.3, the bias and covariance of the slowness estimate, caused by the deterministic time error and the random phase fluctuation, are given. A new approach to estimate the slowness vector and array response simultaneously is proposed.

§ 5.1 Coherent Signal Subspace Method

In this section, the basic formulation and assumptions of a broad-band array processing algorithm called the Coherent Signal Subspace (CSS) method (Wang and Kaveh, 1985) are given. CSS, like Schmidt's MUSIC, is based on eigen-decomposition and utilizes the geometrical properties of the eigen-structure of the spatial cross-covariance matrix. Therefore, CSS may also be classified under the general topic of 'principle component analysis' of time series (Chapter 9 of Brillinger, 1981). In the case of multiple signals, one of the main differences between CSS and the principle component analysis approach of Der and Flinn (1975), is that the latter uses the eigenvectors directly as estimates of the directional vectors of multiple signals. This results in stringent conditions for the resolvability of multi-signals.

In the CSS method, broad-band data recorded by an array of sensors are represented as the superposition of incident signals convolved with the array response, plus background noise. Equation (2.6) justifies the use of this model-based algorithm for seismic source studies. The association of CSS with (2.6) gives the appropriate seismological interpretation of the eigenstructure of the spatial cross-covariance matrix.

In matrix notation, the Fourier coefficient (2.6) at frequency ω_k is

$$\mathbf{u} = \mathbf{A}\mathbf{d} + \mathbf{n}, \tag{5.1}$$

where

$$\mathbf{u} = \begin{pmatrix} u(\omega_k, \mathbf{x}_1) \\ u(\omega_k, \mathbf{x}_2) \\ \vdots \\ u(\omega_k, \mathbf{x}_M) \end{pmatrix}, \quad \mathbf{d}(\omega_k) = \begin{pmatrix} \Phi(\xi_1) \dot{D}(\omega_k, \xi_1) e^{-i\omega_k(\tau(\xi_1)+T(\xi_1, \mathbf{x}_0))} \\ \Phi(\xi_2) \dot{D}(\omega_k, \xi_2) e^{-i\omega_k(\tau(\xi_2)+T(\xi_2, \mathbf{x}_0))} \\ \vdots \\ \Phi(\xi_N) \dot{D}(\omega_k, \xi_N) e^{-i\omega_k(\tau(\xi_N)+T(\xi_N, \mathbf{x}_0))} \end{pmatrix},$$

$$\mathbf{A} = \begin{pmatrix} A_{11} & A_{12} & \dots & A_{1N} \\ A_{21} & A_{22} & \dots & A_{2N} \\ \vdots & \vdots & \ddots & \vdots \\ A_{M1} & A_{M2} & \dots & A_{MN} \end{pmatrix},$$

with

$$A_{ij} = \frac{1}{\sqrt{M}} e^{-i\omega_k[\mathbf{S}(\xi_j) \cdot (\mathbf{x}_i - \mathbf{x}_0)]},$$

$i = 1, \dots, M; j = 1, \dots, N$, \mathbf{u} is the $(M \times 1)$ Fourier coefficients vector of the recorded wavefield, \mathbf{d} is the $(N \times 1)$ incident signal vector, and \mathbf{A} is the $(M \times N)$ array response matrix. \mathbf{A} represents the array response at frequency ω_k to an incident seismic signal originating from the seismic source located at ξ_j . The exponent in A_{ij} is the plane-wave phase delay at station \mathbf{x}_i , relative to the reference station \mathbf{x}_0 . Note that A_{ij} is a function of sensor location \mathbf{x}_i , seismic source location ξ_j , and frequency ω_k .

The unknown parameters in (5.1) are the number of signals, N , the signal slowness vectors, $\{\mathbf{S}(\xi_i), i = 1, \dots, N\}$, and the incident signal \mathbf{d} . The strength of the incident signal is determined by the amount of energy radiated from the seismic source and the subsequent modification by the propagation effects, such as the crustal attenuation. It is assumed in the model (5.1) that the incident signal \mathbf{d} is observed by all the sensors with the same amplitude. Therefore, the array response \mathbf{A} includes only the phase delay and the array gain is uniformly one. In reality, different site conditions cause the array gain to be non-uniform. To better satisfy the unit-gain assumption, data recorded at all the sensors are normalized to their individual peak values, as described in § 4.4, to reduce the site effects. It should be noted that an approach has been proposed whereby array processing can be performed with unknown array gain (Weiss *et al.*, 1988).

Two other assumptions are made in the CSS method: firstly, the noise at each station is uncorrelated with all other stations and secondly, the incident signal and noise have zero-mean and are uncorrelated. The spatial cross-covariance of the Fourier coefficients (5.1) at frequency ω_k is

$$\mathbf{R}_u(\omega_k) = \mathbf{A}(\omega_k)\mathbf{R}_d(\omega_k)\mathbf{A}^H(\omega_k) + \sigma(\omega_k)\mathbf{I}, \quad (5.2)$$

where $\mathbf{R}_d(\omega_k)$ is the cross-covariance matrix of the source signals. The noise at each station is assumed to be uncorrelated, hence the cross-covariance matrix of noise is $\sigma(\omega_k)\mathbf{I}$, where \mathbf{I} is a $(M \times M)$ identity matrix. \mathbf{A}^H is the Hermitian of \mathbf{A} .

Because elements of the array response matrix \mathbf{A} are functions of frequency, direct combination of (5.2) at different frequencies, such as frequency smoothing, destroys the phase-delay information that is essential to slowness estimation. This problem is avoided by using a unitary transformation $\mathbf{T}(\omega_k, \omega_o)$ (Wang and Kaveh, 1985; Hung and Kaveh, 1988) such that

$$\mathbf{T}(\omega_k, \omega_o)\mathbf{A}(\omega_k) = \mathbf{A}(\omega_o), \quad (5.3)$$

where ω_o is a reference frequency. The construction of $\mathbf{T}(\omega_k)$ is discussed in Hung and Kaveh (1988). Application of the transformation to (5.1) and (5.2) yields the steered Fourier coefficient vector

$$\mathbf{u}^*(\omega_k) = \mathbf{T}(\omega_k, \omega_o)\mathbf{u}(\omega_k) = \mathbf{A}(\omega_o)\mathbf{d}(\omega_k) + \mathbf{T}(\omega_k, \omega_o)\mathbf{n}(\omega_k) \quad (5.4)$$

and the steered cross-covariance matrix

$$\begin{aligned} \mathbf{R}_{u^*}(\omega_k) &= \mathbf{T}(\omega_k, \omega_o)\mathbf{R}_u(\omega_k)\mathbf{T}^H(\omega_k, \omega_o) \\ &= \mathbf{A}(\omega_o)\mathbf{R}_d(\omega_k)\mathbf{A}^H(\omega_o) + \sigma(\omega_k)\mathbf{I}. \end{aligned} \quad (5.5)$$

The matrix \mathbf{R}_{u^*} is the unitary equivalent to \mathbf{R}_u . The focusing transformation \mathbf{T} steers the array response at frequency ω_k to the reference frequency ω_o . This unitary transformation does not alter the eigenvalues of (5.2), but rotates the eigenvectors to those corresponding to the frequency component ω_o . The result is the condensation of the broad-band signal into

a narrow frequency band at ω_o . With (5.5), we can take the average of the steered cross-covariance matrix $\mathbf{R}_{u^*}(\omega_k)$ at K different frequencies and still preserve the array response matrix at the reference frequency ω_o . Taking the average for K frequencies,

$$\begin{aligned}\mathbf{P}_{u^*} &= \frac{1}{K} \sum_{k=1}^K \mathbf{R}_{u^*}(\omega_k) \\ &= \mathbf{A}(\omega_o) \mathbf{P}_d \mathbf{A}^H(\omega_o) + \sigma \mathbf{I},\end{aligned}\tag{5.6}$$

where

$$\begin{aligned}\mathbf{P}_d &= \frac{1}{K} \sum_{k=1}^K \mathbf{R}_d(\omega_k), \\ \sigma &= \frac{1}{K} \sum_{k=1}^K \sigma(\omega_k).\end{aligned}$$

In comparison with the MUSIC method, the major difference, and also the advantage of CSS, is that the focusing transformation allows the use of information in a broad frequency band for eigenstructure estimation. This not only avoids the problem of rank deficiency of the cross-covariance matrix, but also improves the accuracy of the eigenvector estimates.

\mathbf{P}_{u^*} is a positive-definite, full-rank matrix and thus has M non-negative real eigenvalues $\lambda_1 \geq \lambda_2 \geq \dots \geq \lambda_M > 0$ with corresponding eigenvectors $\mathbf{e}_1, \mathbf{e}_2, \dots, \mathbf{e}_M$. It can be shown (see Wang and Kaveh, 1985) that, for \mathbf{P}_d having rank N , the minimum eigenvalue of \mathbf{P}_{u^*} is σ and has a multiplicity of $M - N$, i.e. $\lambda_{N+1} = \dots = \lambda_M = \sigma$. In practice, this property is used to determine the number of signals N . Furthermore, there is an orthogonality condition,

$$\mathbf{A}^H \mathbf{e}_i = \mathbf{0}, \quad i = 1, \dots, N.\tag{5.7}$$

Column vectors of \mathbf{A} lie in the *signal-subspace* spanned by the signal-eigenvectors $\{\mathbf{e}_i, i = 1, \dots, N\}$; in other words, column vectors of \mathbf{A} are orthogonal to the noise-eigenvectors $\{\mathbf{e}_i, i = N + 1, \dots, M\}$. This property is utilized to estimate the slowness vector in both CSS and MUSIC algorithms.

For $N = 1$, the signal-eigenvector is identical to the array response vector. For $N > 1$, the column vectors of \mathbf{A} are linear combinations of the signal-eigenvectors and are non-parallel to the signal-eigenvectors in most cases. Hence the resolving power of an algorithm that utilizes signal-eigenvectors as direct estimates of the array response matrix (e.g. Der and Flinn, 1975) is severely limited by the signal-eigenvectors being oblique to the column vectors of \mathbf{A} .

Without the focusing transformation, the signal-subspace at each frequency component is different. With the transformation, the signal-subspace of (5.6) and of the steered cross-covariance matrix (5.5) at any frequency component are identical, and hence the name 'Coherent' signal-subspace for this method. In practice, the steered cross-covariance matrix at one frequency component can be regarded as one data sample of the signal-subspace at frequency ω_o and averaging of the steered cross-covariance matrix over K frequencies, in effect, increases the sample size of the signal-subspace to K . This is one great advantage over the other methods, as averaging improves the accuracy of the eigenvector estimates and, hence, also the slowness estimates. The averaging also ensures the non-singularity of \mathbf{P}_d even if $\mathbf{R}_d(\omega_k)$ is singular. The latter property enables CSS at least in theory to handle correlated incident signals.

The practical procedure in both CSS and MUSIC for slowness estimation is to form the general array response vector

$$\mathbf{a} = \frac{1}{\sqrt{M}} \begin{pmatrix} e^{-i\omega_o[\mathbf{S} \cdot (\mathbf{x}_1 - \mathbf{x}_o)]} \\ e^{-i\omega_o[\mathbf{S} \cdot (\mathbf{x}_2 - \mathbf{x}_o)]} \\ \vdots \\ e^{-i\omega_o[\mathbf{S} \cdot (\mathbf{x}_M - \mathbf{x}_o)]} \end{pmatrix},$$

then project this vector onto the estimated noise-subspace, and take the reciprocal of that projection,

$$Q(\mathbf{S}) = \frac{1}{\sum_{i=N+1}^M |\mathbf{a}^H(\mathbf{S}) \cdot \hat{\mathbf{e}}_i|^2} = \frac{1}{D},$$

where

$$D = 1 - \sum_{i=1}^N |\mathbf{a}^H(\mathbf{S}) \cdot \hat{\mathbf{e}}_i|^2. \quad (5.8)$$

An estimate of $\mathbf{S}(\xi_i)$ may thus be obtained by searching over a grid of points on the slowness plane for \mathbf{S} where the projection onto the noise-subspace (i.e. D) is a local minimum (see equation (5.7)). Other search algorithms have been proposed (e.g. Kumaresan and Tufts, 1983). However, regardless of the search method, accuracy of the slowness estimation is dominated by the accuracy of the signal-subspace estimate.

In what follows, an estimate of an unknown parameter θ will be denoted by $\hat{\theta}$.

In theory, column vectors of the plane-wave array response matrix \mathbf{A} lie completely within the signal-subspace. In practice, because of signal mixing, truncation, intercorrelation, and noise non-stationarity, the signal-subspace estimated from the array data is not exactly identical to the true signal-subspace, therefore resulting in a non-zero projection (i.e. $D \neq 0$) of $\mathbf{a}(\hat{\mathbf{S}})$ onto the estimated noise-subspace. $D(\hat{\mathbf{S}})$ can thus be interpreted as the deviation of the wavefield from the plane-wave propagation model predicted by $\mathbf{a}(\hat{\mathbf{S}})$. The algorithm described above searches for the best fitting plane-wave slowness vectors to the recorded wavefield.

Alternatively, the array response matrix can be defined directly in terms of the source positions ξ_j and \mathbf{Q} computed over a grid of source points on the fault plane. Estimation of the source process can thus be achieved without inverting $\hat{\mathbf{S}}(\xi_j)$ for ξ_j . However, this approach does not allow us to assess the level of uncertainties associated with the velocity model and fault plane orientation (see §6.2).

§ 5.1.1 Equivalence to the Least-Squares Estimate of the Single Signal Case

For the case of one signal, from equation (5.8),

$$D = 1 - M^{-1} \left| \sum_{i=1}^M e^{i(\omega_o \mathbf{S} \cdot (\mathbf{x}_i - \mathbf{x}_o) - \hat{\phi}_i)} \right|^2.$$

$\hat{\phi}_i$ is the phase angle of the i -th element of $\hat{\mathbf{e}}_1$. When \mathbf{S} is near the true slowness vector $\mathbf{S}(\xi)$, the quantity $(\omega_o \mathbf{S} \cdot (\mathbf{x}_i - \mathbf{x}_o) - \hat{\phi}_i)$ is small. With this approximation, keeping only the

first-order term of the above quantity,

$$\begin{aligned}
D &\approx 1 - M^{-1} \left| \sum_{i=1}^M \sqrt{1 - (\omega_o \mathbf{S} \cdot (\mathbf{x}_i - \mathbf{x}_o) - \hat{\phi}_i)^2} + i(\omega_o \mathbf{S} \cdot (\mathbf{x}_i - \mathbf{x}_o) - \hat{\phi}_i) \right|^2 \\
&= 1 - M^{-1} \left| \sum_{i=1}^M \sqrt{1 - (\omega_o \mathbf{S} \cdot (\mathbf{x}_i - \mathbf{x}_o) - \hat{\phi}_i)^2} + i \sum_{i=1}^M (\omega_o \mathbf{S} \cdot (\mathbf{x}_i - \mathbf{x}_o) - \hat{\phi}_i) \right|^2 \\
&\approx 1 - M^{-1} \sum_{i=1}^M 1 - (\omega_o \mathbf{S} \cdot (\mathbf{x}_i - \mathbf{x}_o) - \hat{\phi}_i)^2 \\
&= M^{-1} \sum_{i=1}^M (\omega_o \mathbf{S} \cdot (\mathbf{x}_i - \mathbf{x}_o) - \hat{\phi}_i)^2.
\end{aligned}$$

D is thus, to the first-order, the mean-square phase prediction error, and therefore the search algorithm of CSS gives the same slowness vector estimate as the least-squares problem

$$\phi_i = \phi_o + \omega_o \mathbf{S} \cdot \mathbf{x}_i, i = 1 \dots N. \quad (5.9.a)$$

Or, dividing out ω_o ,

$$t_i = t_o + \mathbf{S} \cdot \mathbf{x}_i, i = 1 \dots N, \quad (5.9.b)$$

where t_i is the arrival time at station i .

The normal equations for the least-squares problem (5.9.a) are (Bates and Kanasewich, 1985),

$$\mathbf{X}_1 \mathbf{S} = \mathbf{X}_2 \mathbf{t},$$

where

$$\mathbf{X}_1 = \begin{pmatrix} \sum x_i^2 - M^{-1}(\sum x_i)^2 & \sum x_i y_i - M^{-1} \sum x_i \sum y_i \\ \sum x_i y_i - M^{-1} \sum x_i \sum y_i & \sum y_i^2 - M^{-1}(\sum y_i)^2 \end{pmatrix},$$

$$\mathbf{X}_2 = \begin{pmatrix} x_1 - M^{-1} \sum x_i & x_2 - M^{-1} \sum x_i & \dots & x_M - M^{-1} \sum x_i \\ y_2 - M^{-1} \sum y_i & y_1 - M^{-1} \sum y_i & \dots & y_M - M^{-1} \sum y_i \end{pmatrix}, \quad \mathbf{t} = \begin{pmatrix} t_1 \\ t_2 \\ \vdots \\ t_M \end{pmatrix}.$$

Bias and covariance of the least-squares slowness vector estimate are

$$E\{\hat{\mathbf{S}}\} = \mathbf{X}_1^{-1} \mathbf{X}_2 E\{\mathbf{t}\}, \quad (5.10)$$

$$\text{Cov}\{\hat{\mathbf{S}}\} = \mathbf{X}_1^{-1} \mathbf{X}_2 \text{Cov}\{\mathbf{t}\} (\mathbf{X}_1^{-1} \mathbf{X}_2)^T, \quad (5.11)$$

where E denotes the expectation and Cov the covariance of $\hat{\mathbf{S}}$. If phase data $(\phi_i, i = 1, \dots, M)$ are used, then the factors ω_o^{-1} and ω_o^{-2} should be applied to (5.10) and (5.11), respectively.

The phase angle can be estimated by methods such as the cross-power spectra estimate. Because, however, the phase may be determined only up to an arbitrary multiple of 2π , the conventional least-squares problem (5.9.b) is not easy to implement unless the phase angle can be unscrambled easily and reliably. This problem is not severe for CSS because the orthogonality property (5.7) is used for the estimation.

The phase angle is also subject to random estimation error. In fact it can be shown that the phase estimation error at frequency ω_o is inversely related to the coherence at that frequency (Brillinger, 1981). Although the bias and covariance of the least-squares estimates are inversely proportional to ω_o and ω_o^2 respectively, the low coherence at high frequency (Abrahamson and Bolt, 1987) prevents the use of phase data at high signal frequencies.

The time delay is measured by generalized cross-correlation (Carter, 1981) method between one station and a selected reference station. The resulting time delay estimate, which is the time lag at the cross-correlation peak, is then used as the vector \mathbf{t} . The uncertainty of the time delay estimate is sometimes measured by the width of the cross-correlation peak, which is mainly controlled by the bandwidth of the cross-spectrum and was shown to be unsatisfactory for seismic data (McLaughlin, 1982). Carter ((1981) suggested the use of the magnitude-squared coherence function, which is itself a function that is unknown and requires careful analysis, to calculate estimation uncertainty of the generalized cross-correlation method.

§ 5.2 Implementation of CSS

The estimation of the number of signals, \hat{N} , and of the slowness vectors, $\hat{\mathbf{S}}(\xi_i)$, is based on the eigenvalues and eigenvectors of \mathbf{P}_{u^*} , respectively. An estimator of $\mathbf{P}_{u^*}(\omega_o)$ suggested

by (5.5) and (5.6) is

$$\hat{\mathbf{P}}_{u^*}(\omega_o) = \frac{1}{K} \sum_{k=1}^K \hat{\mathbf{R}}_{u^*}(\omega_k) = \frac{1}{K} \sum_{k=1}^K \hat{\mathbf{T}}(\omega_k, \omega_o) \hat{\mathbf{R}}_u(\omega_k) \hat{\mathbf{T}}^H(\omega_k, \omega_o), \quad (5.12)$$

$$\hat{\mathbf{R}}_u(\omega_k) = \mathbf{u}(\omega_k) \mathbf{u}^H(\omega_k), \quad (5.13)$$

where $\hat{\mathbf{R}}_u(\omega_k)$ is an estimate of the cross-covariance matrix (5.2) at frequency ω_k , and $\hat{\mathbf{T}}(\omega_k)$ is an estimate of the transformation matrix. Normally K , the number of frequencies averaged, is greater than the number of array stations (M), so $\hat{\mathbf{P}}_{u^*}(\omega_o)$ has full rank. The transformation matrix $\hat{\mathbf{T}}$ allows preservation of phase information at the reference frequency ω_o and, as noted in §5.1, at the same time increases the sample size to K .

Note that the cross-spectral matrix estimator with simple frequency-smoothing is

$$\hat{\mathbf{R}}_u(\omega_o) = \sum_{k=-K/2}^{K/2} \alpha_k \mathbf{u}(\omega_o + k\delta\omega) \mathbf{u}^H(\omega_o + k\delta\omega) \quad (5.14)$$

where α_k is the weight of frequency $\omega_o + k\delta\omega$, and $\delta\omega$ is the frequency increment. Without the transformation matrix $\hat{\mathbf{T}}$, (5.12) is simply a special case of (5.14). This interpretation also enables a comparison between CSS and other widely used non-parametric methods such as CV and HR, where estimates of the cross-power spectral matrix are used.

The selection of $\hat{\mathbf{T}}$ is not unique (Wang and Kaveh, 1985; Hung and Kaveh, 1988). A convenient choice used in this study is

$$\hat{\mathbf{T}}(\omega_k, \omega_o) = \begin{pmatrix} e^{i(\omega_k - \omega_o)[\hat{\mathbf{S}}_o \cdot (\mathbf{x}_1 - \mathbf{x}_o)]} & 0 & \dots & 0 \\ 0 & e^{i(\omega_k - \omega_o)[\hat{\mathbf{S}}_o \cdot (\mathbf{x}_2 - \mathbf{x}_o)]} & \dots & 0 \\ \vdots & \vdots & \ddots & \vdots \\ 0 & 0 & \dots & e^{i(\omega_k - \omega_o)[\hat{\mathbf{S}}_o \cdot (\mathbf{x}_M - \mathbf{x}_o)]} \end{pmatrix} \quad (5.15)$$

where $\hat{\mathbf{S}}_o$ is an initial guess of the signal slowness vector. (5.15) is suitable for the case of one signal, which is generally the case in this work. But in the case of multiple signals, it was shown by Wang and Kaveh (1985) that the diagonal focusing matrix (5.15) is appropriate only when the slowness vectors of the multiple signals cluster together. When this is not so,

construction of \mathbf{T} will involve extensive computations (Hung and Kaveh, 1988). Numerous iterations are usually required. The estimated slowness vector is substituted for $\hat{\mathbf{S}}_0$, and the algorithm is repeated until the estimated slowness vector converges.

With a diagonal transformation matrix \mathbf{T} , (5.12) is numerically equivalent to a cross-spectral matrix estimate formed with data lying within a slant time window chosen according to the slowness vector $\hat{\mathbf{S}}_0$ (McLaughlin *et al.*, 1983). In this context, the main difference between CSS and CV or HR methods (applied to a slant window) is in the weight assigned to each eigenvector. We have (McLaughlin, 1982)

$$\hat{P}^{CV}(\mathbf{s}) = \sum_{i=1}^M \hat{\lambda}_i |\mathbf{a}^H \cdot \hat{\mathbf{e}}_i|^2$$

$$\hat{P}^{HR}(\mathbf{s}) = \frac{1}{\sum_{i=1}^M \hat{\lambda}_i^{-1} |\mathbf{a}^H \cdot \hat{\mathbf{e}}_i|^2}$$

$$Q(\mathbf{s}) = \frac{1}{\sum_{i=N+1}^M |\mathbf{a}^H \cdot \hat{\mathbf{e}}_i|^2} = \frac{1}{1 - \sum_{i=1}^N |\mathbf{a}^H \cdot \hat{\mathbf{e}}_i|^2},$$

where $\hat{\lambda}_i$ and $\hat{\mathbf{e}}_i, i = 1, \dots, M$ are the estimated eigenspectra and eigenvectors. In the HR method, an arbitrary damping factor is added to the diagonal elements of (5.9) when $K < M$ (Abrahamson, 1985), so $\hat{\lambda}_i$ is non-zero, $i > K$. This damping factor contributes arbitrariness to the frequency-slowness spectrum estimate, in particular at the slowness close to the signal slowness vector. In CSS, such a damping factor is not required.

Several optimization principles have been suggested (Wax and Kailath, 1983; Wang and Kaveh, 1985) for the estimation of N . Among them are the statistics of AIC (Akaike Information Criteria) and MDL (Minimum Description Length). Based on experience gained in the present study, these statistics do not give appropriate estimates of N for real data in most cases. The size of the dominant eigenvalues relative to the rest of the eigenvalues provides more useful information.

For the case of one signal, the degree of polarization is a useful statistic for the relative separation between the largest eigenvalue and the rest of the eigenspectra. Estimates of

the degree of polarization β^2 are based on the eigenspectra estimate of $\hat{\mathbf{P}}_{u^*}$ (Darragh, 1987),

$$\hat{\beta}^2 = \frac{M(\text{tr}\hat{\mathbf{P}}_{u^*}^2) - (\text{tr}\hat{\mathbf{P}}_{u^*})^2}{(M-1)(\text{tr}\hat{\mathbf{P}}_{u^*})^2}. \quad (5.16)$$

If a wavefield is composed of one signal (i.e. the wavefield is linearly polarized) and the noise level is low, then there will be only one dominant eigenvalue and $\hat{\beta}^2$ is close to 1. If the wavefield is composed of uncorrelated noise, then all the eigenvalues are identical and $\hat{\beta}^2$ is 0. Polarization is also a lower bound on the coherence of the wavefield (Darragh, 1987). This polarization will be estimated later in §7.1 for each selected time window.

§ 5.3 Uncertainties in Estimation

In this section, the uncertainties associated with the slowness estimates are investigated. The slowness vector estimate is the vector $\hat{\mathbf{S}}$ at which $D(\hat{\mathbf{S}})$ in equation (5.8) is a local minimum. Because $D(\mathbf{S})$ is a function of $\{\hat{\mathbf{e}}_i, i = 1, \dots, N\}$, a perturbation to the signal-eigenvector estimates will result in a perturbation to the estimated slowness vector. The approximate first- and second- order moments of the slowness perturbation are given in § 5.3.1.

In practice, earthquake waves travel through the laterally heterogeneous crust beneath the array; the resultant perturbations to the seismic wavefield are the random phase fluctuation and non-planar wavefronts (Aki, 1973; Capon, 1974). It follows that the true array response is not the plane-wave response \mathbf{A} as specified in (5.1). These perturbations, which are not incorporated in (5.1), would invalidate the plane-wave model, prohibit perfect focusing, and lead to discrepancies between the eigenstructure estimated from the data ($\hat{\mathbf{P}}_{u^*}$) and the eigenstructure of \mathbf{P}_{u^*} . It is these discrepancies that contribute to the bias and variance of the slowness vector estimator. Clock errors at each array sensor may be another source of systematic time error besides lateral heterogeneity (see § 4.1).

Perturbation of the estimated eigenstructure from that of the plane-wave model can be separated into a deterministic part, which is due to the non-planar array response, and a

random part, which is due to the random phase fluctuations. The first part causes bias of the slowness estimator, and the second part is responsible for the estimation variance. As an illustration of how non-planar wavefronts and phase fluctuation would perturb the signal subspace, the case of one signal is considered in § 5.3.2. The single signal case is important to the present study because the selection of window described in §4.4 ensures that in each window only one dominant signal exists. It will be shown that for large focusing-frequency ω_o , the slowness estimation bias is small and the expected phase residual is directly related to the deterministic time error.

§ 5.3.1 Asymptotic Mean and Covariance of Slowness Perturbation.

Using an approach similar to that developed by Porat and Friedlander (1986), approximate formulas for the first- and second- order moment of the slowness perturbation caused by an eigenstructure perturbation are derived. The following formulas are based on the first-order Taylor expansion of $\partial D/\partial \mathbf{S}$,

$$E\{\delta \mathbf{S}\} = - \left[\frac{\partial^2 D}{\partial \mathbf{S}^2} \right]^{-1} \left[\frac{\partial^2 D}{\partial \mathbf{S} \partial \Omega} \right] E\{\delta \Omega\} + O(K^{-1}), \quad (5.17.a)$$

$$Cov\{\delta \mathbf{S}\} = \left[\frac{\partial^2 D}{\partial \mathbf{S}^2} \right]^{-1} \left[\frac{\partial^2 D}{\partial \mathbf{S} \partial \Omega} \right] Cov\{\delta \Omega\} \left[\frac{\partial^2 D}{\partial \mathbf{S} \partial \Omega} \right]^T \left[\frac{\partial^2 D}{\partial \mathbf{S}^2} \right]^{-T} + O(K^{-1}). \quad (5.17.b)$$

where

$$\delta \Omega = [Re(\delta \mathbf{e}_1)^T \quad Im(\delta \mathbf{e}_1)^T \quad Re(\delta \mathbf{e}_2)^T \quad Im(\delta \mathbf{e}_2)^T \quad \dots \quad Re(\delta \mathbf{e}_N)^T \quad Im(\delta \mathbf{e}_N)^T]^T$$

D is defined in (5.8). K is the number of frequencies smoothed. $\delta \mathbf{S} = \hat{\mathbf{S}} - \mathbf{S}(\xi)$ is the perturbation to the slowness vector estimate. $\delta \Omega$ is a $(2MN \times 1)$ column vector consisting of the real and imaginary parts of the signal-eigenvector perturbation $\delta \mathbf{e}_i$. The vector $E\{\delta \Omega\}$ and matrix $Cov\{\delta \Omega\}$ are the mean and covariance of the signal-eigenvector perturbation. The number of signals N is assumed known.

In the case of no systematic time error, appropriate forms for $E\{\delta \Omega\}$ and $Cov\{\delta \Omega\}$ are given by Brillinger (1981). Assuming that the estimate $\hat{\mathbf{P}}_{u^*}$ is only slightly different from

the true \mathbf{P}_{u^*} gives

$$\hat{\mathbf{P}}_{u^*} = \mathbf{P}_{u^*} + \varepsilon \mathbf{G}, \quad (5.18)$$

where elements of \mathbf{G} are zero-mean, mutually-independent, complex, normal random variables and $\varepsilon \ll 1$. Suppose $\{\lambda_i, \mathbf{e}_i, i = 1, M\}$ and $\{\hat{\lambda}_i, \hat{\mathbf{e}}_i, i = 1, M\}$ are the eigenstructure of \mathbf{P}_{u^*} and $\hat{\mathbf{P}}_{u^*}$, respectively. Then for eigenvectors associated with distinct eigenvalues λ_i we have (Brillinger, 1981),

$$E\{\hat{\mathbf{e}}_i\} = \mathbf{e}_i + o(K^{-1})$$

$$Cov\{\hat{\mathbf{e}}_i, \hat{\mathbf{e}}_j\} = \frac{\lambda_i}{K} \delta_{ij} \sum_{\substack{l=1 \\ l \neq i}}^M \frac{\lambda_l}{(\lambda_i - \lambda_l)^2} \mathbf{e}_l \mathbf{e}_l^H + o(K^{-1}). \quad (5.19)$$

$$Cov\{\hat{\mathbf{e}}_i, \tilde{\mathbf{e}}_j\} = -\frac{\lambda_i \lambda_j}{K(\lambda_i - \lambda_j)^2} (1 - \delta_{i,j}) \mathbf{e}_i \mathbf{e}_j^T + o(K^{-1}).$$

where

$$i, j = 1, \dots, N.$$

$\delta_{i,j}$ is the Kronecker delta. So, when deterministic time errors do not exist, the signal-eigenvector estimators are asymptotically unbiased and hence the slowness estimator of CSS is also asymptotically unbiased. The variance of the eigenvector estimate depends on the signal/noise ratio and the separation between the signal eigenvalues. It should be noted that the formulas given above are for eigenvectors associated with the distinct eigenvalues, i.e. the signal-subspace, only. For repeated noise eigenvalues, because of the indeterminacy of the corresponding noise eigenvectors, the variability of the estimate is infinitely large. This, in principle, implies that slowness estimates from methods such as CV and HR, which use the noise- as well as the signal- eigenvectors, will tend to give a larger estimation variance than the variance of the estimator using only the signal eigenvectors.

For the case of one signal, appropriate forms for $E\{\delta \mathbf{e}\}$ and $Cov\{\delta \mathbf{e}\}$, which include deterministic as well as random perturbation, are given in § 5.3.2.

Note that (5.17) is based on a first-order expansion of $\partial D / \partial \mathbf{S}$. An extra term that involves the second-order moment $Cov\{\delta \Omega\}$ would be added to (5.17.a) (Porat and Friedlander,

1986) if warranted by the amount of perturbation. In this case, the slowness estimator is biased. Porat and Friedlander (1986) used formulas derived from the second-order Taylor expansion to analyze the (theoretical) asymptotic, relative efficiency of the MUSIC algorithm, assuming there is no systematic time error.

It is interesting to note that (5.17.a) and (5.17.b) are similar in forms to (5.10) and (5.11). This is not surprising, as both CSS and least-squares methods look for slowness values that minimize the objective functions, $D(\mathbf{S})$ and the sum of squared errors.

§ 5.3.2 Single Signal Case

In this section, systematic time error and random phase fluctuation are introduced into the plane-wave model of (5.1) for the case of one signal. The theoretical discrepancy between the signal-eigenvector of this perturbed model and that of the plane-wave model is derived. Note that, for the one signal case, the signal-eigenvector is identical to the array response vector.

Fourier coefficients of the array data, including systematic time errors and random phase fluctuations, are (see equation (5.1))

$$\mathbf{u}(\omega_k) = \mathbf{A}'(\omega_k) \mathbf{d} + \mathbf{n}(\omega_k)$$

with

$$A'_i(\omega_k) = \frac{1}{\sqrt{M}} e^{-i\omega_k[\mathbf{S}(\boldsymbol{\xi}) \cdot (\mathbf{x}_i - \mathbf{x}_0) + \delta t_i] + i\delta\phi_i(\omega_k)}.$$

where δt_i is the deterministic time deviation at station i from a plane wave with slowness vector $\mathbf{S}(\boldsymbol{\xi})$. $\delta\phi_i(\omega_k)$ is the random phase error at frequency ω_k . Slowness dependence of δt_i is not excluded. The steered Fourier coefficients are

$$\begin{aligned} \mathbf{u}^*(\omega_o) &= \mathbf{T} \mathbf{A}' \mathbf{d} + \mathbf{T} \mathbf{n} \\ &= \begin{pmatrix} e^{-i\omega_k \delta t_1 + i\delta \phi_1(\omega_k)} & 0 & \dots & 0 \\ 0 & e^{-i\omega_k \delta t_2 + i\delta \phi_2(\omega_k)} & \dots & 0 \\ \vdots & \vdots & \ddots & \vdots \\ 0 & 0 & \dots & e^{-i\omega_k \delta t_M + i\delta \phi_M(\omega_k)} \end{pmatrix} \mathbf{A}(\omega_o) \mathbf{d} + \mathbf{T} \mathbf{n} \end{aligned}$$

Here, focusing at the true slowness vector $\mathbf{S}(\xi)$ is assumed. When steered to the wrong slowness vector \mathbf{S}_0 , an additional phase error of $(-\omega_k(\mathbf{S}(\xi) - \mathbf{S}_0) \cdot \mathbf{x}_i)$ will be introduced into the diagonal elements. On forming the steered cross-covariance matrix and averaging over K frequencies, we obtain,

$$(\hat{\mathbf{P}}_{\mathbf{u}^*})_{ij} = \frac{1}{K} e^{-i\omega_o \mathbf{S}(\xi) \cdot (\mathbf{x}_i - \mathbf{x}_j)} \sum_{k=1}^K R_d(\omega_k) e^{-i\omega_k(\delta t_i - \delta t_j)} e^{i(\phi_i(\omega_k) - \phi_j(\omega_k))} + \sigma \quad (5.22)$$

$i, j = 1, \dots, M$. Assume that the difference in random phase error $\phi_i(\omega_k) - \phi_j(\omega_k)$ is small, then $e^{i(\phi_i(\omega_k) - \phi_j(\omega_k))} \approx 1 + C_{ij}$, where C_{ij} is a small random complex number. We have,

$$(\hat{\mathbf{P}}_{\mathbf{u}^*})_{ij} = \frac{1}{K} e^{-i\omega_o \mathbf{S}(\xi) \cdot (\mathbf{x}_i - \mathbf{x}_j)} \{R_e e^{-i\omega_o(\delta t_i - \delta t_j)}\} + \mathbf{G}_{ij} + \sigma, \quad (5.23)$$

with

$$R_e e^{-i\omega_o(\delta t_i - \delta t_j)} = \sum_{k=1}^K R_d(\omega_k) e^{-i\omega_k(\delta t_i - \delta t_j)}. \quad (5.24)$$

$$\mathbf{G}_{ij} = \frac{1}{K} e^{-i\omega_o \mathbf{S}(\xi) \cdot (\mathbf{x}_i - \mathbf{x}_j)} \sum_{k=1}^K R_d(\omega_k) e^{-i\omega_k(\delta t_i - \delta t_j)} C_{ij}.$$

The random matrix \mathbf{G} is the result of random phase fluctuation. Elements of \mathbf{G} are small and assumed to be mutually independent with a zero-mean, complex, normal distribution. In matrix notation,

$$\hat{\mathbf{P}}_{\mathbf{u}^*} = \mathbf{A}_e R_e \mathbf{A}_e^H + \mathbf{G} + \sigma \mathbf{I}, \quad (5.25)$$

$$(\mathbf{A}_e)_i = e^{-i\omega_o \mathbf{S}(\xi) \cdot (\mathbf{x}_i - \mathbf{x}_o) - i\omega_o \delta t_i}.$$

On comparison of (5.23) to (5.6) with $N = 1$,

$$(\mathbf{P}_{\mathbf{u}^*})_{ij} = \frac{1}{K} e^{-i\omega_o \mathbf{S}(\xi) \cdot (\mathbf{x}_i - \mathbf{x}_j)} \sum_{k=1}^K R_d(\omega_k) + \sigma. \quad (5.26)$$

We find the effects of deterministic time errors are (1) a reduction in signal/noise ratio, as $R_e = |\sum_{k=1}^K R_d(\omega_k) e^{-i\omega_k(\delta t_i - \delta t_j)}| \leq \sum_{k=1}^K R_d(\omega_k)$; and (2) a phase shift of $(-\omega_e \delta t_i)$ in the signal-eigenvector.

In equation (5.24), $R_d(\omega_k)$ acts as the weight at frequency ω_k in determining the deterministic phase shift $-\omega_e \delta t_i$. If the power spectra of the incident signal is white, then $\omega_e = \sum_{k=1}^K \omega_k / K$, i.e. ω_e equals the the mean frequency of the bandwidth considered. If the power spectrum is broad-band but with most of the power concentrated in a limited band, then ω_e is approximately the mean frequency of that band. Note that ω_e is independent of the focusing frequency. The deterministic time error does not directly translate into the phase delay through the frequency ω_o , but, instead, it translates through the effective frequency ω_e which depends only on the incident signal power distribution.

(5.25) has a form similar to (5.18), therefore (5.19) can be used to determine the first- and second- order moments of the signal eigenvector $\hat{\mathbf{e}}_1$ of $\hat{\mathbf{P}}_{u^*}$. They are

$$E\{\hat{\mathbf{e}}_1\} = \mathbf{A}_e + O(K^{-1})$$

$$Cov\{\hat{\mathbf{e}}_1, \hat{\mathbf{e}}_1\} = \frac{\lambda_1}{K} \sum_{\substack{i=1 \\ i \neq 1}}^M \frac{\lambda_i}{(\lambda_1 - \lambda_i)^2} \mathbf{e}_i \mathbf{e}_i^H + O(K^{-1}). \quad (5.27)$$

$$Cov\{\hat{\mathbf{e}}_1, \hat{\mathbf{e}}_j\} = \mathbf{0} + O(1/K)$$

Here, $\{\lambda_i, \mathbf{e}_i, i = 1, \dots, M\}$ is the eigenstructure of $\mathbf{A}_e R_e \mathbf{A}_e^H + \sigma \mathbf{I}$.

The first equation of (5.27) indicates that the signal-eigenvector estimate is asymptotically biased. It follows that the slowness estimator of CSS is also asymptotically biased. The mean of the slowness estimate is obtained by substituting the first equation of (5.27) into (5.17.a),

$$E\{\hat{\mathbf{S}}\} = \mathbf{S}(\boldsymbol{\xi}) + \omega_o^{-1} \mathbf{X}_1^{-1} \mathbf{X}_2 \Theta \quad (5.29)$$

$$(\Theta)_i = \sin(\omega_e \delta t_i - \phi_1) - \sin(\phi_1)$$

where ϕ_1 is the phase angle of the first element of $\hat{\mathbf{e}}_1$. Note that (5.28) has the same \mathbf{X}_1 and \mathbf{X}_2 as (5.10). This is consistent with the least-squares interpretation of the CSS method. The differences in the mean and covariance of the slowness estimate obtained from the CSS method and the least-squares method (see (5.10) and (5.11)) are the factor ω_o^{-1} and the error term Θ . These two differences provide some advantages of CSS over the traditional least-squares methods in reducing the bias introduced by systematic time error. The error term Θ is always less than 2.0 and the factor ω_o^{-1} in (5.28) would significantly reduce the bias if its value is large. However, the trade-off in using a large value of ω_o is that the rate of convergence is slow. In practice some accuracy is sacrificed for a reduction in the number of iterations required.

The array configuration also plays an important role in determining the amount of bias introduced by systematic time errors (Bates and Kanasewich, 1985). A large matrix norm $\|\mathbf{X}_1^{-1}\mathbf{X}_2\|$ would offset the bias-reduction effect of a large ω_o .

When ω_o is large and $\|\mathbf{X}_1^{-1}\mathbf{X}_2\|$ is a reasonably small quantity, the bias of the slowness estimation will be small. In this case, little deterministic time error will be absorbed into the slowness estimate, so the mean phase residual is close to $\omega_e\delta t_i$.

In summary, the above demonstrates that, based on a first-order expansion and the assumption of a large ω_o , the bias of the slowness estimator introduced by the systematic time error is small and the expected prediction phase error at station i is $\omega_e\delta t_i$. In §4.3, a SMART1 subarray in which travel-time delay approximately satisfied a plane-wave front was selected for slowness estimation. This selection ensures that the first-order expansion approximately holds and the above results are valid for the present study.

CHAPTER 6

ESTIMATION OF THE SEISMIC SOURCE RUPTURE PROCESS

In this chapter, the computational procedures to perform source mapping and to infer the mapping uncertainty are given. First, exact formulas for source mapping in a crustal model with a velocity gradient are derived. In § 6.2, a simple way to compute the approximate precision of the estimated source parameters is described. Then in § 6.3, the effects of a three-dimensional crustal velocity structure, which includes a sedimentary basin and a proposed slab structure, on the horizontal slowness vector of a seismic ray are studied. It will be shown that a slab of material with higher velocity than the surrounding rock could explain the observed arrival time pattern at the SMART1 array for the earthquake (Event 43) described in Chapter 4. It will also be shown that the underlying sedimentary basin, acting as an optical lens, rotates the incident ray ‘clockwise’ and the rays are refracted at the dipping basin-basement interface so they reach the array at steeper incidence angles. More importantly, the differing basin thickness under each station is not large enough to distort the wavefront.

§ 6.1 Source Mapping in a Gradient-Velocity Model

This section returns to the originally posed problem of inverse mapping for the seismic source rupture process. A simple gradient-layer over half-space velocity model is adopted so that exact formulas for source position and rupture time can be derived. Because of their simplicities, these analytic forms provide important insights into the problem of source mapping. Such exact relations are in general not realistic for complicated geological structures in the actual crust. But the derivation in this section illustrates the basic principles needed for source mapping in a more realistic earth model.

The convention for the coordinate system adopted here corresponds to that used in

Aki and Richards (1980) (Figure 6.1). Because the measured horizontal slowness vector provides only two constraints on the source position, it is necessary to assume that all sources lie on a fault plane of strike λ and dip δ that passes through the hypocenter (X_o, Y_o, Z_o) . This assumption reduces the degrees of freedom of source position from three to two. The vertical component of the slowness vector does not provide the third constraint, it only provides information on the seismic velocity at the array. Location of the source point ξ can thus be specified by two parameters, namely, the epicentral distance Δ , and depth Z_s ; or more appropriately, the distances along strike (s) and down dip (d) from the hypocenter (X_o, Y_o, Z_o) :

$$\xi = (s \cos \lambda - d \sin \lambda \cos \delta + X_o, s \sin \lambda - d \cos \lambda \cos \delta + Y_o, d \sin \delta + Z_o). \quad (6.1),$$

Only the direct P- and S- waves are considered here; secondary arrivals reflected from crustal boundaries such as the Mohorovičić discontinuity and head waves are not included.

The basic method of source mapping is as follows. A ray with slowness parameter $S = \sqrt{S_x^2 + S_y^2}$ is projected from the array center in a direction opposite to the measured wave propagation direction $\psi = \tan^{-1}(S_x/S_y)$. Intersection of this ray with the fault plane gives the source location ξ . Because the seismic ray is confined to the incidence plane in a depth-dependent-only velocity model, the source point lies on the straight line on that fault plane which is intersected by the incidence plane. This straight line satisfies the equation

$$\Delta = \alpha + \gamma Z, \quad (6.2)$$

where

$$\left\{ \begin{array}{l} \alpha = \frac{d}{a \cos \psi + b \sin \psi} \\ \gamma = \frac{-c}{a \cos \psi + b \sin \psi} \end{array} \right\}, \left\{ \begin{array}{l} a = \sin \lambda \sin \delta \\ b = -\cos \lambda \sin \delta \\ c = \cos \delta \\ d = aX_o + bY_o + cZ_o \end{array} \right\}.$$

Δ is the surface distance from a point on this line to the array center (Figure 6.2), (a, b, c) is the unit normal vector to the fault plane. The fault plane satisfies the equation $a X +$

$bY + cZ = d$. It can be shown that, given a velocity model $(A + BZ)$ and a ray parameter S , the ray path is an arc of a circle (Bullen and Bolt, 1985; Lee and Stewart, 1981) that satisfies

$$(\Delta BS + (\sqrt{1 - S^2 A^2})^2 = 1 - S^2(A + BZ)^2. \quad (6.3)$$

The intersection point between the ray path and the fault plane is thus obtained by solving (6.2) and (6.3) to yield

$$Z_s = \frac{-h_2 \pm \sqrt{h_2^2 - 4h_1 h_3}}{2h_1}, \quad (6.4)$$

$$\Delta_s = \alpha + \gamma Z_s, \quad (6.5)$$

where

$$h_1 = \gamma^2 + 1,$$

$$h_2 = 2 \left(\frac{A}{B} + \alpha\gamma + \frac{\gamma}{S} \sqrt{1 - S^2 A^2} \right),$$

$$h_3 = \alpha^2 + \frac{2\alpha}{BS} \sqrt{1 - S^2 A^2}.$$

A solution does not exist if the argument of the square root in (6.4) is negative, or geometrically the straight line does not intersect the circle. Otherwise, there are two solutions. One of the solutions may be physically unreal, either too deep or negative.

Transformation of the source depth to (s, d) through (6.1) and (6.5) yields

$$\begin{aligned} \begin{pmatrix} s \\ d \end{pmatrix} &= \frac{1}{\sin \lambda \sin \delta} \begin{pmatrix} \sin \delta & -\cos \lambda \cos \delta \\ 0 & \sin \lambda \end{pmatrix} \begin{pmatrix} \sin \psi & 0 \\ 0 & 1 \end{pmatrix} \begin{pmatrix} \alpha & \gamma \\ 0 & 1 \end{pmatrix} \begin{pmatrix} 1 \\ Z_s \end{pmatrix} \\ &\quad - \frac{1}{\sin \lambda \sin \delta} \begin{pmatrix} \sin \delta & -\cos \lambda \cos \delta \\ 0 & \sin \lambda \end{pmatrix} \begin{pmatrix} Y_o \\ Z_o \end{pmatrix}, \end{aligned}$$

or

$$s = \frac{\alpha \sin \psi}{\sin \lambda} + Z_s \left(\frac{\gamma \sin \psi}{\sin \lambda} - \frac{1}{\tan \lambda \tan \delta} \right) - \left(\frac{Y_o}{\sin \lambda} - \frac{Z_o}{\tan \lambda \tan \delta} \right), \quad (6.6)$$

$$d = \frac{Z_s - Z_o}{\sin \delta}. \quad (6.7)$$

§ 6.2 Uncertainties of Estimation

Even for a simple velocity model such as the one given in the previous section, the source position and rupture time are nonlinear functions of the slowness vector (S_x, S_y) , the fault strike λ , the fault dip δ , and the velocity model (see equations (6.6) and (6.7)). Uncertainty associated with these variables will be carried into the source estimates in a complicated fashion. Because of this nonlinearity of source mapping, the assessment of uncertainty will not be exact. The approximate variances of the source estimates are obtained through a first order Taylor expansion (Jenkins and Watts, 1968, p76),

$$Cov\{\xi\} = \left[\frac{\partial \xi}{\partial \mathbf{v}} \right] Cov\{\mathbf{v}\} \left[\frac{\partial \xi}{\partial \mathbf{v}} \right]^T \quad (6.8)$$

where

$$\mathbf{v} = (S_x, S_y, \lambda, \delta, A, B, X_0, Y_0, Z_0)^T$$

$$\xi = (s, d, \tau)^T$$

$$\left[\frac{\partial \xi}{\partial \mathbf{v}} \right]_{ij} = \frac{\partial \xi_i}{\partial v_j}$$

These expressions are valid for a small perturbation $\delta \mathbf{v}$ to the vector \mathbf{v} .

The partial derivatives were evaluated numerically. For the case of a gradient-layer crustal model, exact expressions for the partial derivative can be obtained were used to check the accuracy of the numerical differentiation in §7.3.

§ 6.3 The Three-Dimensional Velocity Model Adopted

A three-dimensional P- and S- velocity model was constructed using information from several studies. A north-south profile of this three-dimensional model is given in Figure 6.3. The model consists of 5 gradient-velocity blocks and four interfaces across which velocity is discontinuous or the velocity gradient changes. Well-logging data (Anderson and Tang, 1989) from a site outside the subarray provide the P- and S- velocity of the topmost 150 meters which include velocity blocks 4 and 5. The three-dimensional model

(Yeh, 1987) obtained from inversion of travel-time data (see also Figure 3.3) provides the velocity structure below 5 km depth (block 1). The velocity gradient in this block is estimated from Figure 3.3. Two seismic refraction studies (Chiang, 1976; Wen and Yeh, 1984) provide the sediment thickness and the P-velocity within and immediately below the basin. A Poisson ratio of 0.30 is used to obtain the S-velocity at the bottom of the basin and immediately below the basin at a depth of 0.38 km.

The influence of the proposed slab-like inhomogeneity on seismic rays arriving at the SMART1 array was studied by adding a east-west striking 2-D slab to the 3-D model described above. The dip of this slab was 60 degrees to the north. There was a discrepancy of several km in the location of the slab inferred from the two separate studies of the geomagnetic anomalies by Yu and Tsai (1979) and Hsu (1987); in this work the slab location given in Yu and Tsai was used. Depth and width of this slab were 1.7 km and 4.7 km, respectively. Since information of the S-velocity in the slab was unavailable, a hopefully reasonable value of 3.5 km/sec was arbitrarily assigned. It is acknowledged that, because of the lack of local high-resolution studies, the assumed slab geometry, location, and S-velocity may deviate from the actual structure. However, the essential purpose of this calculation was to understand how a proposed slab-like inhomogeneity would affect the travel times of S-waves arriving at the SMART1 array. Quantitative prediction of other wave phenomena, such as diffraction, in addition to the travel times of geometrical rays would require a more detailed knowledge of the inhomogeneities.

§ 6.4 Effects of the Basin and the Proposed Slab

Using the above crustal model, rays were traced from a number of different source points on the fault plane to the SMART1 array. The case of three source points is described here (see Figure 6.4). The three source points are roughly at an azimuth of 145 degrees and a distance of 7 km from the SMART1 array. The first source point is located close to the source position on the fault that radiates the selected S-phase whose arrival times were

estimated in §4.3.

Figure 6.4 shows the endpoints of a ray tube originating from these 3 source points. The small solid triangles indicate rays which do not travel through the slab and the large triangles denote rays that pass through the slab. The inner- and middle- rings of the array can be divided into two regions, one being 'hit' by rays passing through the slab, the other not. Most of the southeast quadrant stations used for the source study are situated in the latter region. A transition zone lies between the two regions in which both types of seismic rays arrived within 0.1 sec of each other. Ray paths to this transition zone either travel a small distance within the slab or stay just above the slab's upper corner. The transition zone would move south if the slab were displaced southward.

The horizontal slowness vector of the seismic rays predicted by ray tracing from the first source point is plotted in Figure 6.5.a. Figure 6.5.b is the result from a 1-D model, obtained by replacing the basement interface of the basin by a flat surface at 0.38 km depth and removing the slab from the velocity model. The predicted incidence angle at the Earth's surface is only a few degrees. The corresponding travel times are shown as contours in Figure 6.6. One of the two rays in the transition zone is not included in Figure 6.6, to make the contour look more regular. In the southeast quadrant, where rays are not affected by the slab, travel times display a plane wavefront. This result verifies the insignificance of wavefront distortion due to the variation of basin thickness in the southeast quadrant. The general effects of the basin on seismic rays, in relation to those predicted by the 1-D model, are the 'clockwise' rotation of the ray azimuth and the decrease of the horizontal slowness. This clockwise rotation is opposite to the sense of the observed rotation in Figure 4.4. Note also that both components of the horizontal slowness vector vary less than 0.001 sec/km across the southeast quadrant.

The slab's effects on seismic rays, as noted in the northwest quadrant of Figures 6.5 and 6.6, are the 'counterclockwise' rotation of the ray direction and the decrease of the horizontal slowness. Comparison of the arrival time contour in Figure 6.6 to the observed

arrival time contours given in Figure 4.4 suggests that a slab-like inhomogeneity used here is a plausible cause for the observed arrival times. However, this 3-D subsurface model predicts a larger counterclockwise rotation of the wave direction and a larger horizontal slowness than the observed slowness. These disagreements may be due to the discrepancy between the true velocity and the assumed velocity in the slab, or between the true geometry and the assumed slab geometry.

Additional fits by the present trial and error process were not pursued in this study, because the main focus is on the source process. Determination of the detailed properties of this structural inhomogeneity is in principle achievable given the large number of events at different azimuths that have been recorded by the SMART1 array.

It is important to note that the above model calculations demonstrate the potentially large bias and uncertainty that may occur because of unknown lateral inhomogeneities in the actual earth. The dipping interface gives a less severe error in the source process estimates and its existence is also more difficult to detect. If the slab structure were not recognized and the array were installed entirely in the northeast quadrant, then the measured slowness vector would give a source position almost due east, which is 45 degrees away, and an estimated source depth greater than 40 km. It is fortunate that the aperture of the SMART1 array was large enough to detect the existence of such a slab structure. In the remaining analysis, it will be assumed that there are no other heterogeneities along the ray paths which would produce a similar large bias in the source estimate.

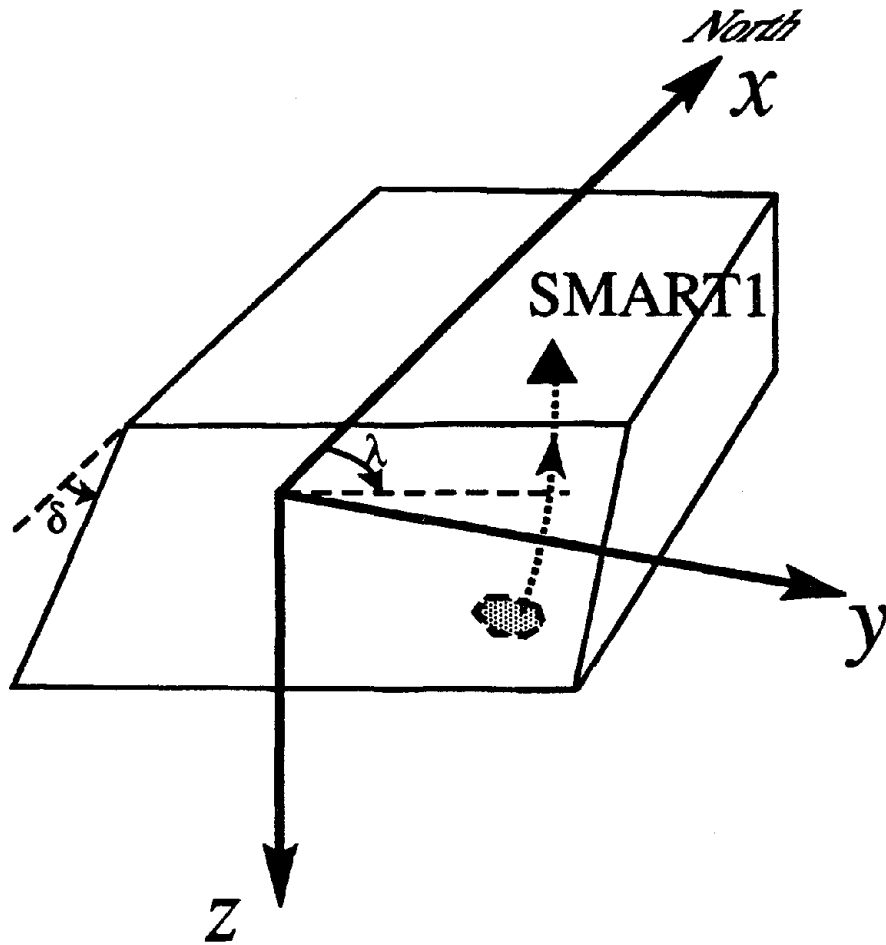


Figure 6.1 Definitions of the coordinate system, fault strike λ , and fault dip δ . The positive x -axis points toward the North, y -axis toward the East. Strike is measured clockwise from the North.

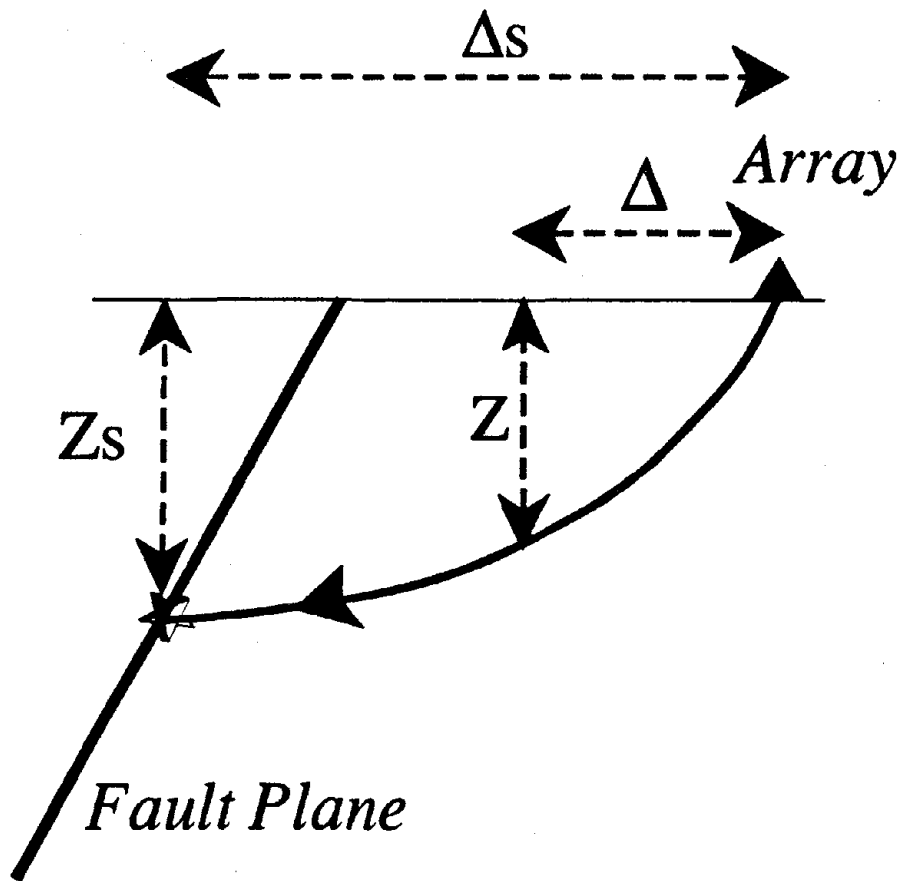


Figure 8.2 Illustration of source mapping in a gradient-velocity model.

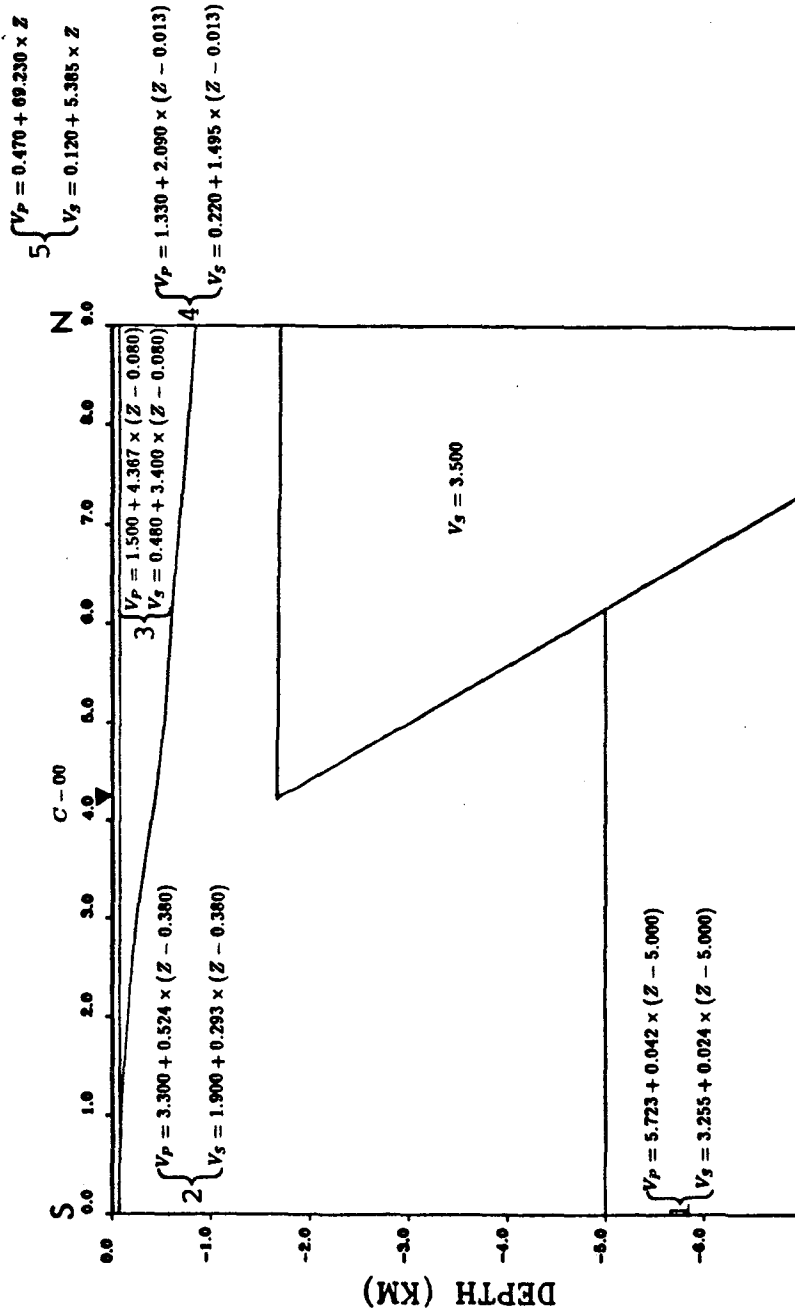


Figure 6.3 A North-South profile of the three-dimensional crustal velocity model. This profile passes through the SMART1 station C-00. Numbers indicate model blocks.

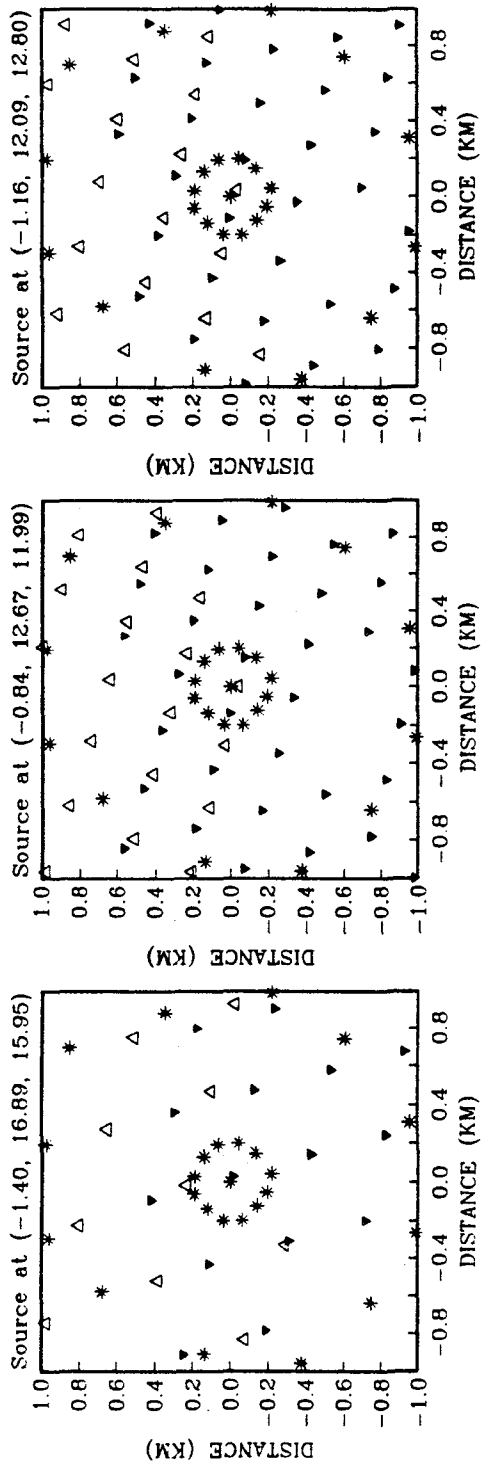


Figure 6.4 Endpoints of a ray tube originating at three different points on the fault plane. The source positions (in km) are given at the top of each diagram. Note that the center coordinate of SMART1 array is (7.2, 7.2, 0.0). The stars indicate the inner and middle ring stations. Solid triangles denote rays that do not travel through the slab. Open triangles denote rays that pass through the slab.

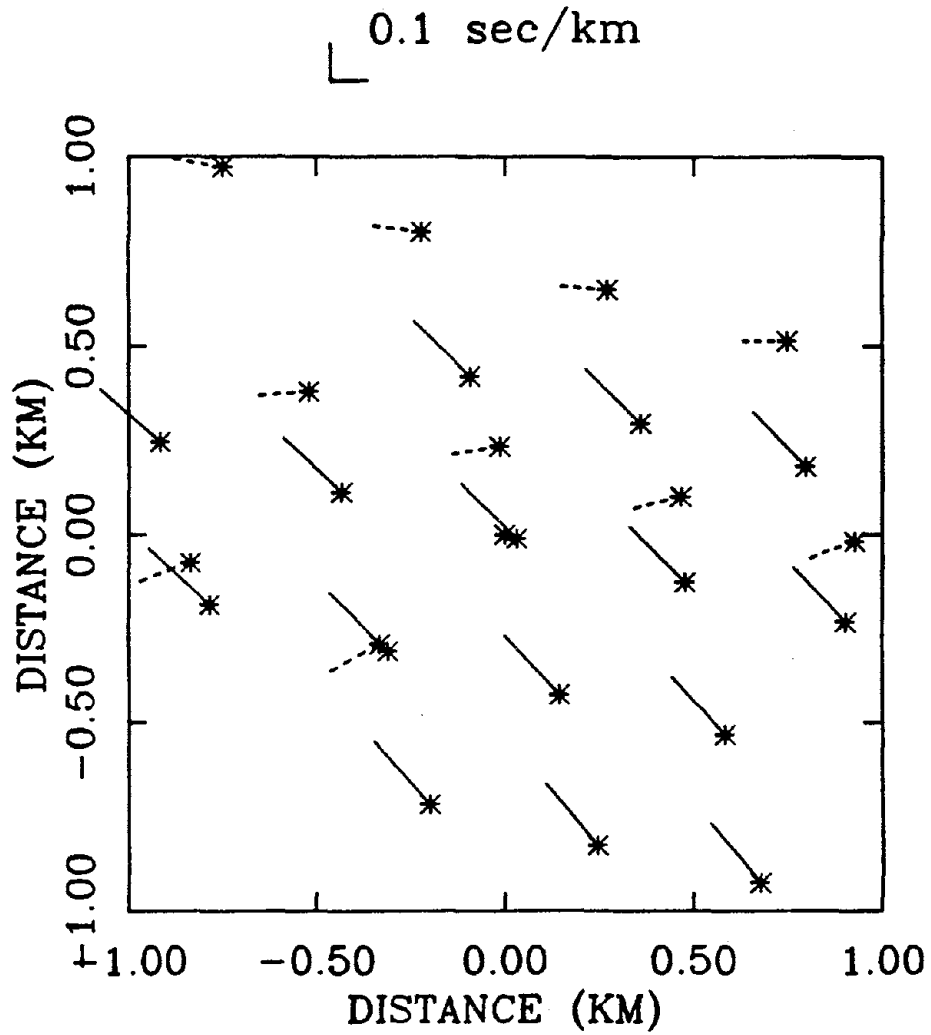


Figure 6.5 (a) Slowness vectors at the array for rays in the first diagram of Figure 6.4. The solid lines indicate the slowness vectors of rays that do not travel through the slab. Slowness vectors of rays that pass through the slab are denoted by dashed lines. The stars indicate the endpoints of these rays.

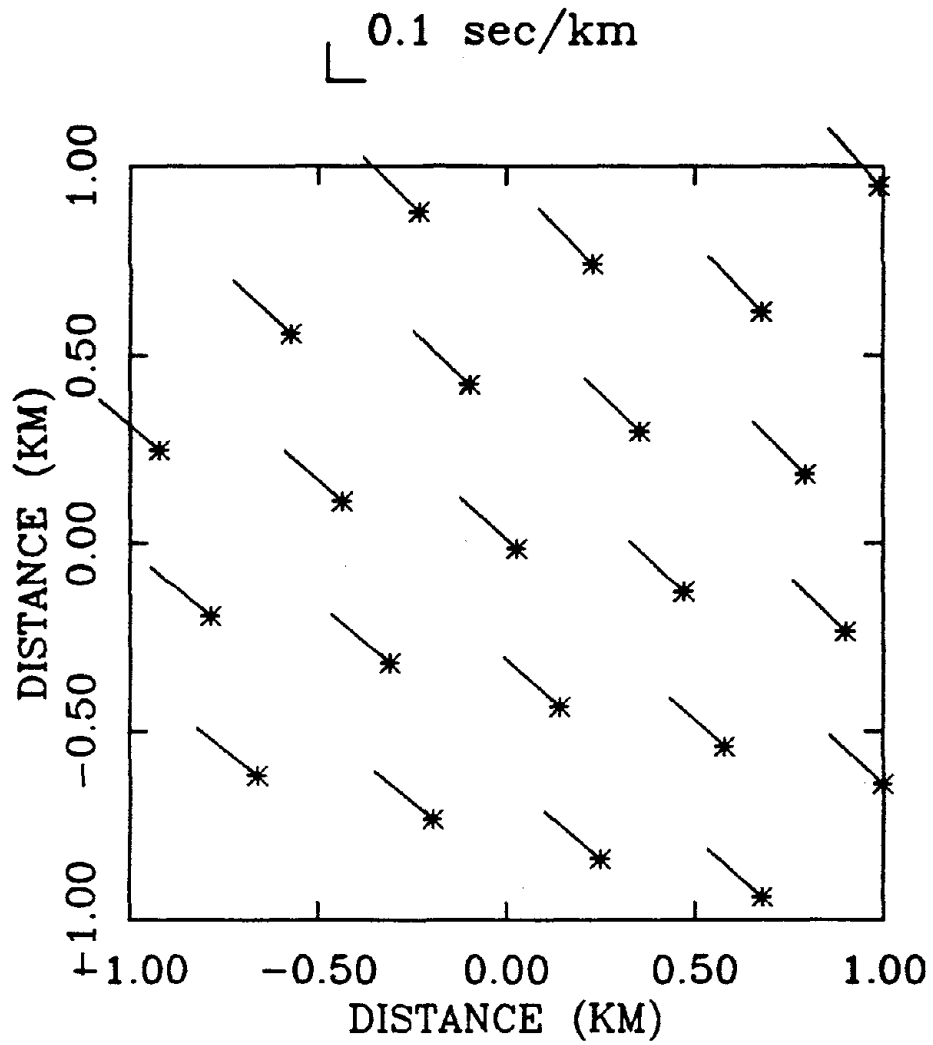


Figure 6.5 (b) Slowness vectors at the array for rays propagating through the one-dimensional crustal velocity model described in the text. The stars indicate the endpoints of rays.

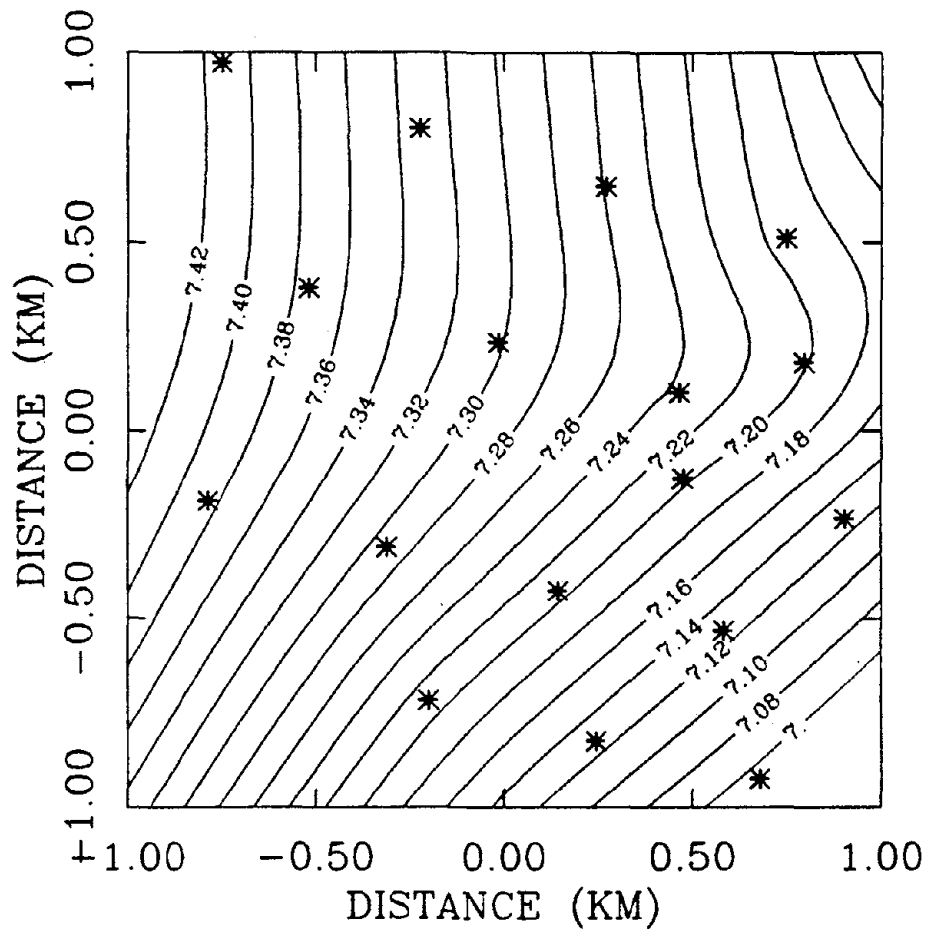


Figure 6.6 Contour of calculated travel times for rays in the first diagram of Figure 6.4. The stars indicate the endpoints of rays.

CHAPTER 7

THE SOURCE PROCESS OF THE JULY 30, 1986 EARTHQUAKE

§ 7.1 Slowness Vector Estimates

The slowness estimation of P- and S-wave was achieved in two steps. First, seismograms were aligned to a reference slowness vector and normalization was performed, as discussed in Chapter 4. Then, the array analysis method CSS was used to estimate the slowness vector of the aligned wavefield. The slowness vector of the signal was calculated as the vector sum of the reference vector and the estimated slowness vector. A 9-station subarray was used (Figure 7.1). Acceleration records (Figure 7.2) at these nine stations were aligned to the slowness vector $(0.1314, -0.165)$ and $(0.079, -0.065)$ sec/km on the horizontal and the vertical components, respectively. The distance shown in Figure 7.2 is the projected distance along the reference slowness vector. Seven time windows on the NS and EW components were selected for computation of S-wave slowness vectors. The windows on the NS component do not coincide in time with those on the EW component. Three windows on the vertical component were chosen for the P-wave analysis. All windows were 0.64 sec long. This duration was specifically chosen as 64 times the digitization time step (0.01 sec) because the Fast Fourier Transform algorithm, which was used to calculate Fourier coefficients, requires the number of data points to be a power of 2. In the following discussion each window was denoted by a character and a number. The character indicates the component, the number denotes the order of the windows.

In this study, the problem of multi-signals was avoided intentionally. One reason is that the 0.64 sec window used is short enough to assign an accurate arrival time to the recorded signal, but not long enough to include completely more than one signal. The other reason is that, for multiple signals, construction of the transformation matrix T (see equation (5.3)) takes much more computational effort than it takes for the one signal case (Hung

and Kaveh, 1988). In addition, for the one signal case, the interpretation of the signal eigenvector is straightforward and the time residuals can also be calculated (see §5.3.2). However, the single-signal situation is not always valid, in particular when the source-array configuration is such that seismic signals from two different slipping patches on the fault arrive almost simultaneously. The appropriate transformation matrix then has to be used. In the present case of earthquake Event 43, the single-signal assumption was confirmed by the dominance of one eigenvalue in the estimated eigenspectra.

Each window was tapered and the constant DC term was calculated and removed. Fifteen frequencies, at an interval of 1.56 Hz, were used in the analysis. This frequency range coincides with the instrument response of the SMART1 accelerometers (see §4.1). The focusing frequency ω_0 was set at the mean frequency, 12.5 Hz. Slowness was estimated by searching over a grid of points on the slowness plane at an equal interval of 0.001 sec/km. It took less than 10 iterations to obtain convergence. The Fourier amplitude spectrum of each window is shown in Figure 7.3. In some windows of the horizontal components (for examples, windows E1 and E2), the Fourier spectra were deficient in the frequency range of 2 to 5 Hz compared to the typical acceleration spectra.

§ 7.1.1 S Windows.

The first window (windows *N0* and *E0*) on the NS and EW components was selected well before the arrival of the first S-waves. The energy included in these two windows is interpreted as mostly random scattered energy and is most likely signal-generated noise. The estimated eigenspectra are plotted in Figure 7.4. Star symbols denote the eigenvalues in window 0, representing the pre-S noise level. The estimates of polarization $\hat{\beta}^2$ are given in Table 7.1 (see §5.2 for definition).

NS Component. In all six windows of the NS component, the second largest eigenvalue $\hat{\lambda}_2$ is close to the largest eigenvalue in window *N0*. Except for windows N1 and N4, the largest eigenvalue $\hat{\lambda}_1$ in each window is well separated from the rest of the eigenvalues.

These two observations suggest that only one signal is present within each window. The small value of $\hat{\lambda}_1$ in window N1 is perhaps due to the fact that the signal power is not as high as in the other windows (see Figure 7.3). However, this is not the case in window 4 in which the Fourier amplitude spectrum has the same level as in the other windows. The value of $\hat{\beta}^2$ in window N0 is 0.16, agreeing with the interpretation that window N0 consists mostly of random noise. Values of $\hat{\beta}^2$ in the other six windows are well above 0.16. These $\hat{\beta}^2$ values, interpreted as the lower bound of coherence, agree with the visual similarity of the Fourier spectra from each station, especially in the frequency band where the amplitude is large.

EW Component. Windows E1 and E2 also show well-separated eigenvalues. In windows E5 and E6, $\hat{\lambda}_1$ is quite small and separation between the eigenvalues is also small. The value of $\hat{\beta}^2$ (Table 7.1) in window E5 is close to the $\hat{\beta}^2$ value in window E0. This low $\hat{\beta}^2$ value agrees with the observation that there is little or no coherent seismic wave arrival in window E5.

Figures 7.5 and 7.6 show the contour of the reciprocal projection length Q as a function of the two horizontal slowness components (see §5.1 for definition). Note that the slowness indicated at the bottom of each plot is the slowness vector estimated from aligned seismograms. The peak value of Q reflects the goodness-of-fit of a single plane wavefront to the recorded wavefield. Numerical simulation experiments suggest that Q decreases rapidly with the introduction of extra systematic time errors. Slowness estimates that give a reasonable fit to the signal-eigenvector estimates of windows E5 and E6 could not be found and therefore there are no corresponding entries in Figure 7.6.

Relative phase delays of the detected signal were calculated from the estimated signal-eigenvector and plotted as star symbols in the upper diagrams of Figures 7.7 and 7.8. Solid lines in the same diagrams are the relative phase delays predicted by the slowness vector estimates given in Figures 7.5 and 7.6. The lower diagrams of Figures 7.7 and 7.8 are the corresponding time residuals (predicted - observed). The effective frequency ω_e (see

§3.3.2 for definition) that was used to translate the phase residual to the time residual is also given at the top of each diagram. The value of ω_e was calculated by shifting C-00 by 0.01 sec and the consequent change in the phase angle of the signal-eigenvector equals $2\pi\omega_e \times 0.01$. Note that the value of ω_e is roughly the mean frequency of the frequency band which contains most of the energy (see Figure 7.3).

All the time residuals relative to C-00 are less than 0.05 sec. The estimated time residuals at each station, together with their mean and standard error, were plotted in Figure 7.9. These time residuals are too large to be solely explained by the misalignment of the signal. It is of interest that time residuals are all positive at station 8 (M-05), negative at station 9 (M-06), and are mostly positive at station 3 (I-04). These time residuals are not correlated with the basin's thickness beneath each station. This agrees with the calculation in Chapter 6 that the difference in sediment thickness under each station is not large enough to become the dominant contributor of wavefront distortion. Further discussion on the time residuals is given in §7.2.

§ 7.1.2 P Windows

Because of the waveform incoherence and the proximity to the arrival of the S-wave, data after the first 2 sec of the vertical component were not used. Only three P-windows were selected for analysis. No pre-P window was available. Estimated eigenspectra of the first two windows (Figure 7.10) indicate that only one signal is present in each window. However, the relatively large value of $\hat{\lambda}_2$ in window 3 may indicate a secondary signal in this part of the seismogram. Nevertheless, all slowness vectors were estimated with one signal-eigenvector and the resulting time residual is reasonably small (Figure 7.12). The estimated polarizations (Table 7.1) are also small in the last two windows.

Contours of the reciprocal projection length Q are shown in Figure 7.11 and the relative phase and time residual of each window are given in Figure 7.12. The effective frequency ω_e on the vertical component is about three times that of each horizontal component, reflecting

the broader bandwidth of the main energy distribution (Figure 7.3). Time residuals of the vertical component (Figure 7.13) are not as scattered as in the case of the horizontal components (Figure 7.9).

§ 7.1.3 Summary of Estimated Slowness Vectors

All the estimated slowness vectors for the mainshock of July 30, 1986 (Event 43) are summarized in Figure 7.14. Note that only the second quadrant of the slowness plane was plotted. With the exceptions of windows E2 and V3, slowness vectors from all three components display a counterclockwise azimuthal rotation of the wave propagation direction in subsequent windows. Window E2 contains a strong and relatively long-period S-phase that is not clearly seen on the NS component. The estimated azimuth of this signal is -31.6° , which implies less SH contribution to the NS component. This azimuthal effect on the horizontally polarized shear wave may explain why the signature of this S-phase is weak on the NS component. Slowness vector estimates of the EW component are different from those of the NS component even for windows that cover roughly the same time period.

A regular pattern of time residuals appeared in windows N1, N2, E1, and E2 (Figures 7.7 and 7.8), in which their estimated wave azimuths were greater than -45° (Figure 7.14). Windows N3, E3, and E4 show a different residual pattern, as well as different wave azimuths, from the above four windows. Because both clock errors and shallow site effects produce fixed time errors that are not dependent on the azimuth to the seismic source, additional lateral heterogeneities in the deeper portion of the subsurface structure are required to account for the observed window-dependent (or rather, slowness-dependent) time residuals. Interpretation of the observed time residuals as the signature of lateral heterogeneities needs further work to remove clock errors and errors that arise from the shallow soil layers. Nevertheless, the observed time residuals provide some confidence on the robustness of the procedures of slowness estimation adopted here. This slowness-dependent residual also indicates that the seismogram alignment technique (Goldstein and

Archuleta, 1991a) would not properly correct for the non-planar wavefront of a signal whose slowness vector is not close to the aligned seismic phase.

§ 7.2 Precision of Slowness Vector Estimates

Covariance matrices of the slowness estimates are given in Table 7.2. These matrices were calculated by (5.17.b). The slowness estimate variance is smaller for windows whose eigenvalue separation (or $\hat{\beta}^2$) are large, as was expected (see §5.3.1). The standard error for the slowness estimate is of the order 10^{-3} sec/km, with the largest value of 5.0×10^{-3} sec/km in window N4. The off-diagonal elements of the covariance matrices are non-zero (Table 7.2) and the two components of the slowness vector estimate are correlated. Choosing a focusing frequency of 12.5 Hz in this study ensures a small estimation bias that can be neglected compared to the estimation variance.

§ 7.3 Estimation of the Source Parameters of the July 30, 1986 Taiwan Earthquake

The ‘source parameters’ estimated in this study were the source position and the corresponding rupture time. In the following sections, the velocity model, the fault plane orientation and location will be referred to as the ‘independent parameters’, because they are estimated from data independent of the strong motion array data. The three-dimensional crustal model described in §6.3 and the fault plane obtained in Chapter 3 were adopted to determine the source parameters from the estimated P- and S-wave slowness, separately. The values of these independent parameters are listed in Tables 7.3 and will be referred to as ‘Model A’ in the following. The systematic and random errors of the estimated source parameters introduced by the uncertainties of the independent parameters and the slowness measurement errors are discussed in §7.3.1 to §7.3.2.

There are three P-sources mapped from the P-windows on the vertical acceleration component, and ten S-sources from the S-windows on the North-South and East-West

components (see Figure 7.2). The results are plotted in Figure 7.15. The estimated source position from window N5 (not shown in Figure 7.15) was considerably deeper than the other source estimates. Based on the late arrival time of this signal, it is possible that this signal is a secondary phase and is not radiated directly from the fault. Therefore, the source estimate of N5 was not used in the following discussion. The numerical values associated with each mapped source point in Figure 7.15 are the corresponding rupture times relative to the time of rupture nucleation which was assumed to be at the source position of N3.

The values of the independent parameters in Model A (Table 7.3) were the best estimates obtained in this study. The crustal velocity in model A is well constrained above 150 meters by drilling data (Anderson and Tang, 1989) and below 5 km depth by a velocity model obtained from travel-time inversion (Yeh, 1987). The seismic velocity of the subsurface structure between these two depths was mainly based on the P-velocity value measured in a seismic refraction study (Wen and Yeh, 1984) (see Figure 4.1).

All the P and S rays from the faulted area of Event 43 enter the basin at a depth around 0.38 km. It follows that the wave velocities in this depth range are crucial to the accuracy of the source mapping. The P- and S- velocities in the basin at this depth are the only independent parameters that are not constrained by other seismological studies. The reason why a S-velocity of 1.5 km/sec ($0.48 + 3.4 \times (0.38 - 0.08)$) was chosen is because, with this value, the mapped source parameters are close to the focus (the origin in Figure 7.15) and the origin time inferred by the joint location in Chapter 3 (Table 3.1). Several different values of the S-velocities at the two sides of the basin-basement interface were tried for source mapping and it was found that the mapped source positions were more sensitive to the contrast of velocities across the basin-basement interface than to their absolute values. In general, a velocity ratio of 0.7 would give source positions close to the inferred focus. More discussion is given in §7.3.3. The P-velocity at this depth is determined from the S-velocity by adopting a reasonable Poisson ratio of 0.3.

The two spatial distributions of P- and S- source points in Figure 7.15 show a systematic discrepancy. The inferred P-sources are at the down-dip side of the inferred S-source positions. This systematic shift in source positions can be easily removed by a slightly different crustal model than the one specified in Table 7.3. However, it was not done here, because such fitting of crustal velocity structure is unimportant to the central objective of this study, i.e. comparing the resolution of the estimated source process parameters using P- and S- wave data independently.

There are several things that are important to bear in mind when interpreting the estimated parameters. First, the calculated source position is actually an estimate of the center of a fault patch (see Chapter 2), from points of which the radiated seismic waves at the array are indistinguishable at the resolution available with the SMART1 array. Secondly, Spudich and Frazer (1984) showed that large spatial variation in slip velocity and rupture speed (V_R) generates large amplitude high frequency ground accelerations. Thirdly, in each window, because only the strongest signal was detected, the actual ruptured area may be larger than the area indicated by the spatial extent of the source estimates. Fourthly, some parts of the fault may be a radiation node for the array and therefore were not detected by the SMART1 array. Finally, the slowness estimates, which are subject to random estimation error, are in reality not fully independent. This correlation leads to correlated source parameter estimates.

§7.3.1 Estimation Sensitivities and Uncertainties

The sensitivity of the source parameter estimation to the independent parameters and the slowness estimates can be summarized by their partial derivatives (Figure 7.16). Note that all the partial derivatives are strongly depth-dependent in the cases of both P- and S-sources. The absolute values of the partial derivatives increase as source depth increases. This result is consistent with a growing cross-sectional area of a ray tube as the rays travel deeper and away from the SMART1 array. This depth-dependence results in less accurate estimations of source parameters for deeper sources. A similar conclusion has been reached

by Iida *et al.* (1990a), who investigated the precision of source inversion using the method of waveform inversion.

Among the three source parameters for each source point, the down-dip distance has the largest partial derivative. This agrees with the well-known result in the traditional earthquake hypocenter location problem that the focal depth is ill-constrained when the azimuthal coverage of seismic stations is poor.

The large partial derivatives with respect to the slowness for P-source parameters, especially the down-dip distance, suggest that the estimated P-source parameters are more sensitive than the S-source parameters to small uncertainties in the estimated slowness. On the other hand, in terms of the forward problem, the larger partial derivatives for P-sources imply less variation in the measured P-wave slowness than in the S-wave slowness at the array, agreeing with the observed slowness vectors (see Figure 7.14). In addition, the smaller travel-time derivatives for P-sources suggest that the P-phases radiated from two neighboring fault patches would arrive closer in time at the array than the corresponding S-phases radiated from the same two patches. These properties entail that, to achieve the same level of source resolution, an array with better precision and higher resolution of multiple signals is required for the P-wave data.

The estimated P-source parameters are less sensitive to the uncertainties in the velocity structure, as suggested by their smaller partial derivatives with respect to the crustal velocity model (Figure 7.16). The result is that a more accurate source estimation would be achieved by P-wave data than by the S-wave data when both the P- and S- velocity models are subject to the same level of uncertainty.

The source-parameter estimation uncertainties come from both the random slowness measurement error and the uncertainty of the independent parameters. The former introduces random errors into the source parameter estimates and the latter produces systematic errors. Instead of performing error sensitivity analysis for all the independent parameters, equation (6.18) was used to calculate the overall uncertainties inherent in the slowness

measurement errors and in the uncertainties of the crustal velocity model and epicenter. Although the standard errors of the estimated fault strike, fault dip, and focal depth are reasonably small (Table 7.3), they are too large for equation (6.8) to be used, because the latter expansion is based on the first-order Taylor approximation. Therefore, they were not included in the calculation of variance for the mapped source parameters. The systematic errors introduced by the uncertainties associated with these three independent parameters to the estimated source parameters will be investigated later in §7.3.2.

The measurement errors of the slowness estimates were discussed in Chapter 5 and given in §7.2. The variances and covariances given in Table 7.3 represent the confidence in the values of the independent parameters in Model A. The fault plane and focus were estimated by the joint location procedure and the fault plane solution method described in Chapter 3. Their precisions (Table 3.1 and Figure 3.6) are typical of the uncertainties obtained in standard seismological hypocentral location and fault plane solution techniques. It is difficult to estimate the uncertainties associated with the velocity model, partly because it was constructed from studies (see §6.3) in which observational error and resolution were not discussed. Because no information is available to assess the velocity uncertainties, the variances 2.5×10^{-2} sec/km and 9.0×10^{-6} sec/km were assigned to the velocity at the reference depth and the velocity gradient, respectively, in blocks 2 and 3 (Table 7.3). This choice of variances was intended to represent the lower range of the uncertainties of a seismological study of the velocities in blocks 2 and 3. They were introduced so the relative importance of seismic velocity in the source mapping uncertainties can be evaluated. The variance and covariance for the velocity in the topmost two blocks (parameters A_4 , A_5 , B_4 , and B_5 ; see Table 7.3), were set equal to zero, because the corresponding partial derivatives (see Figure 7.16) are small and their contributions to the uncertainties of source parameter estimates are negligible. The parameters A_1 , B_1 , and their variances were estimated by the least-squares fitting of a gradient-velocity model to the mean velocities of the 3-D model (Yeh, 1987) at four different depths (see Figure 3.4).

The covariance matrices calculated by (6.8) are given in Table 7.4 and the estimation standard errors for each source point are plotted in Figure 7.17. The vertical and horizontal bars in Figure 7.17 represent one standard error of the estimated source position and the numbers shown are the corresponding rupture time with its standard error. The large correlation between the rupture time and the down-dip distance (Table 7.4) parallels the trade-off between origin time and focal depth in the earthquake location problem. As expected, the estimation variance of the down-dip distance is larger than the variance of the along-strike distance. For P- and S- source at approximately the same depth, for example V1 and N2, the calculated estimation variance using the P-wave data is smaller than that from the S-wave data (Figure 7.17). This is because more than half of the total estimation variance for source parameters inferred by S-wave data comes from the uncertainty of the rock velocity A_2 immediately below the basin. This percentage contribution is considerably larger than that of the P-wave data, which is less than 25%. The large variance contribution from A_2 is another expression of the importance of the velocity contrast between the basin and basement in determining the source parameters. It can be concluded that the source-parameter uncertainty is mainly controlled by the uncertainties of velocity contrast between basin and basement rock.

§7.3.2 Uncertainties Associated with Fault Strike, Dip, and Focal Depth

To investigate the amount of systematic errors in the estimated source parameters of each source point induced by the uncertainties in fault strike, fault dip, and focal depth, several mappings were made with values of these three parameters perturbed by one standard error (8.0° , 8.0° , and 3.0 km, respectively). The results (Figure 7.18) showed a systematic shift of the mapped source positions from the unperturbed positions in Figure 7.15. The shift in the source location of V1 is as large as 15 km in Model F of Figure 7.18. The distance between estimated source points also showed large variations. However, the relative location between source points and their order of rupturing remain unchanged.

§7.3.3 Uncertainties Associated with the Velocity Contrast and the Dipping Interface

To test the sensitivity of source estimates to the velocity contrast between basin and basement, the P-velocity gradient in block 3 was decreased from 4.367 to 1.667, and S-velocity gradient from 3.400 to 1.967 (see Figure 6.3). As a consequence, the velocity ratio between the alluvial basin and the basement was decreased from 0.7 to 0.6. The new mapped source positions are shown as Model H in Figure 7.19. This change of velocity contrast decreased the P-velocity at the basin interface by 0.81 km/sec and S-velocity by 0.3 km/sec, thus the P-source positions were more affected by this change of velocity ratio than were the S-source positions. Again, all the source positions were moved down-dip systematically but still retained their relative positions.

The dipping interface in Figure 6.3 was replaced by a horizontal interface at 0.38 km. The results, Model I in Figure 7.19, are consistent with the findings in §6.3, that is: removal of the basin interface, which acts as an optical lens that diverge rays leaving the basin, causes all the mapped source points to become shallower and cluster closer together than those in Model A.

§7.4 Estimation of the Source Dimension and Rupture Speed

The large variation in the estimated source positions and rupture times described in the previous two sections indicate that the systematic errors introduced by the uncertainties of the independent parameters are large and, without stronger constraints on these independent parameters, the chance of obtaining source parameter estimates close to the true source parameters is slim.

Because all the source points are estimated using the same independent parameters and the estimation bias introduced by the uncertainties of these independent parameters is systematic, the source-parameter estimation variances were recalculated with only the random slowness measurement errors included in the computation. The resulting source-

parameter standard errors are shown in Figure 7.20. The standard errors for the S-sources given in Figure 7.20 are more than a factor of two smaller than those errors given in Figure 7.17. This dramatic reduction in variance is because slowness measurement errors account for less than half of the variances of S-source parameters given in Table 7.4. As expected, the estimation variances of P-sources are considerably larger than the variances of the S-sources.

The estimated S-source rupture time increases progressively up-dip. A similar temporal and spatial trend is also observed in the P-sources, but this trend is less definite than the one in S-sources because the differences in the estimated rupture times are less than one standard error of the estimation. Based on the estimated S-source rupture times (Figure 7.20), the rupture direction of Event 43 had both along-strike and up-dip components. The preferred rupture direction is chosen to be parallel to the line joining the estimated source points of E2 and N3. Because of the array-rupture configuration the early arrivals on the vertical and horizontal components are not coming from the area that ruptured first. Instead they originate at the source positions closer to the SMART1 array, suggesting a supershear rupture speed.

§7.4.1 Source Dimension

The dimension of the ruptured area was estimated as the area occupied by the source positions shown in Figure 7.20. The spatial extent of the P-sources is $(7.5 \pm 4.7 \times 3.5 \pm 0.6)$ km², and of the S-sources is $(10.0 \pm 0.7 \times 6.5 \pm 0.1)$ km². For the perturbed models studied in §7.3.2 and §7.3.3, the spatial extent of P- and S- sources varied in some cases by a factor of 2 from the source dimension estimate of model A.

In detail, the source dimension is not strongly affected by the uncertainties in the fault strike. However, when the fault dip is increased by 8 degrees, the estimated source positions converge toward the focus (the origin of the fault coordinates) giving a smaller source dimension estimate than that from model A. The opposite occurs when fault dip was decreased by 8 degrees. The focal depth and velocity contrast also have significant

effects on the estimated source dimension. The source dimension corresponding to a focal depth of 12.7 km (model F in Figure 7.18) is only half of the dimension inferred from model A. With a velocity contrast of 0.6 (model H in Figure 7.19), the corresponding source dimension is more than twice the dimension of model A.

§7.4.2 Rupture Duration and Rupture Speed

The rupture duration was estimated by the largest difference in rupture-time estimates. The duration of model A was 0.3 ± 0.7 sec and 3.0 ± 0.2 sec for P- and S- sources, respectively (Figure 7.20). Because the difference in P-source rupture-time estimates is less than the standard errors, the estimated 0.3 sec P-source duration is below the resolution level.

The most straightforward approach is to compute the average rupture speed V_R of Event 43 from the ratio of source dimension and S-source rupture duration. The resulting average rupture speed along the diagonal of the ruptured area (see Figure 7.20), which is roughly along the rupture direction, is 3.94 ± 0.23 km/sec. This value compares with an S-wave velocity of 3.26 km/sec in the crust at a depth of 5 km (Table 7.3).

From the estimated rupture times (Figure 7.20), different rupture speeds at different stages of rupturing are indicated. Rupture speed between a pair of source points, i and j , was computed from their estimated source locations, \hat{s}_i and \hat{d}_i , and their estimated rupture times, $\hat{\tau}_i$, by

$$\hat{V}_R = \frac{\sqrt{(\hat{s}_i - \hat{s}_j)^2 + (\hat{d}_i - \hat{d}_j)^2}}{(\hat{\tau}_i - \hat{\tau}_j)}. \quad (7.1)$$

The standard errors of the estimated rupture speeds were calculated with a formula similar to equation (6.8). There are two obstacles to a reliable measurement of the rupture speed of the dislocation. First, the apparent rupture speed, instead of the true rupture speed, would be measured if i and j do not lie on a line that is parallel to the rupture direction (Goldstein, 1988). Second, the source parameter estimates are subject to estima-

tion errors and these errors propagate into the rupture speed estimate. (7.1) implies that the estimated rupture speed is sensitive to small errors in rupture time when the denominator is small, i.e. when the estimated rupture-time difference between i and j is small. Therefore, rupture speeds computed from the small P-source rupture time differences are not reliable and are not considered in the following. The first of the above obstacles was removed by selecting four estimated S-sources that lie approximately along the inferred rupture direction described previously. These four source points correspond to windows N2, N3, E1, and E2.

The estimated rate of rupture propagation using N3 and E1 was 5.58 ± 0.79 km/sec, and 6.99 ± 1.62 km/sec using N3 and N2 (Table 7.5). These two rupture speeds are supershear, i.e. exceed the average S-wave velocity in the crustal rock (see Figure 3.3.b). They are also unrealistically high compared to most rupture speeds estimated from earthquakes in other regions (a table of estimated rupture speeds for earthquakes occurred around the world is given in Kasahara, 1981). There are several possible explanations for these high rupture speed estimates. The first is that the assumed fault plane and crustal velocity model are inaccurate and the resulting systematic errors in the source-parameter estimates bias the calculated rupture speed; further discussion follows in this section. A second explanation is that the preferred rupture direction adopted here is incorrect and the estimated rupture speed is actually the apparent rupture speed. A third explanation is that there are some unknown lateral heterogeneities in the crust whose differential effects on the source-parameter estimate of the individual source point result in the unreasonably high rupture speed estimate. This possibility was demonstrated in §4.3. In addition, when the uncertainties of the velocity model are included in the variance calculation, the large standard errors of the estimated source parameters (see Figure 7.17) give little confidence to the estimated rupture speed. Nevertheless, supershear values for V_R have been derived during the early stage of earthquake faulting in the earlier studies, e.g. the 1979 Imperial valley earthquake (Olson and Apsel, 1982; Archuleta, 1984; Spudich and Cranswick, 1984). Theoretically, supershear rupture speed is possible for a Mode II case of fracture

(for example, see the review given in Scholz, 1990).

\hat{v}_R calculated from the source pairs (N2, E2) and (E1, E2) are 3.24 ± 0.12 km/sec and 3.07 ± 0.13 km/sec, respectively. These two values are lower than the local shear velocity (see Figure 3.3.b). If these rupture speeds are taken at face value, the inference is that the fault rupture of Event 43 spread out rapidly at the deeper part of the faulted area during the earlier stage of rupturing, and slowed down to a rupture speed below the shear velocity as the rupture moved farther up-dip.

To investigate the effects of systematic errors on the estimated rupture speed, the same calculation was applied to the source estimates given in §7.3.2 and §7.7.3 and the results are given in Table 7.5. The estimated rupture speeds for the early stage of rupture varied over a wide range, from 4.16 km/sec to 31.0 km/sec. As a consequence, the confidence in the rupture-speed estimates at the deeper part of the fault is low. The estimated rupture speeds of the shallower up-dip portion of the fault plane were more stable, ranging from 2.48 km/sec to 3.43 km/sec. The rupture speeds estimated from the source pairs that include N2 were always greater than those including E2, in agreement with the suggestion that N2 is located slightly off the inferred rupture direction.

Despite the unstable estimates of v_R for the earlier stage of rupture propagation and the limited number of models evaluated in this study, the inference of increasing rupture speed as rupture continued is not affected by the uncertainties of the fault plane and crustal velocity model. However, it is noted that, when the assumed fault dip is 52 degrees, the rupture-speed estimates (Model E in Table 7.5) appear to be more reasonable, suggesting that there may be one or more combinations of independent parameters, whose values are within the standard errors of those given in Table 7.3, which would give rupture-speed estimates more in agreement with those values estimated from other earthquakes.

Table 7.1 Estimate of the Polarization

β^2			
Window	NS	EW	Z
0	0.162	0.230	
1	0.465	0.768	0.669
2	0.704	0.700	0.445
3	0.578	0.476	0.406
4	0.420	0.462	
5	0.715	0.274	
6	0.733	0.408	

Table 7.2 Covariance Matrix of Slowness Estimates

Event 43 NS Component

Windows 1 and 2

$$\begin{bmatrix} 0.797 \times 10^{-5} & 0.733 \times 10^{-5} \\ 0.733 \times 10^{-5} & 0.140 \times 10^{-4} \end{bmatrix}, \begin{bmatrix} 0.286 \times 10^{-5} & 0.251 \times 10^{-5} \\ 0.251 \times 10^{-5} & 0.326 \times 10^{-5} \end{bmatrix}$$

Windows 3 and 4

$$\begin{bmatrix} 0.895 \times 10^{-6} & 0.224 \times 10^{-5} \\ 0.224 \times 10^{-5} & 0.134 \times 10^{-4} \end{bmatrix}, \begin{bmatrix} 0.611 \times 10^{-5} & -.101 \times 10^{-4} \\ -.101 \times 10^{-4} & 0.248 \times 10^{-4} \end{bmatrix}$$

Windows 5 and 6

$$\begin{bmatrix} 0.273 \times 10^{-5} & -.713 \times 10^{-6} \\ -.713 \times 10^{-6} & 0.137 \times 10^{-5} \end{bmatrix}, \begin{bmatrix} 0.125 \times 10^{-5} & 0.300 \times 10^{-6} \\ 0.300 \times 10^{-6} & 0.193 \times 10^{-5} \end{bmatrix}$$

Event 43 EW Component

Windows 1 and 2

$$\begin{bmatrix} 0.201 \times 10^{-5} & 0.964 \times 10^{-6} \\ 0.964 \times 10^{-6} & 0.113 \times 10^{-5} \end{bmatrix}, \begin{bmatrix} 0.142 \times 10^{-5} & -.347 \times 10^{-6} \\ -.347 \times 10^{-6} & 0.150 \times 10^{-5} \end{bmatrix}$$

Windows 3 and 4

$$\begin{bmatrix} 0.101 \times 10^{-4} & 0.327 \times 10^{-5} \\ 0.327 \times 10^{-5} & 0.460 \times 10^{-5} \end{bmatrix}, \begin{bmatrix} 0.939 \times 10^{-5} & 0.372 \times 10^{-6} \\ 0.372 \times 10^{-6} & 0.136 \times 10^{-4} \end{bmatrix}$$

Table 7.2 (Continued)

Event 43 Z Component

Window 1

$$\begin{bmatrix} 0.210 \times 10^{-5} & -.106 \times 10^{-5} \\ -.106 \times 10^{-5} & 0.458 \times 10^{-5} \end{bmatrix}$$

Window 2

$$\begin{bmatrix} 0.124 \times 10^{-4} & 0.336 \times 10^{-5} \\ 0.336 \times 10^{-5} & 0.680 \times 10^{-4} \end{bmatrix}$$

Window 3

$$\begin{bmatrix} 0.245 \times 10^{-4} & -.102 \times 10^{-4} \\ -.102 \times 10^{-4} & 0.193 \times 10^{-4} \end{bmatrix}$$

Table 7.3 Model A

Block i	Velocity Model					
	Reference Depth (Km)	P Velocity at Reference Depth A_i^P (Km/sec)	P Velocity Gradient B_i^P (1/sec)	S Velocity at Reference Depth A_i^S (Km/sec)	S Velocity Gradient B_i^S (1/sec)	
1	5.000	5.723 ± 0.195	0.042 ± 0.012	3.255 ± 0.057	0.024 ± 0.003	
2	0.380	3.300 ± 0.05	0.524 ± 0.003	1.900 ± 0.05	0.293 ± 0.003	
3	0.080	1.500 ± 0.05	4.367 ± 0.003	0.480 ± 0.05	3.400 ± 0.003	
4	0.013	1.330	2.090	0.220	1.495	
5	0.000	0.470	69.23	0.120	5.385	

$$Cov\{A_1^P, B_1^P\} = -2.20 \times 10^{-1}$$

$$Cov\{A_1^S, B_1^S\} = -1.70 \times 10^{-4}$$

$$\text{Fault Strike } (\lambda) = 65^\circ \pm 8.0^\circ$$

$$\text{Fault Dip } (\delta) = 60^\circ \pm 8.0^\circ$$

$$\text{Epicenter} = (24^\circ 36.73' \text{ N} \pm 0.5 \text{ km}, 121^\circ 48.88' \text{ E} \pm 0.4 \text{ km})$$

$$\text{Focal Depth} = 9.7 \pm 3.0 \text{ km}$$

Table 7.4 Covariance Matrix of Source Parameter Estimates

Event 43 NS Component

Windows 1 and 2

$$\begin{bmatrix} 0.5169E+00 & 0.3096E+00 & 0.1676E+01 \\ 0.3096E+00 & 0.3973E+00 & 0.1052E+01 \\ 0.1676E+01 & 0.1052E+01 & 0.5551E+01 \end{bmatrix} \begin{bmatrix} 0.1226E+01 & 0.1387E+01 & 0.3932E+01 \\ 0.1387E+01 & 0.1806E+01 & 0.4483E+01 \\ 0.3932E+01 & 0.4483E+01 & 0.1272E+02 \end{bmatrix}$$

Windows 3 and 4

$$\begin{bmatrix} 0.4741E+01 & 0.8134E+01 & 0.1402E+02 \\ 0.8134E+01 & 0.1436E+02 & 0.2403E+02 \\ 0.1402E+02 & 0.2403E+02 & 0.4170E+02 \end{bmatrix} \begin{bmatrix} 0.1387E+01 & 0.2782E+01 & 0.3482E+01 \\ 0.2782E+01 & 0.5919E+01 & 0.7040E+01 \\ 0.3482E+01 & 0.7040E+01 & 0.8895E+01 \end{bmatrix}$$

Windows 5 and 6

$$\begin{bmatrix} 0.1149E+03 & 0.2203E+03 & 0.4108E+03 \\ 0.2203E+03 & 0.4284E+03 & 0.7852E+03 \\ 0.4108E+03 & 0.7852E+03 & 0.1470E+04 \end{bmatrix} \begin{bmatrix} 0.1108E+01 & 0.2059E+01 & 0.2838E+01 \\ 0.2059E+01 & 0.4116E+01 & 0.5375E+01 \\ 0.2838E+01 & 0.5375E+01 & 0.7403E+01 \end{bmatrix}$$
Event 43 EW Component

Windows 1 and 2

$$\begin{bmatrix} 0.7530E+00 & 0.1018E+01 & 0.2276E+01 \\ 0.1018E+01 & 0.1597E+01 & 0.3143E+01 \\ 0.2276E+01 & 0.3143E+01 & 0.6995E+01 \end{bmatrix} \begin{bmatrix} 0.2852E+00 & 0.1856E+00 & 0.7380E+00 \\ 0.1856E+00 & 0.4401E+00 & 0.4758E+00 \\ 0.7380E+00 & 0.4758E+00 & 0.2015E+01 \end{bmatrix}$$

Windows 3 and 4

$$\begin{bmatrix} 0.5164E+00 & 0.8334E+00 & 0.1344E+01 \\ 0.8334E+00 & 0.1645E+01 & 0.2235E+01 \\ 0.1344E+01 & 0.2235E+01 & 0.3605E+01 \end{bmatrix} \begin{bmatrix} 0.7647E+00 & 0.1290E+01 & 0.2079E+01 \\ 0.1290E+01 & 0.2469E+01 & 0.3576E+01 \\ 0.2079E+01 & 0.3576E+01 & 0.5773E+01 \end{bmatrix}$$

Table 7.4 Covariance matrices of the source parameters. First row: rupture times (sec); second row: along strike distance (km); third row: down-dip distance (km).

Table 7.4 (Continued)

Event 43 Z Component

Windows 1

$$\begin{bmatrix} 0.1934E+00 & -0.5651E-01 & 0.1081E+01 \\ -0.5651E-01 & 0.2167E+00 & -0.3071E+00 \\ 0.1081E+01 & -0.3071E+00 & 0.6132E+01 \end{bmatrix}$$

Windows 2

$$\begin{bmatrix} 0.3620E+00 & 0.2775E+00 & 0.2059E+01 \\ 0.2775E+00 & 0.4728E+00 & 0.1623E+01 \\ 0.2059E+01 & 0.1623E+01 & 0.1186E+02 \end{bmatrix}$$

Windows 3

$$\begin{bmatrix} 0.1090E+01 & 0.8657E+00 & 0.6665E+01 \\ 0.8657E+00 & 0.1122E+01 & 0.5305E+01 \\ 0.6665E+01 & 0.5305E+01 & 0.4099E+02 \end{bmatrix}$$

Table 7.5

Estimated Rupture Velocities (km/sec)				
Model	N3→E1	N3→N2	E1→E2	N2→E2
A	5.58	6.99	3.07	3.24
B	4.54	4.79	3.09	3.25
C	8.21	31.0	3.06	3.25
D	8.79	12.5	3.18	3.36
E	4.16	4.63	3.01	3.21
F	8.49	10.6	2.48	2.77
G	5.27	6.76	3.31	3.43
H	4.48	5.47	3.29	3.42
I	7.83	10.3	2.95	3.18

Table 7.5 Estimated rupture velocities. Model A is the model described in Table 7.3. See Figures 7.18 and 7.19 for descriptions of other models.

SMART 1 SUBARRAY CONFIGURATION

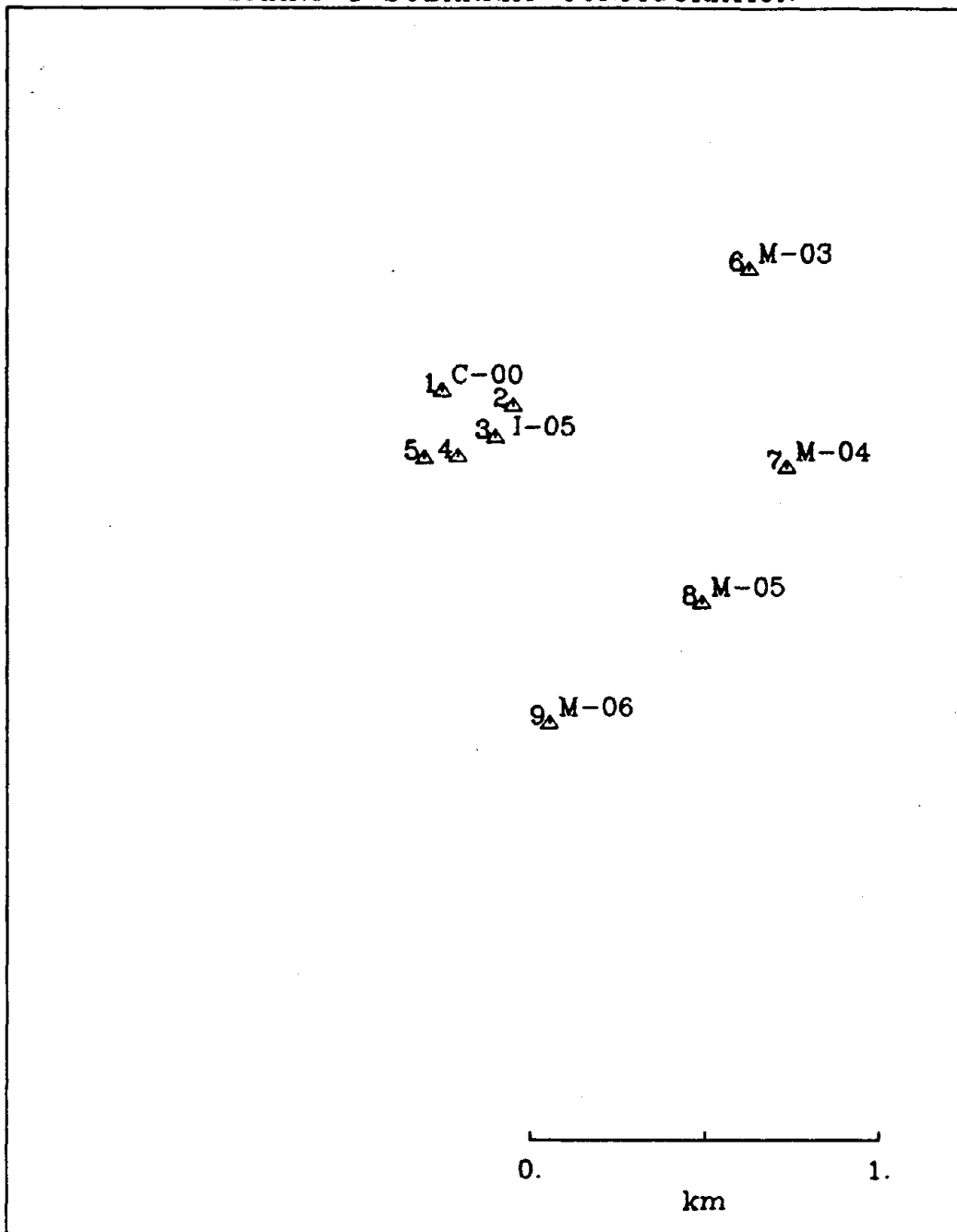


Figure 7.1 The SMART1 subarray used in slowness estimation. The numbers shown are the station indices.

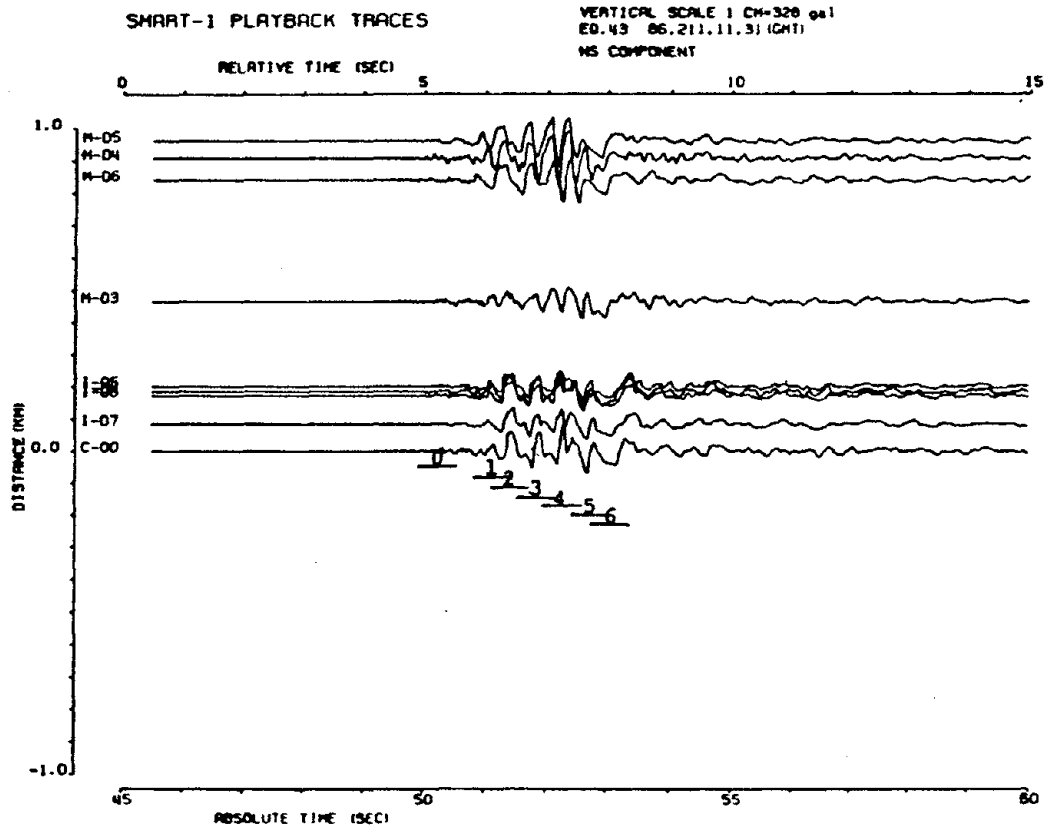


Figure 7.2 (a) North-South accelerations recorded at the subarray stations. Time windows selected for slowness estimation are plotted below station C-00. The distance shown in this figure is the projected distance along the reference slowness vector.

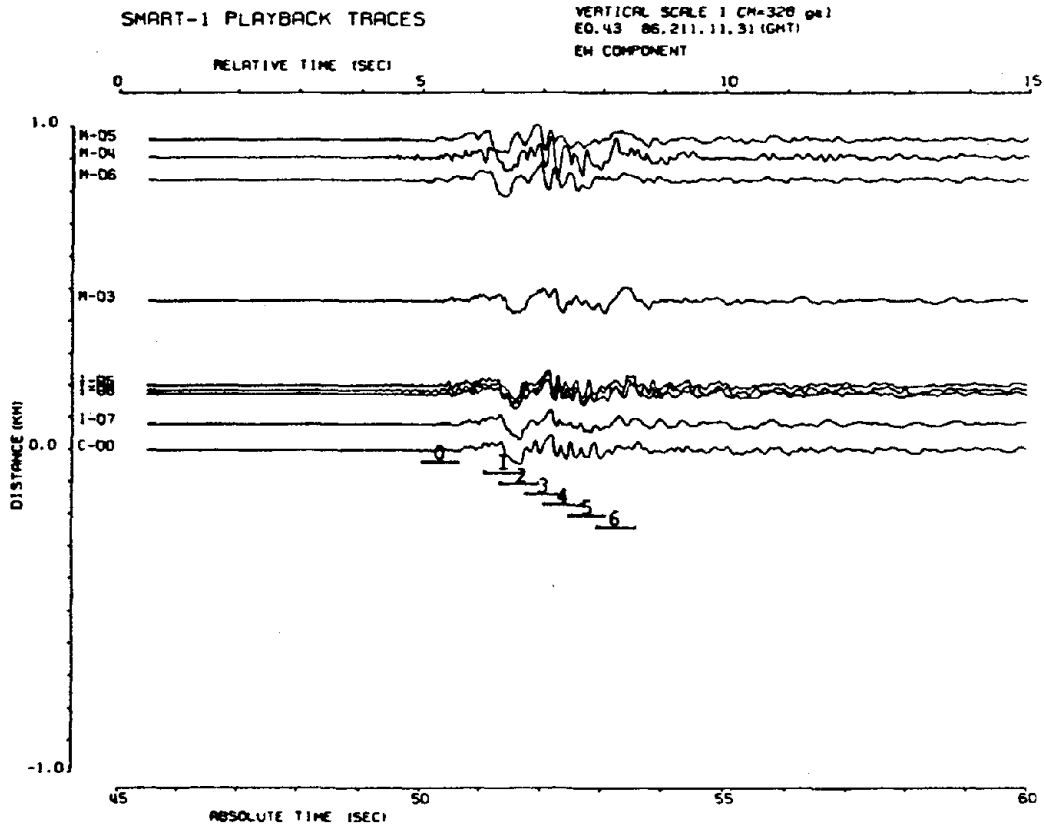


Figure 7.2 (b) East-West accelerations recorded at the subarray stations. See Figure 7.2.a for explanations.

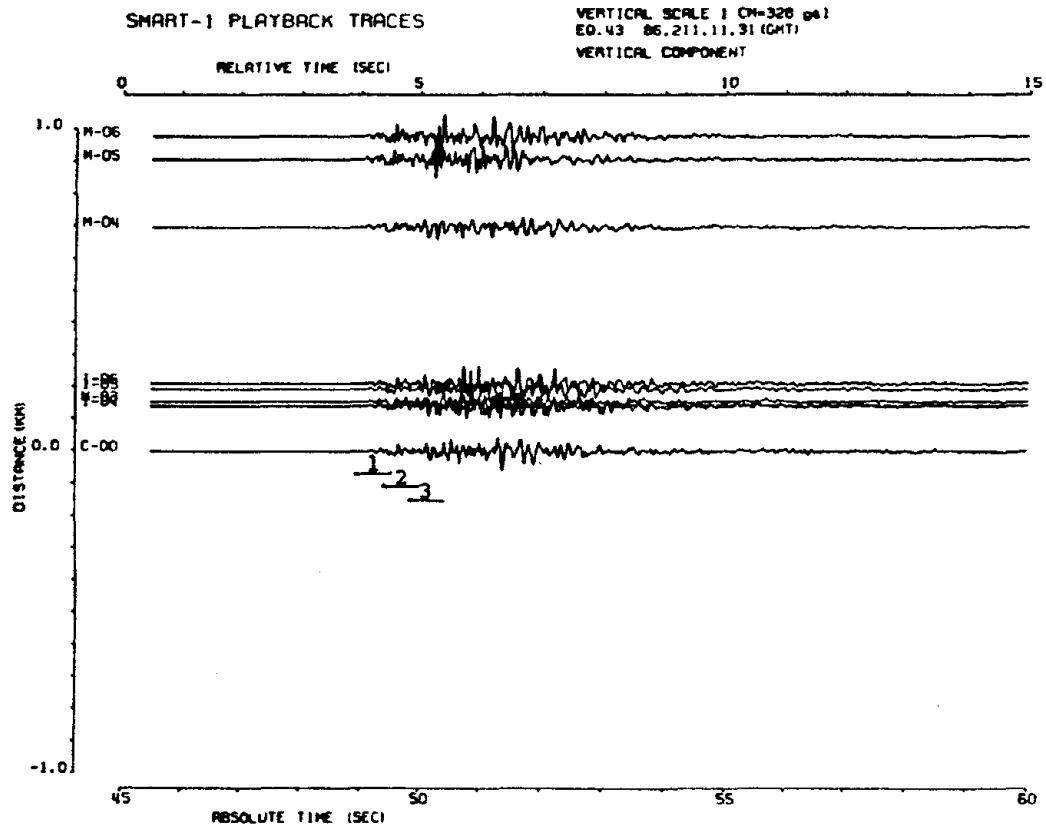


Figure 7.2 (c) Vertical accelerations recorded at the subarray stations. See Figure 7.2.a for explanations.

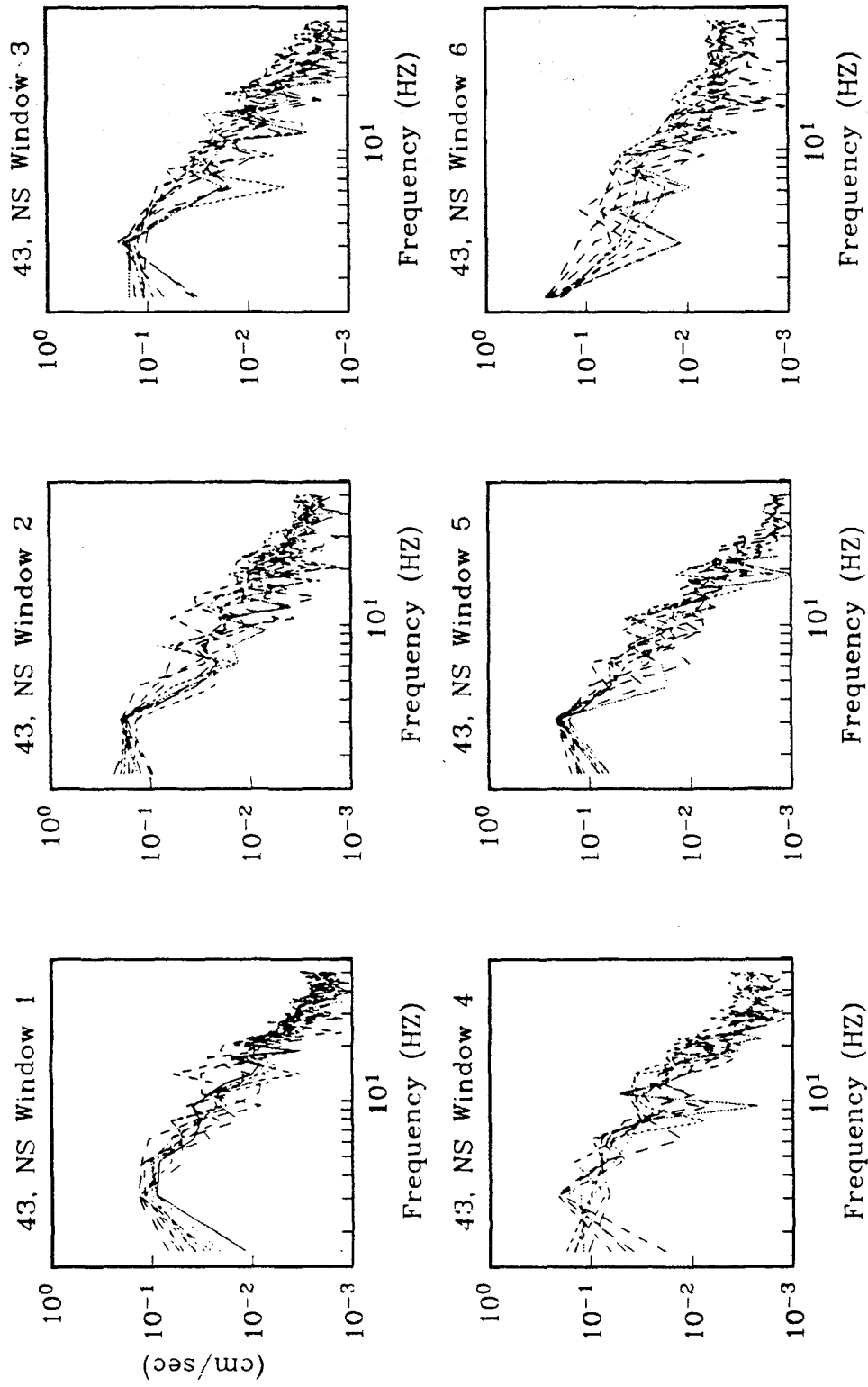


Figure 7.3 Fourier amplitude spectra of waves in the selected time windows.

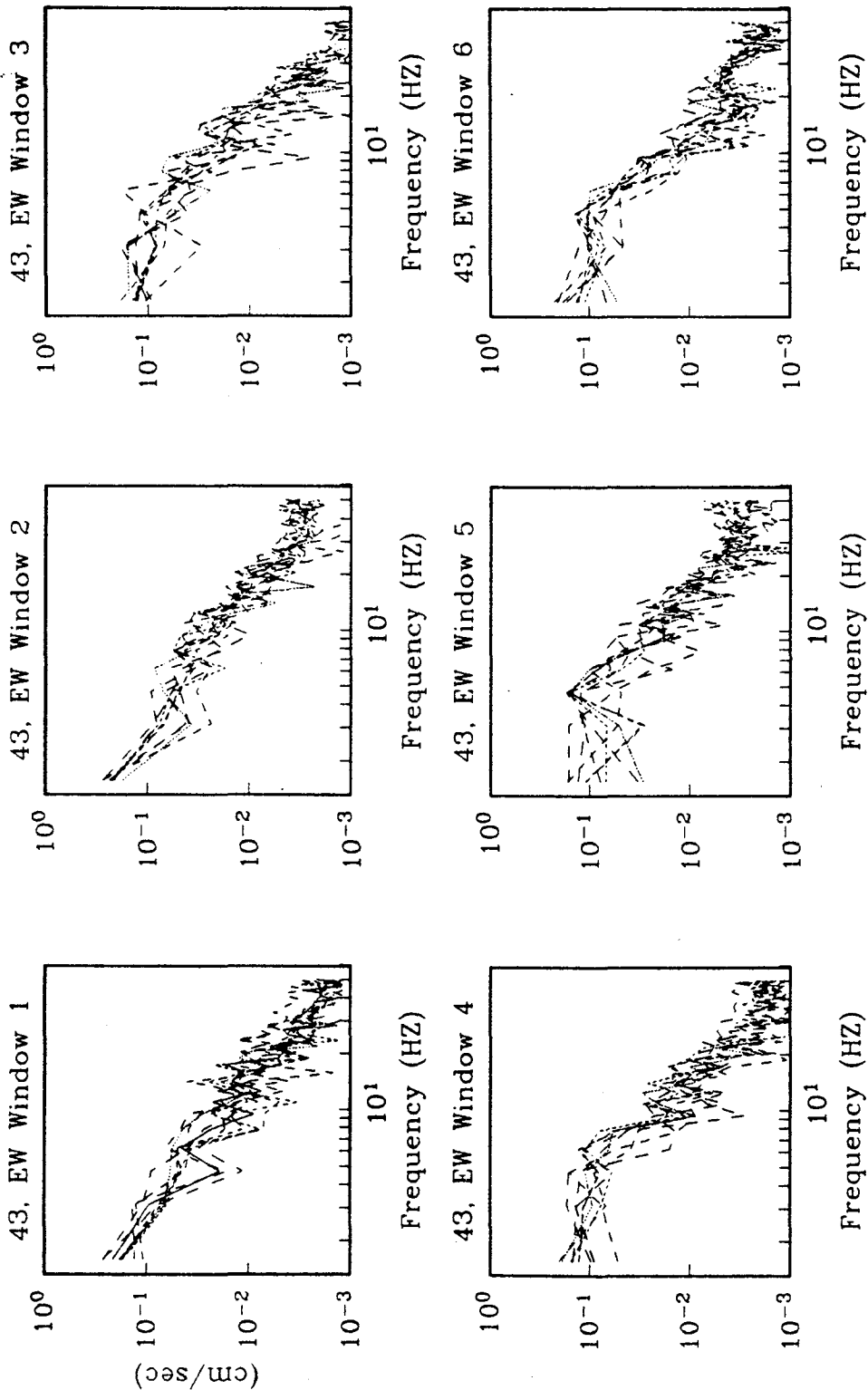


Figure 7.3 (Continued)

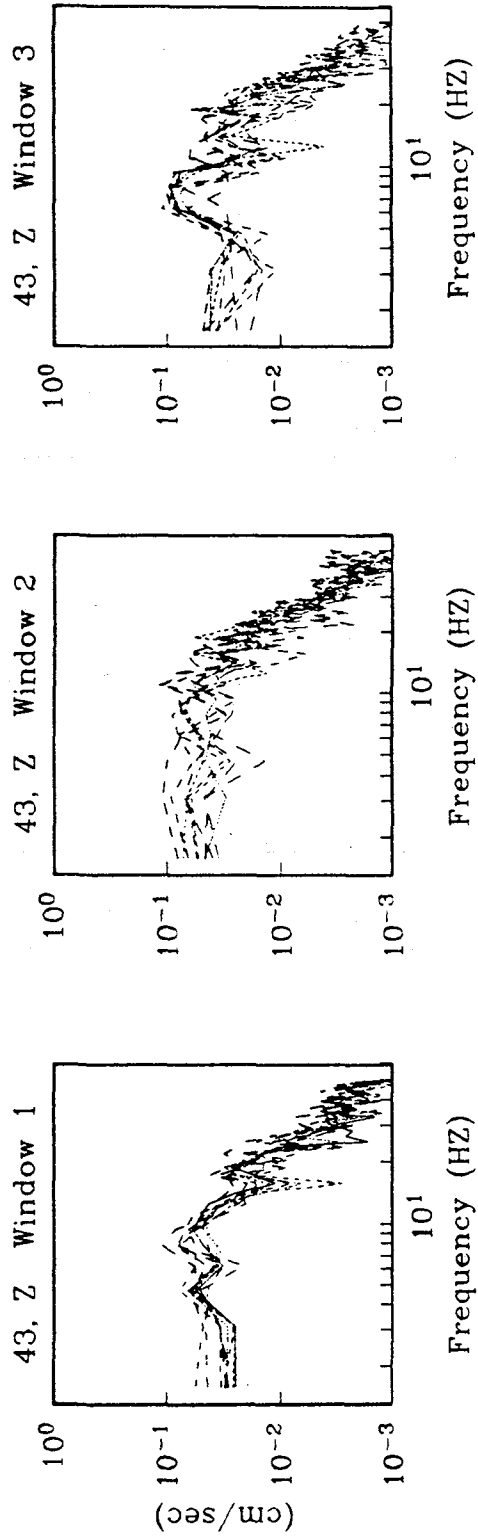


Figure 7.3 (Continued)

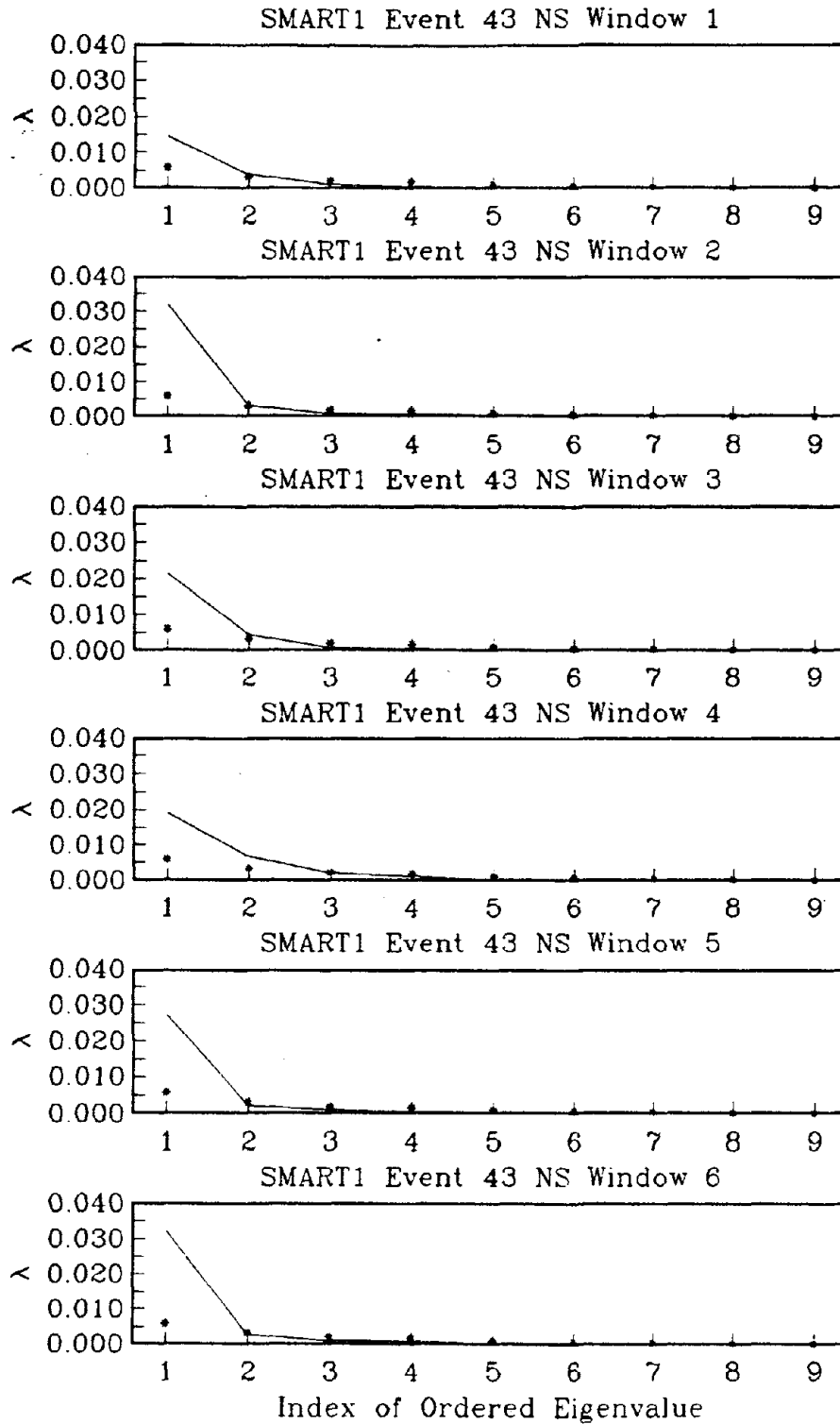


Figure 7.4 Estimated eigenspectra for windows on the EW and NS components. Symbols in each diagram are the estimated eigenspectra of window zero.

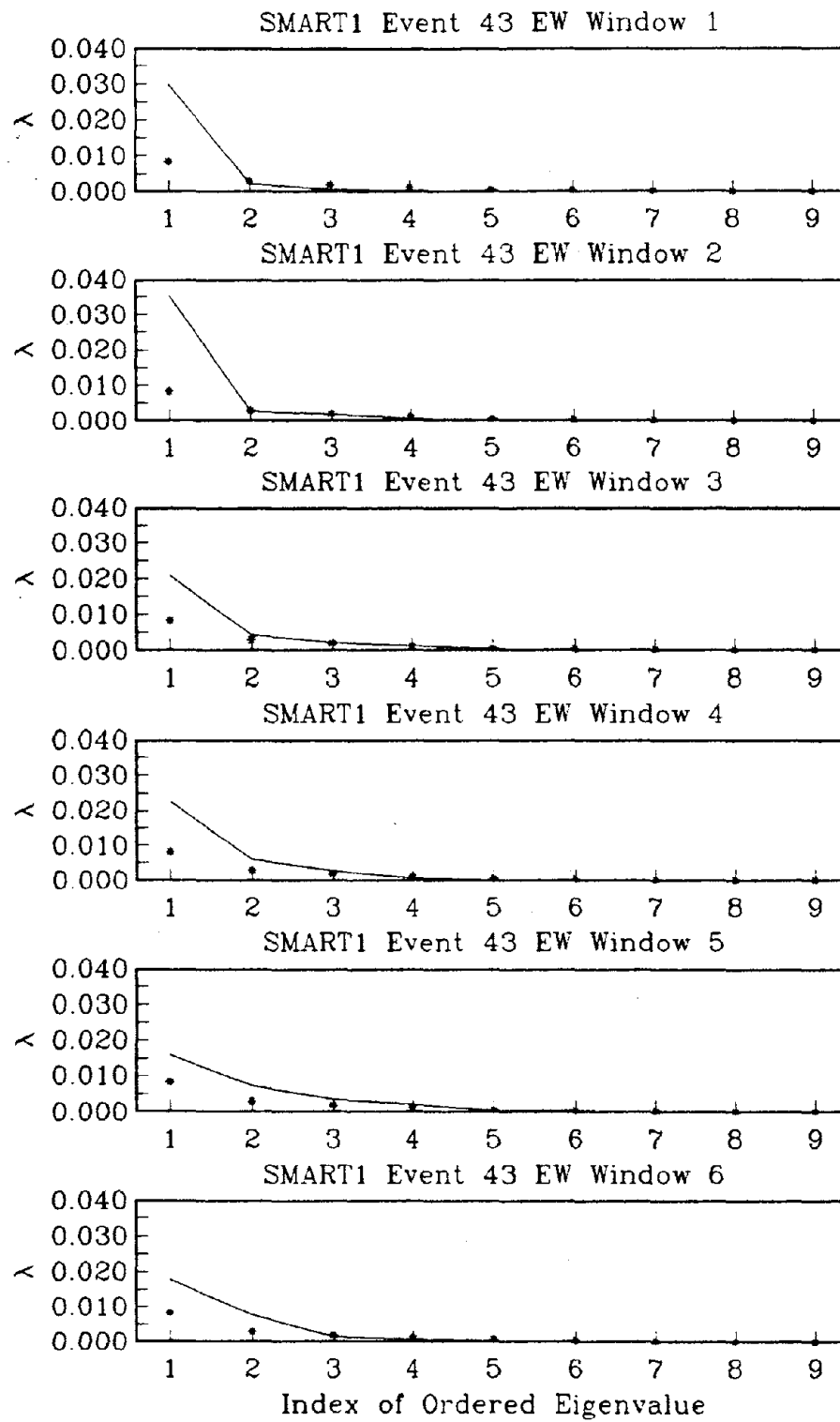
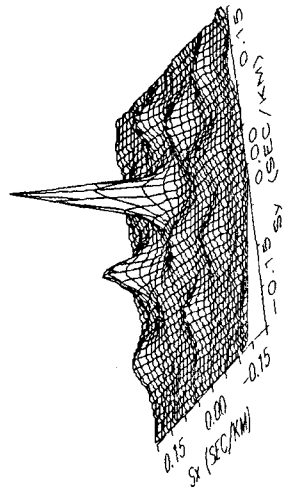
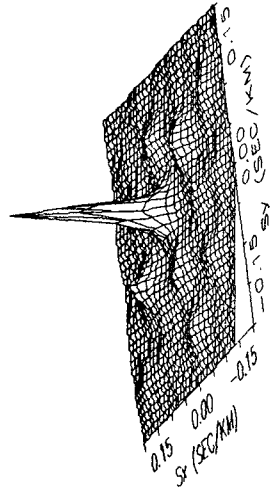


Figure 7.4 (Continued)

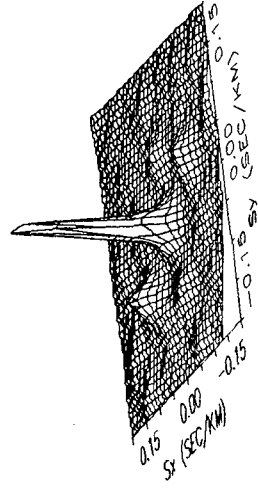
SMART1 Event 43 NS Window 1 SMART1 Event 43 NS Window 2 SMART1 Event 43 NS Window 3



Peak=9.0, S=(0.063,0.058)

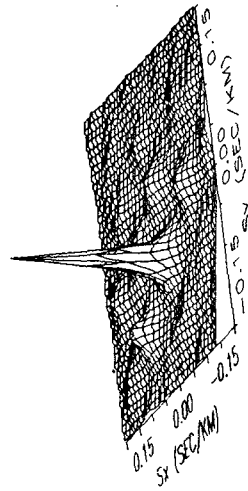


Peak=15.2, S=(0.028,0.023)

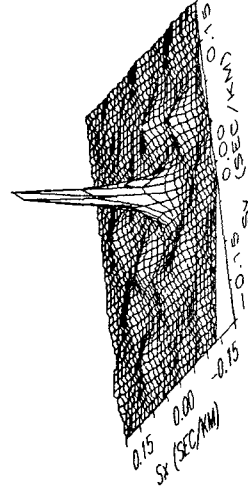


Peak=24.4, S=(-0.014,-0.015)

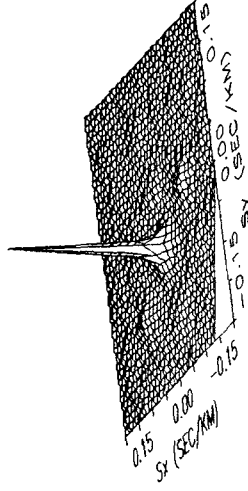
SMART1 Event 43 NS Window 4 SMART1 Event 43 NS Window 5 SMART1 Event 43 NS Window 6



Peak=14.3, S=(-0.020,-0.052)



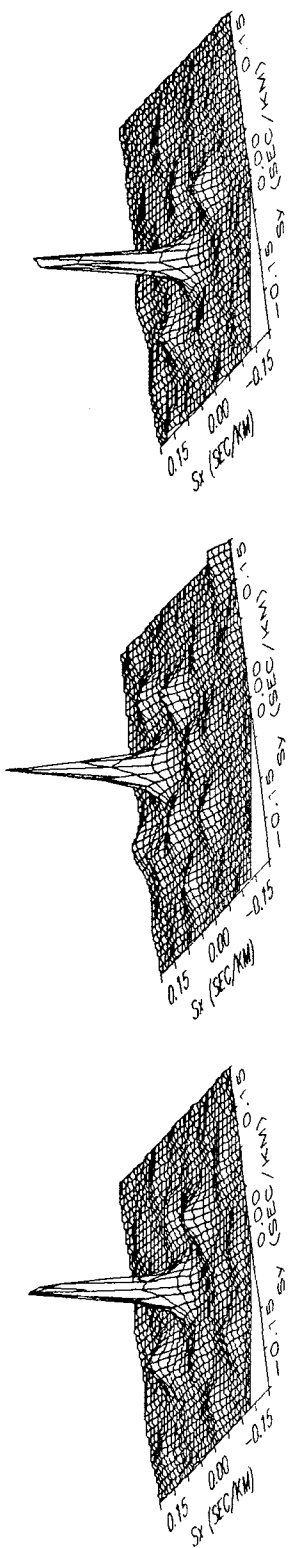
Peak=16.4, S=(-0.040,0.015)



Peak=51.1, S=(-0.008,-0.040)

Figure 7.5 The reciprocal projection length Q for NS component windows. The slowness vectors given at the bottom of each diagram are the slowness vectors estimated from the aligned wavefield.

SMART1 Event 43 EW Window 1 SMART1 Event 43 EW Window 2 SMART1 Event 43 EW Window 3

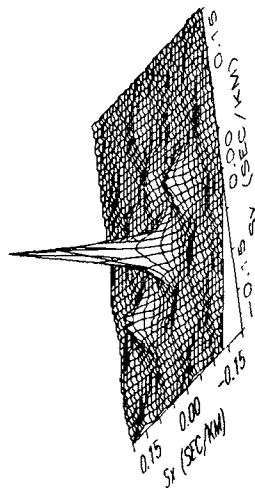


Peak=18.9, S=(0.025,0.004)

Peak=13.4; S=(0.103,0.021)

Peak=22.3, S=(0.017,-0.035)

SMART1 Event 43 EW Window 4



Peak=13.48, S=(0.007,-0.029)

Figure 7.6 The reciprocal projection length Q for EW component windows. See Figure 7.5 for explanation.

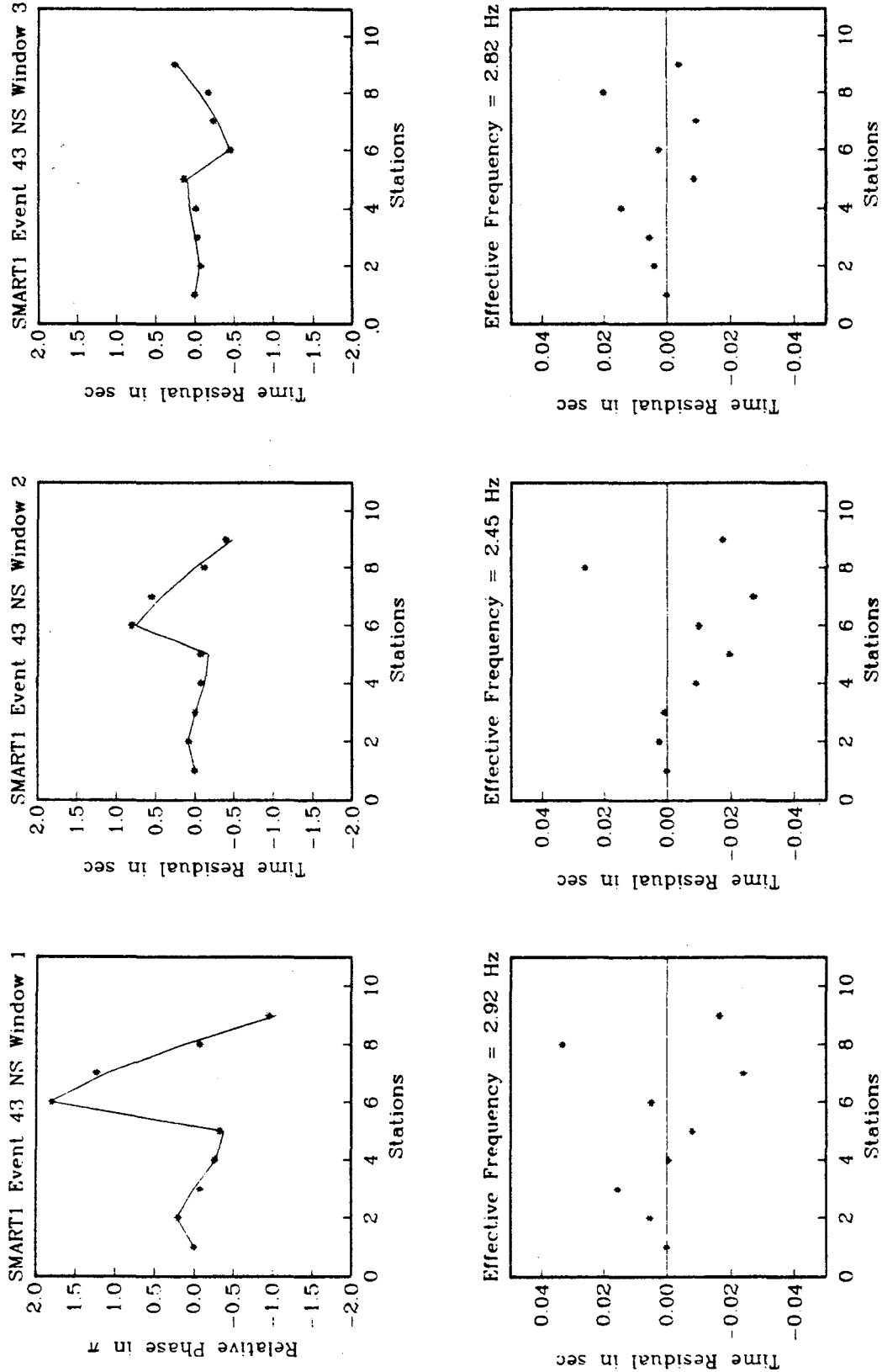


Figure 7.7 Top: Observed (stars) and predicted (solid lines) phase residuals of NS component windows. Bottom: Time residuals. Effective frequency is given at the top of each diagram. See Figure 7.1 for station index.

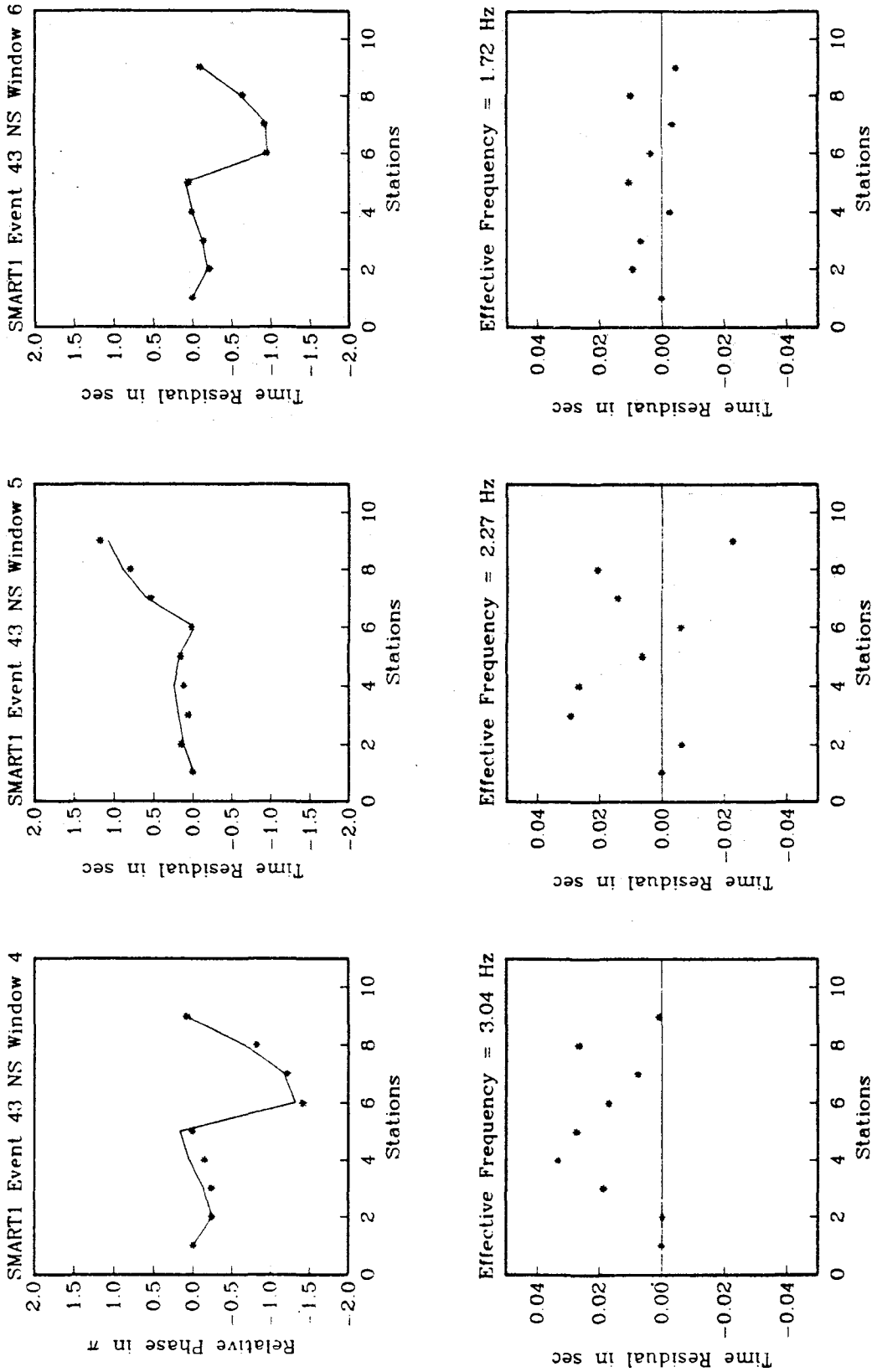


Figure 7.7 (Continued)

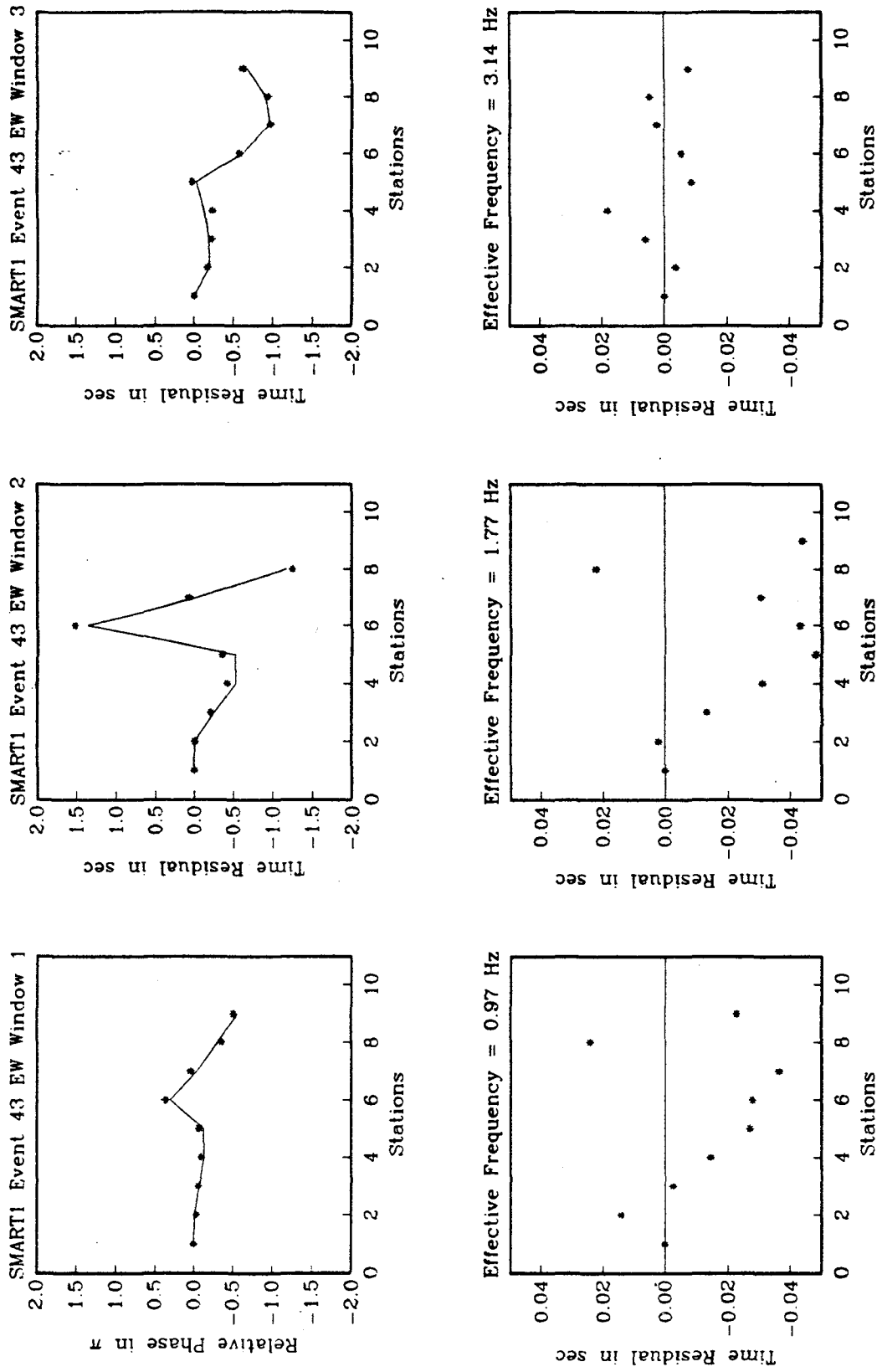


Figure 7.8 Same as Figure 7.7, but for EW component.

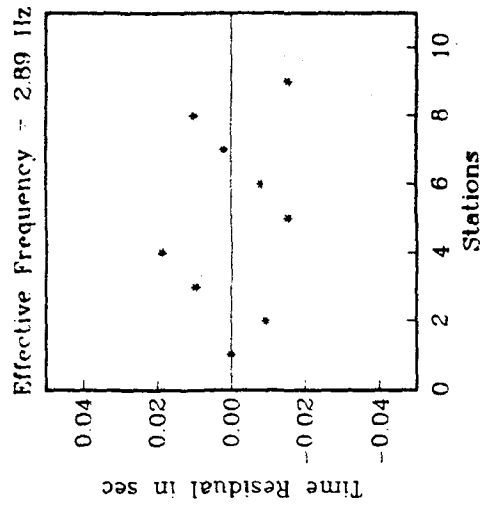
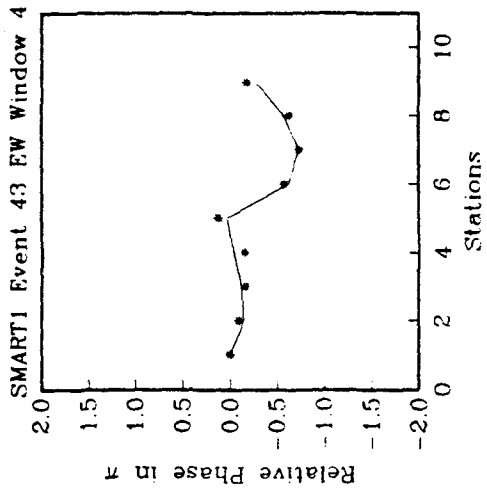


Figure 7.6 (Continued)

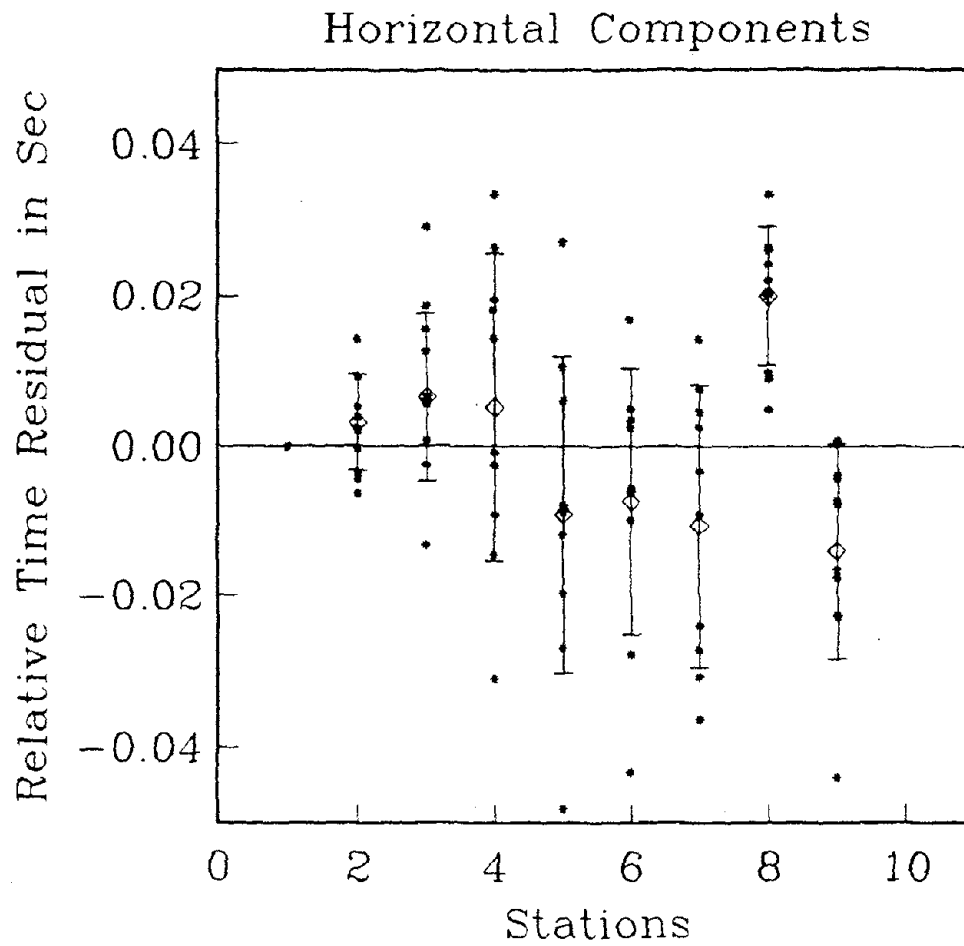


Figure 7.9 Summary of time residuals from both NS and EW components. The diamonds indicate the mean residual at each station. The vertical bars denote one standard deviation.

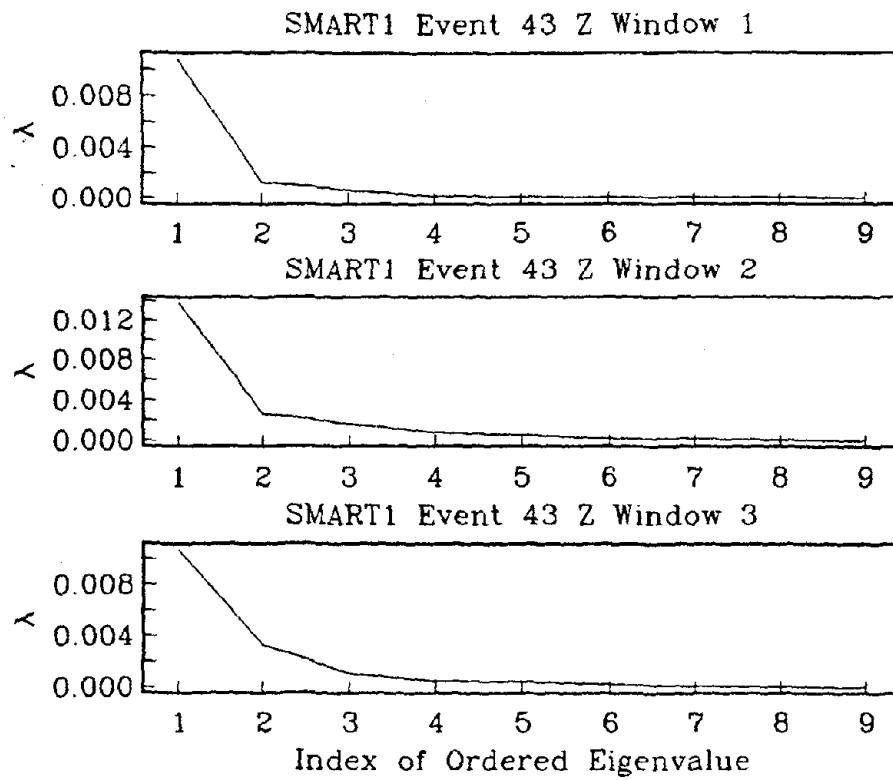
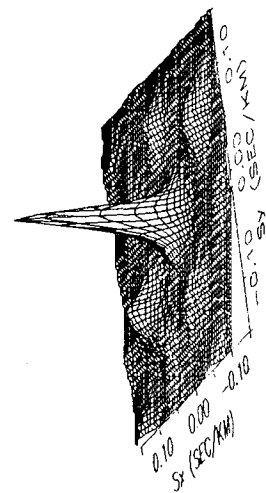
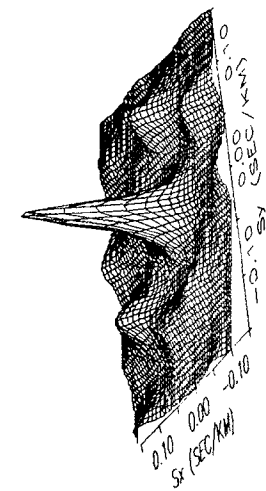
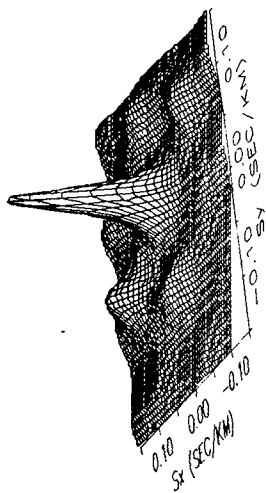


Figure 7.10 Estimated eigenspectra for vertical components.

SMART1 Event 43 Z Window 1

SMART1 Event 43 Z Window 2

SMART1 Event 43 Z Window 3



Peak=8.2, S=(0.017,0.034)

Peak=7.1, S=(-0.011,0.008)

Peak=12.6, S=(-0.001,0.011)

Figure 7.11 The reciprocal projection length Q for vertical component windows. See Figure 7.5 for explanations.

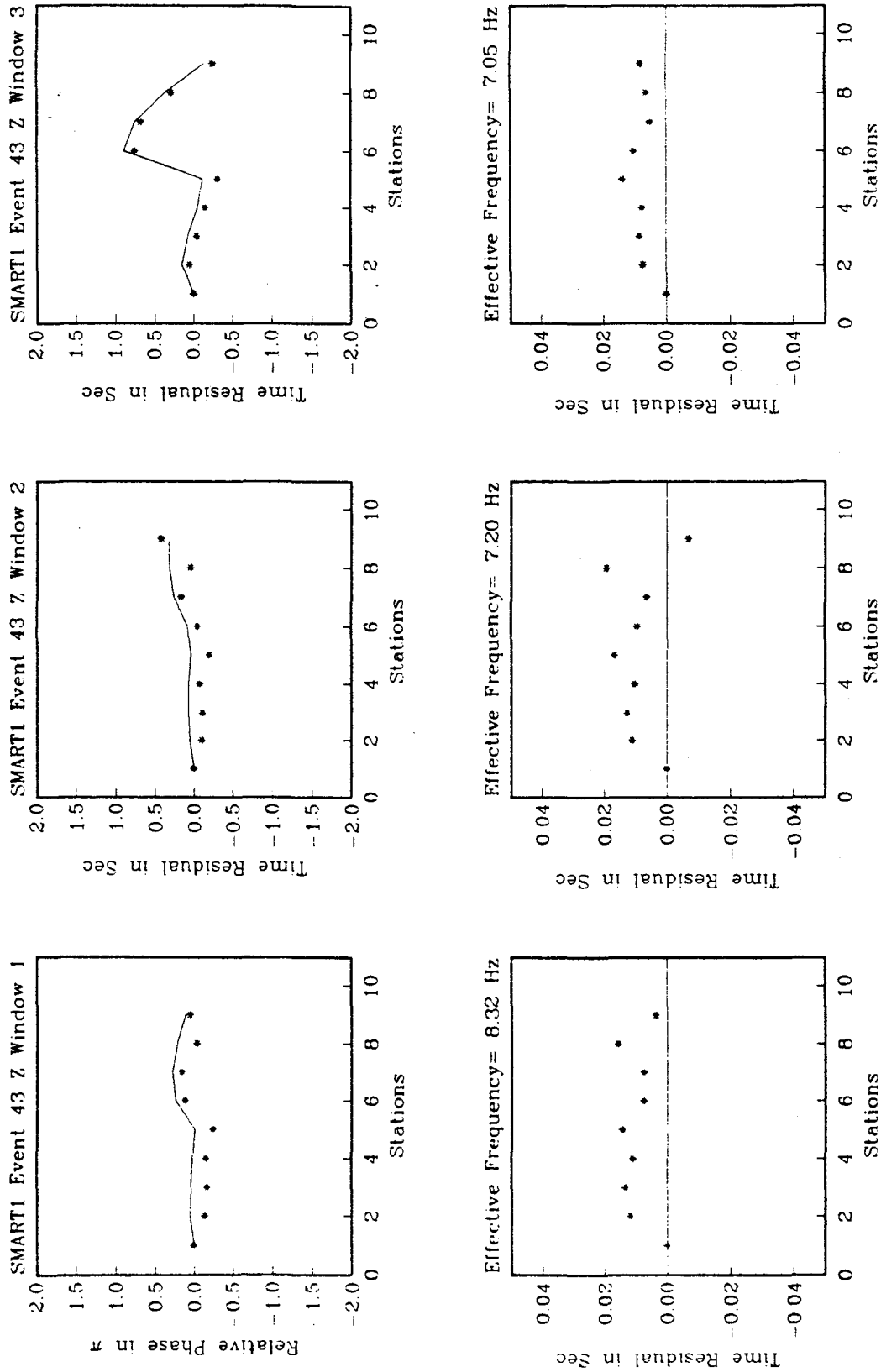


Figure 7.12 Same as Figure 7.7, but for vertical component.

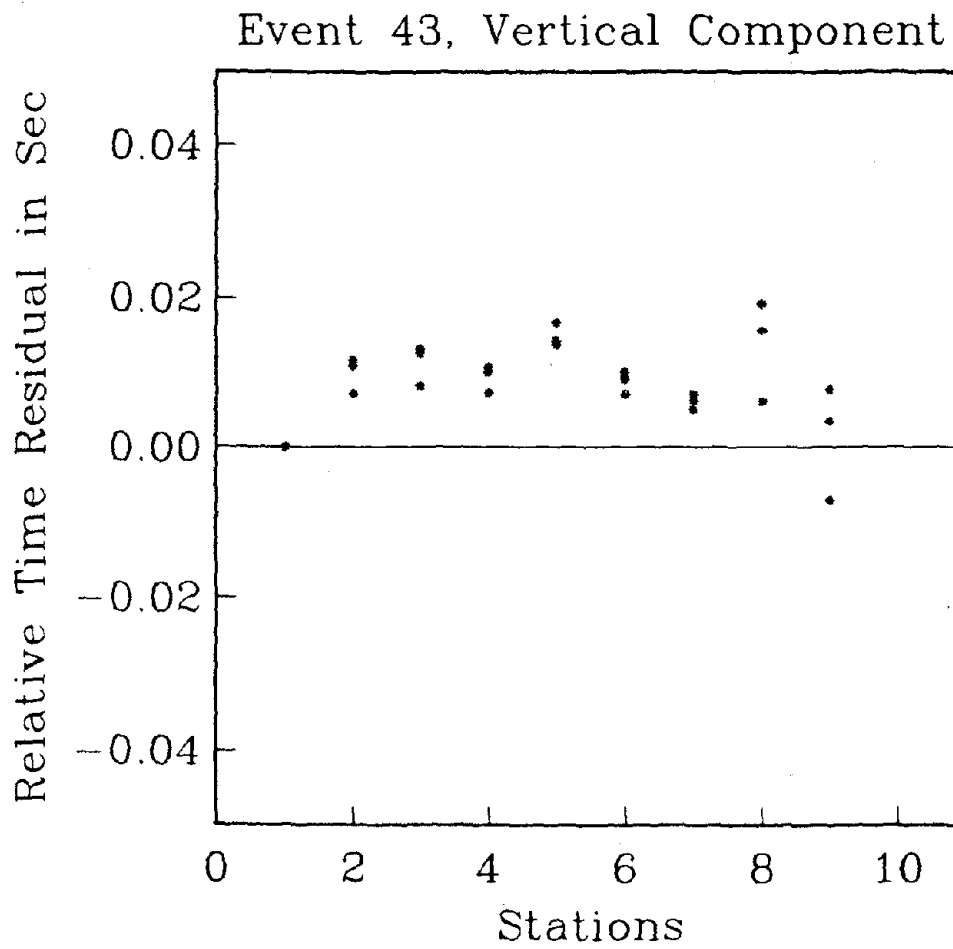


Figure 7.13 Summary of time residuals from the three windows of vertical component.

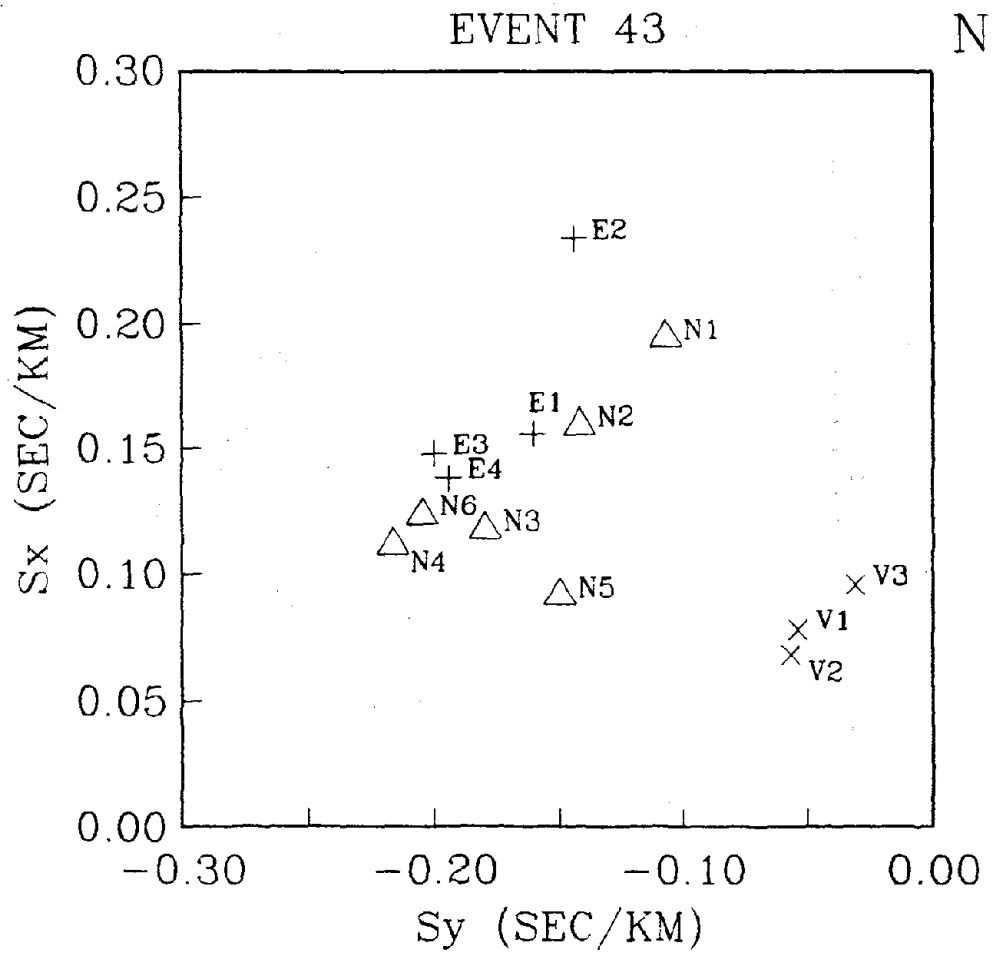


Figure 7.14 Summary of estimated slowness vectors from all three components.

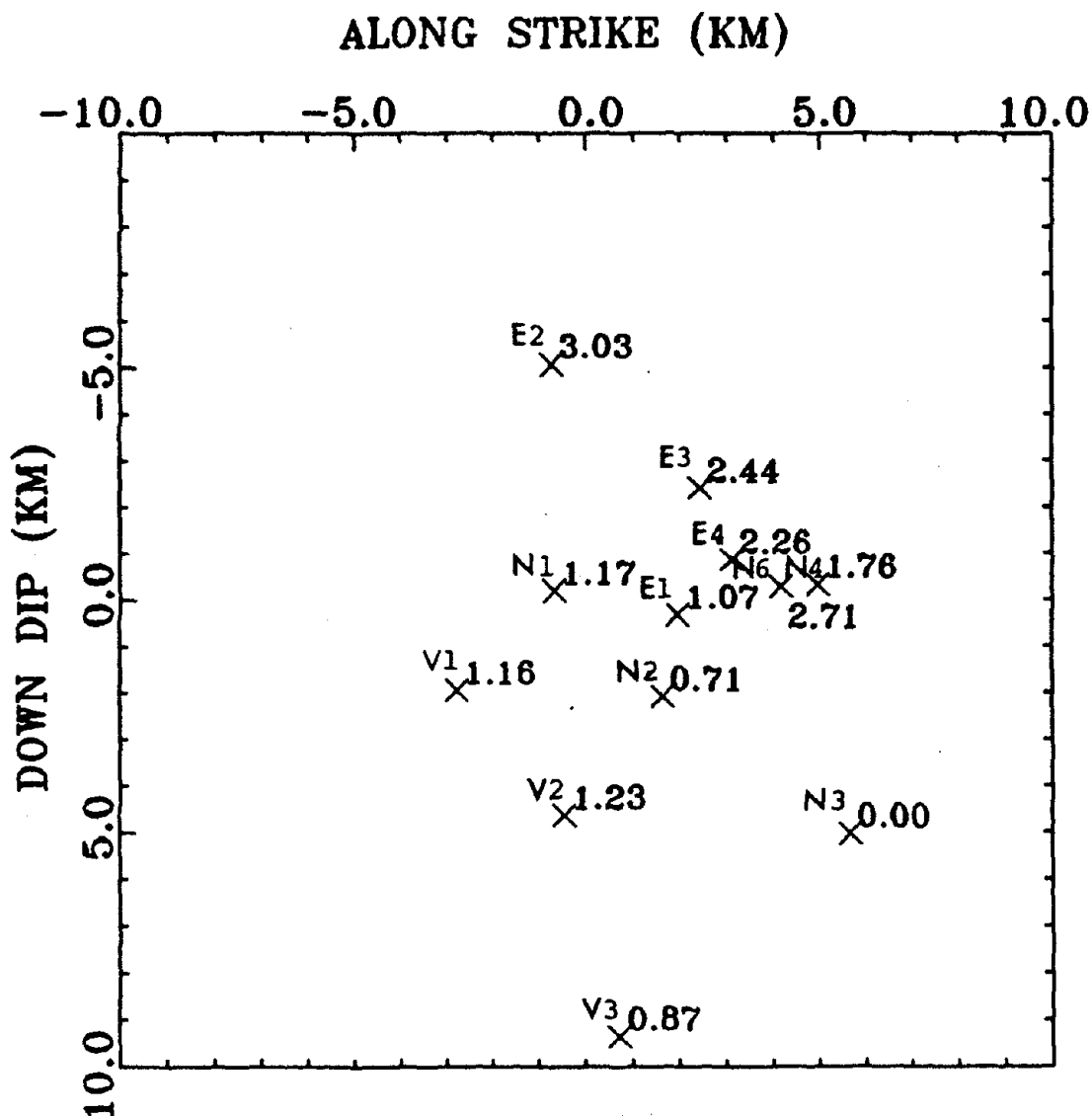


Figure 7.15 Estimated source locations and rupture times using the independent parameters given in Table 7.3 (Model A). Numerical values are the rupture times. The hypocenter inferred by the joint location procedure in Chapter 3 is located at the origin.

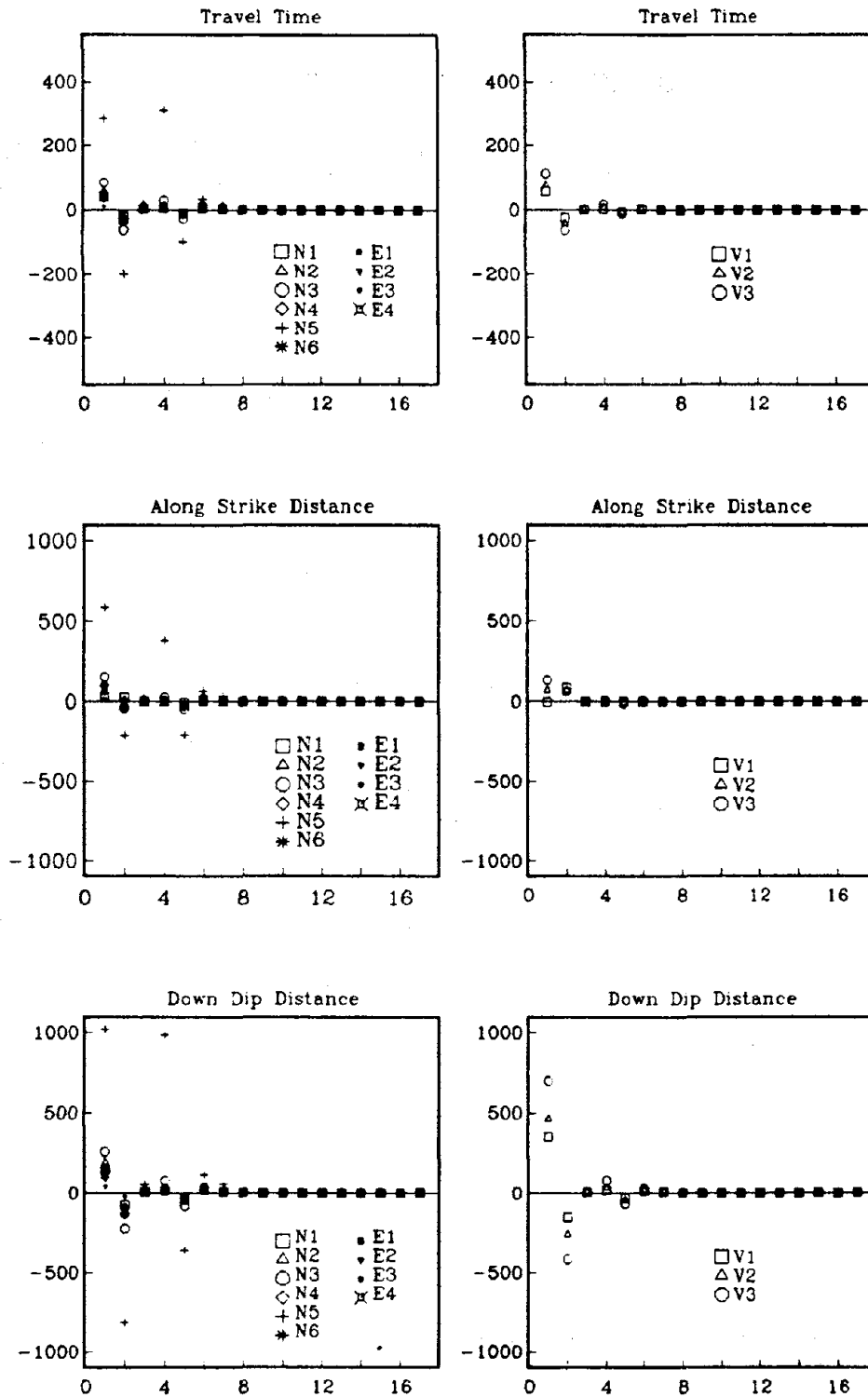


Figure 7.16 Partial derivatives for the S-source (left) and the P-source (right) parameters with respect to: 1 - X component of the slowness vector; 2 - Y component of the slowness vector; 3 - A_1 ; 4 - B_1 ; 5 - A_2 ; 6 - B_2 ; 7 - A_3 ; 8 - B_3 ; 9 - A_4 ; 10 - B_4 ; 11 - A_5 ; 12 - B_5 ; 13 - Fault Strike; 14 - Fault Dip; 15 - X_0 ; 16 - Y_0 ; 17 - Z_0 . Where (X_0, Y_0, Z_0) is the focus, A_i is the wave velocity at the reference depth, and B_i the velocity gradient, in block i (see Table 7.3 and Figure 6.3).

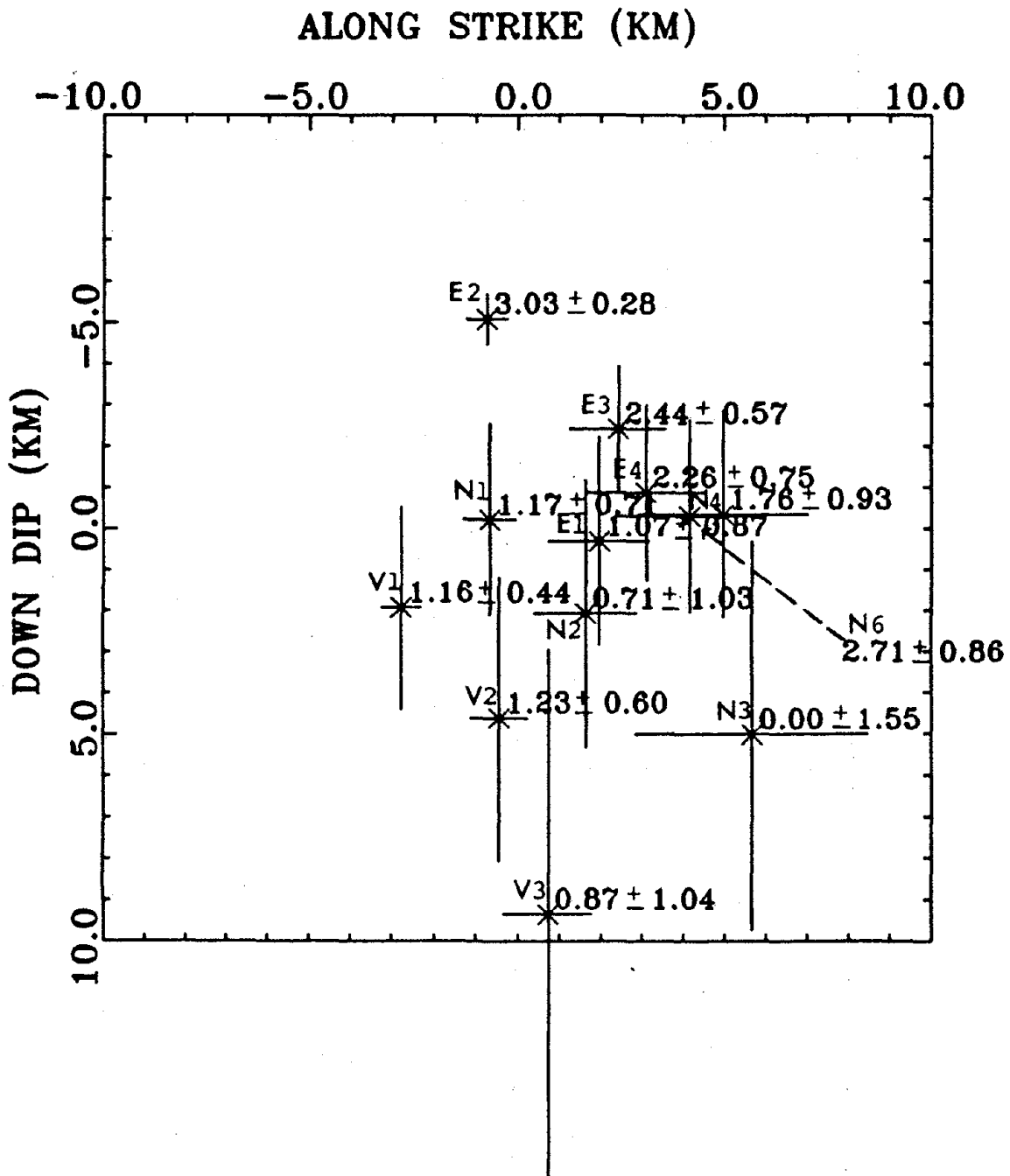


Figure 7.17 Source-parameter estimation standard errors. The calculated standard error include errors from both slowness measurement errors and the uncertainties in the velocity model and epicenter location. The vertical and horizontal bars indicate one standard error of the estimation. The given rupture times are relative to the rupture nucleation time. The numerical value following the rupture time is one standard error.

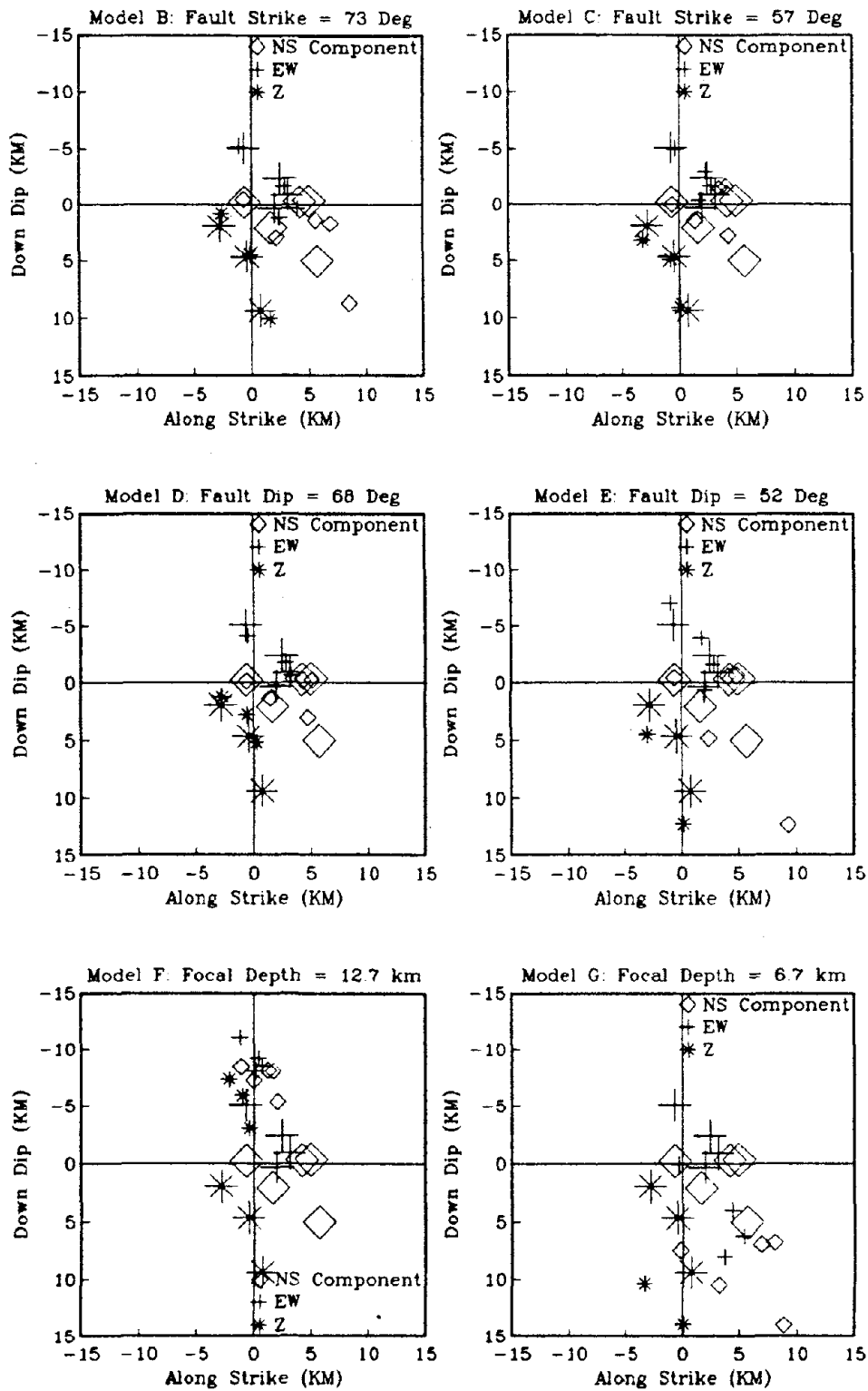


Figure 7.18 Systematic errors of estimated source locations due to the uncertainties in fault strike, fault dip, and focal depth. Models B to G are derived from Model A by changing the value of the independent parameters specified at the top of each diagram. The larger symbols denote the estimated source locations using Model A (see Figure 7.15).

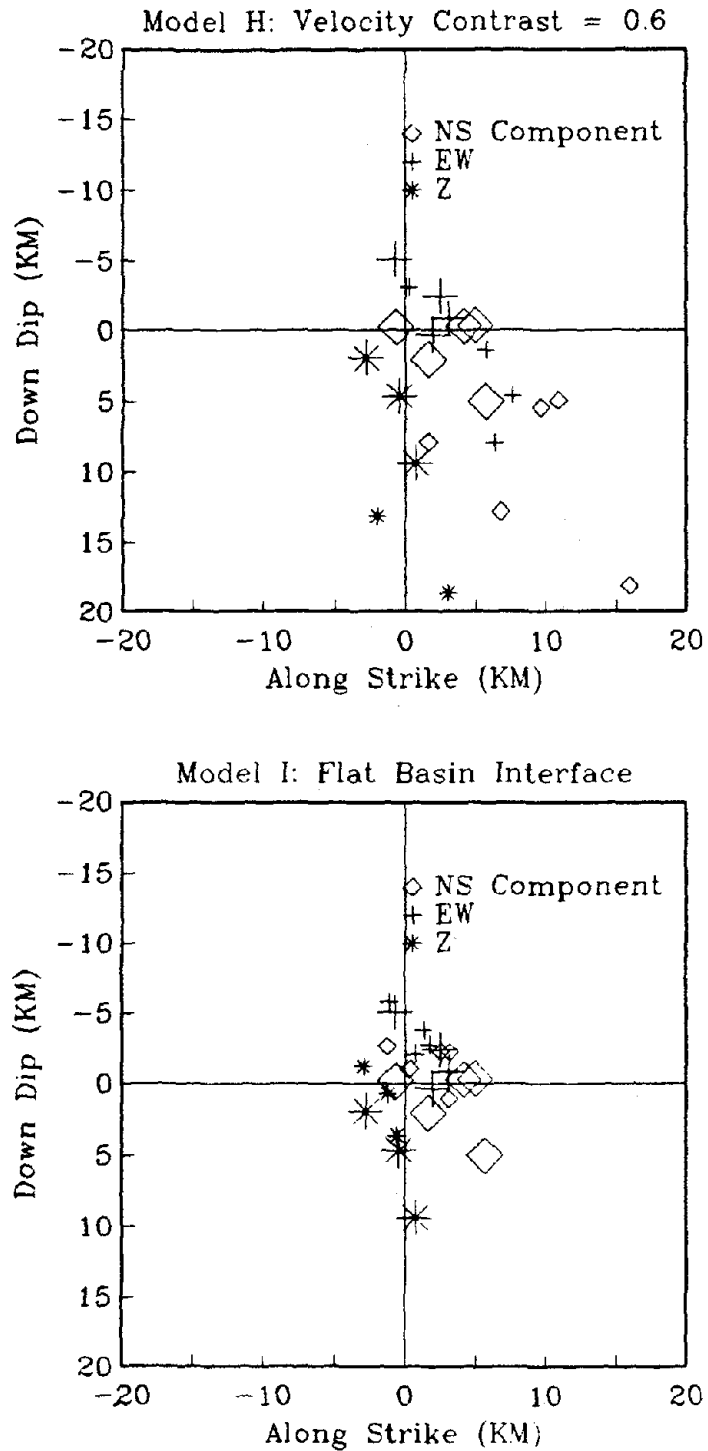


Figure 7.19 Systematic errors of estimated source locations due to the uncertainties in the velocity contrast and the dipping interface. The larger symbols denote the estimated source locations using Model A (see Figure 7.15).

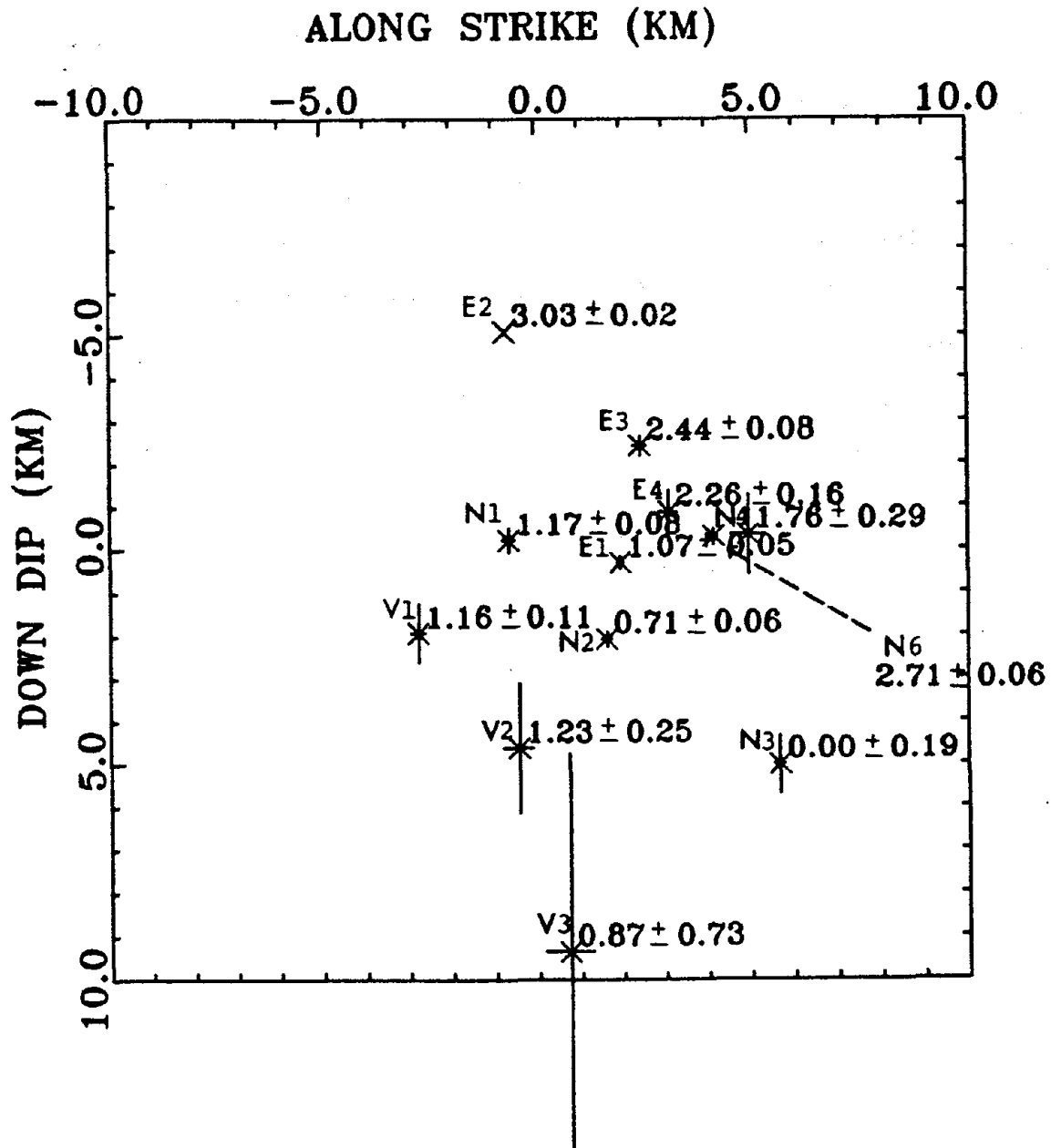


Figure 7.20 Source-parameter estimation standard errors. The calculated standard error includes only errors from the slowness measurement errors. The vertical and horizontal bars indicate one standard error of the estimate. The given rupture times are relative to the rupture nucleation time. The numerical value following the rupture time is one standard error.

CHAPTER 8

SUMMARY OF RESULTS AND RECOMMENDATIONS FOR FUTURE RESEARCH

§8.1 Summary of Results

In this study, several aspects of the problem of estimating source rupture processes using digital data from strong motion seismographic arrays were discussed. The main objective was to investigate the robustness of source mapping by a small aperture array situated near to the ruptured fault, given the precision achievable by present-day seismological methods of array processing, hypocenter location, fault-plane determination, and establishing the subsurface geological structure.

In Chapter 2, the forward model for array recording of a near earthquake was given. The near-source wavefield was decomposed into propagating plane waves whose horizontal slowness vectors were functions of the source positions and the crustal velocity structure. Based on this geophysical model, the inverse problem of determining the source parameters, defined in this study as the source location and rupture time of subevents, was solved by examining the phasing relationship of the recorded wavefield. The strengths of this inverse approach, compared to the waveform inversion approach (Olson and Apsel, 1982; Hartzell and Heaton, 1983; Archuleta, 1984), are (1) the relatively fewer computations involved, (2) the practical assessment of estimation uncertainties, and (3) the simple physical principles used in the source mapping. In addition, this approach does not require full azimuthal coverage of strong-motion sensors around the faulted area and can be applied to an array of a small number of stations.

The July 30, 1986 Taiwan earthquake sequence was used as a test case for the inverse procedure developed. The principal earthquake had a suitable magnitude (M_L 6.2) and epicentral distance (7km) for this type of analysis. In Chapter 3, the focus and fault plane

of the earthquake source were determined by the joint location method (Canas, *et al.*, 1977) and the fault plane solution method (Brillinger *et al.*, 1980). The preferred fault plane agreed, within the standard errors, with the foreshock-aftershock distribution.

In §4.3, the plane-wave assumption was examined critically. It was found that the acceleration data recorded at the inner and middle rings of the SMART1 array did not satisfy the plane-wave model and consequently a subarray which did approximately allow for a robust estimation of slowness was selected. It was inferred that the failure of the plane-wave model in this case may be attributed to a crustal slab of material underneath the array with higher seismic velocities than the surrounding rock (§6.3). This analysis also demonstrated the potentially large estimation bias that may occur because of unknown lateral heterogeneities in the actual crust.

A recent eigen-decomposition scheme for array processing, called the Coherent Signal Subspace (CSS) method, was adopted to estimate the slowness vector of the broad-band wavefield recorded by the selected SMART1 subarray. It was found to be superior to narrow-band methods, such as the conventional beamforming, high resolution, and MUSIC (Multiple Signal Characterization), in the following ways: (1) CSS combines phasing information in a broad frequency band to improve the estimation accuracy and precision, (2) first-order evaluation of the estimation variance and covariance is practical, and (3) CSS does not require the wavefield to be recorded by an array with special symmetry. The recorded vertical and horizontal components of ground motions were used to compute P-wave slowness and S-wave slowness separately using CSS. The estimation results for Event 43 using the SMART1 array data were presented in §7.1, and the estimation variances were given in §7.2. The standard errors of the slowness estimates are of the order 10^{-3} sec/km for the SMART1 installation. The estimated P- and S- slowness vectors were then inverted independently for the P- and S- source parameters in §7.3.

In general, the accuracy of the measurement of source location and origin time with a simple small array is similar to the precision in the traditional problem of earthquake

location using stations with poor azimuthal coverage. The sensitivity of the source values to the slowness measurement (and also to the independent parameters of velocity models, fault-plane orientation and location) are depth-dependent, with a larger sensitivity for deeper sources. The down-dip distance is ill-constrained and strongly correlated with the rupture-time estimate.

The level of sensitivity of the source-parameter estimates to the slowness and independent parameters varies with the wave type used. The numerical results for Event 43 indicate the following: (1) P-source parameters are more susceptible to estimation errors caused by the slowness measurement errors than S-source parameters are; (2) P-source parameters are less sensitive to the uncertainties of the adopted crustal velocity model; (3) for seismic waves radiated from two neighboring fault patches, the arriving P-phases at the array are more closely spaced in arrival time and wave slowness than the arriving S-phases are. Therefore, an array with the capability of higher estimation precision and higher resolution of multiple P-signals is needed for P-source estimation than for S-source. Based on the study of Event 43, it is concluded that S-wave data are superior to P-wave data in measuring fault rupture processes.

The results of source mapping (Figure 7.15) indicated that the rupture of Event 43 nucleates at depth and propagates up-dip from the northeast to the southwest. The estimated rupture times suggested that the early arrivals on the vertical and horizontal components were not from the fault patches that ruptured first; rather they were radiated from slipping patches closer to the array, and, as a consequence, a supershear rupture speed is inferred.

The reliability of this inference of supershear propagation relies on the precision of the source parameter estimates. These errors come from both the systematic errors, which are introduced by the uncertainties of the crustal velocity model and the fault plane, and the random errors induced by the slowness measurement errors. Combination of both systematic and random errors gives large uncertainties in the source-parameter estimates of an individual source point. The estimated parameters have large systematic errors arising

from several assumed fault planes and velocity models given in §7.3.2 and §7.3.3. However, the relative subevent source positions and the order of rupturing remain constant.

The estimated source dimension from Model A (Table 7.3 and Figure 7.20) is $(7.5 \pm 4.7 \times 3.5 \pm 0.6)$ km² and $(10.0 \pm 0.7 \times 6.5 \pm 0.1)$ km², based on the estimated P- and S- sources respectively. The estimation standard errors given above include only the random errors that derive from the slowness measurements. The source dimension values are found to vary significantly with changes in the adopted fault plane and crustal velocity model. In the particular case worked here, the dimension could be different from the estimated source area of Model A by more than a factor of two.

The estimated average rupture-speed of Event 43, based on the S-wave recordings, was 3.94 ± 0.23 km/sec, higher than the local shear velocity. The formal rupture-speed estimates for the earlier stage of rupturing were unrealistically high: 5.58 ± 0.79 km/sec and 6.99 ± 1.62 km/sec, using two pairs of estimated source points that lie roughly along the rupture direction. However, as noted above, these two rupture-speed estimates are strongly conditioned on the adopted fault planes and velocity models. The estimated rupture speeds for the later stage of rupturing were 3.24 ± 0.12 km/sec and 3.07 ± 0.13 km/sec. These two values are lower than the local shear velocity and the values do not vary strongly with the adopted fault planes and velocity models (Table 7.5). The estimated rupture-time differences between the subevent P-sources were too small, compared to the estimation uncertainties, to give a meaningful estimate of rupture speed.

In summary, the algorithms developed in this study more reliably measured the source locations and rupture times of shallow sources in the crust than for deeper sources. The algorithm was successful in determining the rupture sense and direction. One other encouraging observation is the stability of the estimate of the rupture speed at shallow depth, suggesting the seismological potential of measuring at close distances the rupture speed of large and moderate shallow earthquakes.

§8.2 Recommendations and Future Work

The crustal velocity models and fault planes which have been used in this study to calculate the rupture speed were not exhaustive. The results from Model E (Table 7.5) suggest that values for the crustal velocity model and fault plane, which are within the standard errors of those given in Table 7.3, may be found that would give estimates of rupture speed agreeable to those observed from other earthquakes. A more thorough search of crustal velocity model and fault plane over the admissible range of values is thus needed before a conclusive inference about the supershear rupture speed can be made.

The conclusions on the performance of source estimation using strong motion array data reached in this study are based on the numerical application of a general algorithm to one particular earthquake and therefore may not always be applicable to earthquakes occurring in different regions. A general statement of the reliability of this inverse approach would require additional study of the precision and resolution for different types of faulting, using arrays located at various positions with respect to the slipped fault.

A complete theoretical study of the optimal array-fault configuration for measurement of source processes can be accomplished without much computational effort using the simple analytical source mapping formulas for a gradient-velocity crustal model derived in §6.1. Even if it is not close to the actual crustal structure, this gradient-velocity model should capture the first-order effects of seismic ray propagation in the crust. On the observational side, this extension could be accomplished to a certain extent using the high density distribution of strong-motion instruments in California and in a few other countries such as Japan, where a small seismograph array can sometimes be formed by selecting several accelerograph stations that are close to the source region. Such an extension of the algorithm would be particularly useful in studying the source processes of earthquakes that occur on the major fault systems in California because of the shallow source depths, the relatively well-known crustal structure, and the well-constrained fault plane orientations and locations. For example, the highly coherent strong ground motions of the 1989 Loma Prieta

earthquake recorded at the San Francisco Peninsula by the CSMIP (California Strong Motion Instrument Program) and the USGS (U.S. Geological Survey) accelerometers could be regarded as a set of array recordings and hence used to study the rupture process of the Loma Prieta earthquake, even though the along-strike position of the San Francisco area may create some resolution problems.

Most of the strong motion instruments deployed in California do not have a clock which gives the absolute time of the recorded acceleration. As a consequence, only the phasing relationship of the wavefield relative to a selected seismic phase can be recovered by aligning seismograms to that phase (for example, Spudich and Cranswick, 1984). This restriction will not present an important problem if the relative, not the absolute, source positions and rupture times are the main interest. Nevertheless, without complete timing, the plane-wave assumption of the recorded wavefield is not easy to verify and complicated crustal structure may introduce significant slowness-dependent timing errors and therefore bias the slowness estimates of signals whose slowness vectors are not close to that of the aligned seismic phase.

Besides using a large focusing frequency ω_0 in CSS (see §5.3.2), the precision of slowness estimates can also be improved by increasing the spatial extent of the array (Bates and Kanasevich, 1985). However, the trade-off in using a large array is that the curved wavefront and, as demonstrated in this study and others (Aki, 1973; Capon, 1974), lateral crustal heterogeneity may invalidate the plane-wave assumption of the recorded wavefield which is adopted by most modern array processing schemes with high resolution. Therefore, the optimal array size should be determined by the required slowness estimation precision, which will be dependent upon the specific array-fault configuration, and the regional crustal structure.

In this study, because only the phasing relationship of the wavefield recorded at the SMART1 subarray was used for the estimation of source processes, the important source property of coseismic slip was not recoverable. The waveform inversion approach deter-

mines the faulting model, which includes both the rupture time and the accompanying slip at a grid of points on the fault surface, by matching the predicted and the observed waveform at several near stations. With waveform inversion results, the important question of how much extra source information, not obtained from the phasing data, is retrievable can be answered. The spatial extent of the SMART1 array, including the two extra stations of E-01 and E-02 (see Figure 4.1), is large enough to provide the necessary azimuthal coverage needed for the source inversion by waveform matching. The presence of the underlying alluvial basin and the slab structure inferred in this study mandate the computation of at least a two-dimensional, visco-elastic medium response to the seismic source (Green's function). This computation requires considerable coding effort and computer time (Spudich and Archuleta, 1987). One alternative to the use of a theoretical Green function is the use of a smaller aftershock or foreshock (Event 44 or Event 42) as the empirical Green function (Hartzell, 1978; Iwata, 1989).

Results from this study suggest that adding a shallow down-hole array (depth less than 100 meters) to the existing SMART1 surface array would not significantly improve the performance of source mapping. This is because a shallow down-hole array would yield information primarily about the near surface velocity structure, which is not a dominant factor in determining the precision of source estimate (see §7.3).

In contrast, simultaneous observation of the source process by additional arrays, at which the wave azimuth and slowness are significantly different from those of the first array, would allow the use of triangulation to estimate the source positions and the detection of subevent sources relative to which the first array is at the nodal point of the radiation pattern. This additional data would reduce the source estimation variance and improve the parameter resolution. Unfortunately, in this study, due to the limited spatial extent of the SMART1 array, a second subarray that satisfies this condition could not be constructed from the full array (see §6.3). However, a new strong motion array (SMART2) is now being installed at Haulien about 40 km south of the SMART1 array. This array can be used as

a second array in the study of mechanisms of future earthquakes in northeast Taiwan.

In this study, only three P-windows were usable because the strong interference from waves generated by local site effects destroyed the wave coherence of later P arrivals across the selected subarray and prevented the use of records about two seconds after the first arrived P. The SMART2 array is located on firmer soil than the SMART1 array, and the influence of site effects should be much less than SMART1. As a consequence, more P-windows will be usable for source estimation from the recordings of this new array and therefore improve the resolution of the P-source parameters in future earthquakes.

References

- Abrahamson, N.A. (1985). Estimation of seismic wave coherency and rupture velocity using the SMART-1 strong motion array recordings, *EERC Report No. UCB/EERC-85/02*.
- Abrahamson, N.A. and B.A. Bolt (1987). Array analysis and synthesis mapping of strong seismic motion, In: B.A. Bolt (editor), *Strong motion synthetics: Computational techniques series*, Academic Press, New York.
- Abrahamson, N.A., B.A. Bolt, R.B. Darragh, J. Penzien, and Y.B. Tsai (1987). The SMART-1 accelerograph array (1980 - 1987): A review, *Earthquake Spectra*, **3**, 263 - 287.
- Abrahamson, N.A. and R.B. Darragh (1985). Observation of a double event at regional distances: the Morgan Hill earthquake of 24 April, 1984, *Bull. Seismol. Soc. Am.*, **75**, 1461 - 1464.
- Aki, K. (1968). Seismic displacements near a fault, *J. Geophys. Res.*, **73**, 5359 - 5376.
- Aki, K. (1973). Scattering of P waves under the Montana LASA, *J. Geophys. Res.*, **78**, 1334 - 1346.
- Aki, K. (1981). Asperities, barriers and characteristics of earthquakes, *J. Geophys. Res.*, **89**, 5867 - 5872.
- Aki, K. and P.G. Richards (1980). *Quantitative Seismology Theory and Methods*, W.H. Freeman and Co., San Francisco.
- Anderson, D.G. and Y.K. Tang (1989). Summary of soil characterization program for the Lotung large-scale seismic experiment, *Proc. EPRI/NRC/TPC workshop on seismic soil-structure interaction analysis techniques using data from Lotung, Taiwan*, EPRI, NP-6154
- Archuleta, R.J. (1984). A faulting model for the 1979 Imperial Valley earthquake, *J. Geophys. Res.*, **89**, 4559 - 4585.
- Bates, A.C. and E.R. Kanasevich (1985). Seismic array design, In: *Seismic Wave Attenuation*, (ed. G. Dohr), Geophysical Press, London..
- Benioff, H. F. Press, and S.W. Smith (1961). Excitation of the free oscillations of the earth by earthquakes, *J. Geophys. Res.*, **66**, 605 - 618.
- Beroza, G.C. and P. Spudich (1988). Linearized inversion for fault rupture behavior: Application to the 1984, Morgan Hill, California, earthquake, *J. Geophys. Res.*, **93**, 6275 - 6296.
- Boatwright, J. and D.M. Boore (1982). Analysis of the ground accelerations radiated by the 1980 Livermore valley earthquakes for directivity and dynamic source characteristics, *Bull. Seismol. Soc. Am.*, **72**, 1843 - 1865.

- Bolt, B.A. (1988). *Earthquakes, A primer*, 2nd Edition, W.H. Freeman and Company, New York.
- Bolt, B.A., C.H. Loh, J. Penzien, Y.B. Tsai and Y.T. Yeh (1982). Preliminary report on the SMART1 strong motion array in Taiwan, *EERC Report No. UCB/EERC-82/13*.
- Boore, D.M. and W.B. Joyner (1978). The influence of rupture incoherence on seismic directivity, *Bull. Seismol. Soc. Am.*, **64**, 283 – 300.
- Bostwick, T.K., P.A. Spudich, and D. Oppenheimer (1985). Suppressing aliases and side-lobes in frequency/wavenumber transforms through slowness and frequency, *EOS (abstract)*, **66**, 313.
- Brillinger, D.R. (1981). *Time Series: Data Analysis and Theory*, expanded ed. San Francisco, CA: Holden-Day.
- Brillinger, D.R., A. Udias, and B.A. Bolt (1980). A probability model for regional focal mechanism solutions, *Bull. Seismol. Soc. Am.*, **70**, 149 – 170.
- Bullen, K.E. and B.A. Bolt (1985). *An introduction to the theory of seismology*, Cambridge University Press, New York.
- Canas, J., R.D. Miller, and R.A. Uhrhammer (1977). *Bulletin of the Seismographic Stations*, University of California at Berkeley, Vol. 47, No.1, 51 – 54.
- Capon, J. (1969). High-resolution frequency-wavenumber spectrum analysis, *Proc. IEEE*, **57**, 1408 – 1418.
- Capon, J. (1974). Characterization of crust and upper mantle structure under LASA as a random medium, *Bull. Seismol. Soc. Am.*, **64**, 235 – 266.
- Carter, G.C. (1981). Time delay estimation for passive sonar signal processing, *IEEE Trans. Acoust., Speech, Signal Processing*, ASSP-29, 463 – 470.
- Chiang, S.C. (1976). A seismic refraction prospecting of the Ilan plain (in Chinese), *Mining Tech.*, **14**, 215 – 221.
- Choy, G.L. (1985). Source parameters of the Coalinga, California, earthquake of May 2, 1983 Coalinga earthquake, USGS OFR 85-44, 83 – 131.
- Darragh, R.B. (1987). Analysis of near-source waves: separation of wave types using strong motion array recordings, *EERC Report No. UCB/EERC-88/08*.
- Der, Z.A. and E.A. Flinn (1975). The applicability of principal component analysis to the separation of multiple plane-wave signals, *Bull. Seismol. Soc. Am.*, **65**, 627 – 635.
- Filson, J. and T.V. McEvelly (1967). Love wave spectra and the mechanism of the 1966 Parkfield sequence. *Bull. Seismol. Soc. Am.*, **57**, 1245 – 1259.
- Goldstein, P. (1988). Array measurements of earthquake rupture, *Ph.D. Dissertation*, 193 pp., University of California, Santa Barbara.

- Goldstein, P., and R.J. Archuleta (1987). Array analysis of seismic signal, *Geophys. Res. Lett.*, **14**, 13 – 16.
- Goldstein, P. and R.J. Archuleta (1991a). Deterministic frequency-wavenumber methods and direct measurements of rupture propagation during earthquakes using a dense array: Theory and methods, *J. Geophys. Res.*, **96**, 6173 – 6185.
- Goldstein, P. and R.J. Archuleta (1991b). Direct measurements of rupture propagation during earthquakes using a dense array: Data analysis, *J. Geophys. Res.*, **96**, 6187 – 6198.
- Hartzell, S.H. (1978). Earthquake aftershocks as Green's functions, *Geophys. Res. Letters*, **5**, 1 – 4.
- Hartzell, S.H. (1989). Comparison of seismic waveform inversion results for the rupture history of a finite fault: Application to the 1986 North Palm Springs, California, earthquake, *J. Geophys. Res.*, **94**, 7515 – 7534.
- Hartzell, S.H. and T.H. Heaton (1983). Inversion of strong ground motion and teleseismic waveform data for the fault rupture history of the 1979 Imperial Valley, California, earthquake, *Bull. Seismol. Soc. Am.*, **73**, 1553 – 1583.
- Hsu, S.G. (1987). Interpretation of the geomagnetic anomalies of Ilan plain, Taiwan, by DGRF model and the approximate gradient method, (in Chinese) *M.S. Thesis*, Institute of Oceanography, National Taiwan University, 57pp.
- Hung, H. and M. Kaveh (1988). Focusing matrices for coherent signal-subspace processing, *IEEE Trans. Acoust., Speech, Signal Processing*, ASSP-36, 1272 – 1281.
- Iida, M. (1990). Optimum strong-motion array geometry for source inversion – II, *Earthquake Eng. Struct. Dyn.*, **19**, 35 – 44.
- Iida, M., T. Miyatake, and K. Shimazaki (1990a). Relationship between strong-motion array parameters and the accuracy of source inversion and physical waves, *Bull. Seismol. Soc. Am.*, **80**, 1533 – 1552.
- Iida, M., T. Miyatake, and K. Shimazaki (1990b). Preliminary analysis of resolving power of existing strong-motion arrays for source inversion. *J. Phys. Earth*, **38**, 285 – 304.
- Iwata, T. (1989). A study of earthquake source characteristics from high-frequency strong motions, *Ph.D. Thesis*, Kyoto University, Japan.
- Jenkins, G.M. and D.G. Watts (1968). *Spectral analysis and its applications*, San Francisco: Holden-Day.
- Kanamori, H. and G.S. Stewart (1978). Seismological aspects of the Guatemala earthquake of February 4, 1976, *J. Geophys. Res.*, **83**, 3427 – 3434.
- Kasahara, K. (1981). *Earthquake mechanics*, Cambridge Univ. Press.
- Kaveh, M. and A.J. Barabell (1986). The statistical performance of the MUSIC and the minimum-norm algorithms in resolving plane waves in noise, *IEEE Trans. Acoust., Speech, Signal Processing*, ASSP-34, 331 – 341.

- Kumaresan, R. and D.W. Tufts (1983). Estimating the angles of arrival of multiple plane waves, *IEEE Trans. Aerosp. Electron. Syst.*, AES 19.
- Lee, W.H.K and S.W. Stewart (1981). *Principles and applications of micro-earthquake networks*, Academic Press Inc.
- McLaughlin, K.L. (1982). Spatial coherency of seismic waveforms, *Ph.D. Dissertation*, 275 pp., University of California, Berkeley.
- McLaughlin, K.L., L. Johnson, and T. McEvilly (1983). Two-dimensional array measurements of near-source ground accelerations, *Bull. Seismol. Soc. Am.*, **73**, 349 – 375.
- Olson, A.H. and R.J. Apsel (1982). Finite faults and inverse theory with applications to the 1979 Imperial Valley earthquake, *Bull. Seismol. Soc. Am.*, **72**, 1969 – 2001.
- Porat, B. and B. Friedlander (1986). Analysis of the asymptotic relative efficiency of the MUSIC algorithm, *IEEE Trans. Acoust., Speech, Signal Processing*, ASSP-36, 532 – 543.
- Reid, H.F. (1911). The elastic-rebound theory of earthquakes, *Bull. Dep. Geol. Univ. Calif.*, **6**, 412 – 444.
- Rial, J.A. (1978). The Caracas, Venezuela, earthquake of July 1967: a multiple-source event, *J. Geophys. Res.*, **83**, 5405 – 5414.
- Schmidt, R.O. (1981). A signal subspace approach to multiple emitter location and spectral estimation, *Ph.D. Dissertation*, 201 pp., Stanford University, Stanford, California,
- Schmidt, R.O. (1986). Multiple emitter location and signal parameter estimation, *IEEE Trans. Antennas and Propagation*, **34**, 276 – 280.
- Scholz, C.H. (1990). *The mechanics of earthquakes and faulting*, Cambridge Univ. Press.
- Spudich, P. (1986). Strong ground motion prediction in realistic Earth structure, In: M.L. Jacobson and T.R. Rodriguez (compilers), *Natural Earthquake Hazards Reduction Program, Summary of Technical Reports*, XXI, USGS OFR 86-31, 628 – 629.
- Spudich, P. and R.A. Archuleta (1987). Techniques for earthquake ground-motion calculation with application to source parameterization of finite faults, In: B.A. Bolt (editor), *Strong motion synthetics: Computational techniques series*, Academic Press, New York.
- Spudich, P. and E. Cranswick (1984). Direct observation of rupture propagation during the 1979 Imperial Valley earthquake using a short baseline accelerometer array, *Bull. Seismol. Soc. Am.*, **74**, 2083 – 2114.
- Spudich, P. and L.N. Frazer (1984). Use of ray theory to calculate high-frequency radiation from earthquake sources having spatially variable rupture velocity and stress drop, *Bull. Seismol. Soc. Am.*, **74**, 2061 – 2082.
- Spudich, P. and D. Oppenheimer (1986). Dense seismograph array observations of earthquake rupture dynamics, In: *Proc. Fifth Ewing Symposium on Earthquake Source Mechanics*, Edited by S. Das, J. Boatwright, C.H. Scholz, 285-296, American Geophysical Union Monograph, Washington D.C.

- VanDecar, J.C. and R.S. Crosson (1990). Determination of teleseismic relative phase arrival times using multi-channel cross correlation and least squares, *Bull. Seismol. Soc. Am.*, **80**, 150 - 169.
- Wang, H. and M. Kaveh (1985). Coherent signal-subspace processing for the detection and estimation of angles of arrival of multiple wide-band sources, *IEEE Trans. Acoust., Speech, Signal Processing*, ASSP-33, 823 - 831.
- Wax, M. and T. Kailath (1983). Estimating the number of signals by information theoretic criteria, In *Proc. ASSP Spectral Estimation Workshop II*, Tampa, FL, 192 - 196
- Weiss, A.J., A.S. Willsky, and C.L. Bernard (1988). Eigenstructure approach for array processing with unknown intensity coefficients, *IEEE Trans. Acoust., Speech, Signal Processing*, ASSP-36, 1613 - 1617.
- Wen, K.L. and Y.T. Yeh (1984). Seismic velocity structure beneath the SMART1 array, *Bull. Inst. Earth Sci., Academia Sinica*, **4**, 51 - 71.
- Woods, J.W. and P.R. Lintz (1973). Plane waves at small arrays, *Geophysics*, **38**, 1023 - 1041.
- Wyss, M. and J. Brune (1967). The Alaska earthquake of 28 March 1964: A complex multiple rupture, *Bull. Seismol. Soc. Am.*, **57**, 1017 - 1023.
- Yeh, Y.H. (1987). Three dimensional crustal and upper mantle structures of northern Taiwan from earthquake and gravity data, *Ph.D. Dissertation*, 142 pp., National Central University, Taiwan.
- Yeh, Y.H., C.H. Lin, and S.W. Roecker (1989). A study of upper crustal structures beneath northeastern Taiwan: possible evidence of the western extension of Okinawa trough, *Proc. Geol. Soc. China*, **32**, 139 - 156.
- Yu, S.B. and Y.B. Tsai (1979). Geomagnetic anomalies of Ilan plain, Taiwan, *Pet. Geol. Taiwan*, **16**, 19 - 27.

EARTHQUAKE ENGINEERING RESEARCH CENTER REPORT SERIES

EERC reports are available from the National Information Service for Earthquake Engineering(NISEE) and from the National Technical Information Service(NTIS). Numbers in parentheses are Accession Numbers assigned by the National Technical Information Service; these are followed by a price code. Contact NTIS, 5285 Port Royal Road, Springfield Virginia, 22161 for more information. Reports without Accession Numbers were not available from NTIS at the time of printing. For a current complete list of EERC reports (from EERC 67-1) and availability information, please contact University of California, EERC, NISEE, 1301 South 46th Street, Richmond, California 94804.

- UCB/EERC-81/01 "Control of Seismic Response of Piping Systems and Other Structures by Base Isolation," by Kelly, J.M., January 1981, (PB81 200 735)A05.
- UCB/EERC-81/02 "OPTNSR- An Interactive Software System for Optimal Design of Statically and Dynamically Loaded Structures with Nonlinear Response," by Bhatti, M.A., Ciampi, V. and Pister, K.S., January 1981, (PB81 218 851)A09.
- UCB/EERC-81/03 "Analysis of Local Variations in Free Field Seismic Ground Motions," by Chen, J.-C., Lysmer, J. and Seed, H.B., January 1981, (AD-A099508)A13.
- UCB/EERC-81/04 "Inelastic Structural Modeling of Braced Offshore Platforms for Seismic Loading," by Zayas, V.A., Shing, P.-S.B., Mahin, S.A. and Popov, E.P., January 1981, INEL4, (PB82 138 777)A07.
- UCB/EERC-81/05 "Dynamic Response of Light Equipment in Structures," by Der Kiureghian, A., Sackman, J.L. and Nour-Omid, B., April 1981, (PB81 218 497)A04.
- UCB/EERC-81/06 "Preliminary Experimental Investigation of a Broad Base Liquid Storage Tank," by Bouwkamp, J.G., Kollegger, J.P. and Stephen, R.M., May 1981, (PB82 140 385)A03.
- UCB/EERC-81/07 "The Seismic Resistant Design of Reinforced Concrete Coupled Structural Walls," by Aktan, A.E. and Bertero, V.V., June 1981, (PB82 113 358)A11.
- UCB/EERC-81/08 "Unassigned," by Unassigned, 1981.
- UCB/EERC-81/09 "Experimental Behavior of a Spatial Piping System with Steel Energy Absorbers Subjected to a Simulated Differential Seismic Input," by Stierner, S.F., Godden, W.G. and Kelly, J.M., July 1981, (PB82 201 898)A04.
- UCB/EERC-81/10 "Evaluation of Seismic Design Provisions for Masonry in the United States," by Sveinsson, B.I., Mayes, R.L. and McNiven, H.D., August 1981, (PB82 166 075)A08.
- UCB/EERC-81/11 "Two-Dimensional Hybrid Modelling of Soil-Structure Interaction," by Tzong, T.-J., Gupta, S. and Penzien, J., August 1981, (PB82 142 118)A04.
- UCB/EERC-81/12 "Studies on Effects of Infills in Seismic Resistant R/C Construction," by Brokken, S. and Bertero, V.V., October 1981, (PB82 166 190)A09.
- UCB/EERC-81/13 "Linear Models to Predict the Nonlinear Seismic Behavior of a One-Story Steel Frame," by Valdimarsson, H., Shah, A.H. and McNiven, H.D., September 1981, (PB82 138 793)A07.
- UCB/EERC-81/14 "TLUSH: A Computer Program for the Three-Dimensional Dynamic Analysis of Earth Dams," by Kagawa, T., Mejia, L.H., Seed, H.B. and Lysmer, J., September 1981, (PB82 139 940)A06.
- UCB/EERC-81/15 "Three Dimensional Dynamic Response Analysis of Earth Dams," by Mejia, L.H. and Seed, H.B., September 1981, (PB82 137 274)A12.
- UCB/EERC-81/16 "Experimental Study of Lead and Elastomeric Dampers for Base Isolation Systems," by Kelly, J.M. and Hodder, S.B., October 1981, (PB82 166 182)A05.
- UCB/EERC-81/17 "The Influence of Base Isolation on the Seismic Response of Light Secondary Equipment," by Kelly, J.M., April 1981, (PB82 255 266)A04.
- UCB/EERC-81/18 "Studies on Evaluation of Shaking Table Response Analysis Procedures," by Blondet, J. M., November 1981, (PB82 197 278)A10.
- UCB/EERC-81/19 "DELIGHT.STRUCT: A Computer-Aided Design Environment for Structural Engineering," by Balling, R.J., Pister, K.S. and Polak, E., December 1981, (PB82 218 496)A07.
- UCB/EERC-81/20 "Optimal Design of Seismic-Resistant Planar Steel Frames," by Balling, R.J., Ciampi, V. and Pister, K.S., December 1981, (PB82 220 179)A07.
- UCB/EERC-82/01 "Dynamic Behavior of Ground for Seismic Analysis of Lifeline Systems," by Sato, T. and Der Kiureghian, A., January 1982, (PB82 218 926)A05.
- UCB/EERC-82/02 "Shaking Table Tests of a Tubular Steel Frame Model," by Ghanaat, Y. and Clough, R.W., January 1982, (PB82 220 161)A07.
- UCB/EERC-82/03 "Behavior of a Piping System under Seismic Excitation: Experimental Investigations of a Spatial Piping System supported by Mechanical Shock Arrestors," by Schneider, S., Lee, H.-M. and Godden, W. G., May 1982, (PB83 172 544)A09.
- UCB/EERC-82/04 "New Approaches for the Dynamic Analysis of Large Structural Systems," by Wilson, E.L., June 1982, (PB83 148 080)A05.
- UCB/EERC-82/05 "Model Study of Effects of Damage on the Vibration Properties of Steel Offshore Platforms," by Shahrivar, F. and Bouwkamp, J.G., June 1982, (PB83 148 742)A10.
- UCB/EERC-82/06 "States of the Art and Practice in the Optimum Seismic Design and Analytical Response Prediction of R/C Frame Wall Structures," by Aktan, A.E. and Bertero, V.V., July 1982, (PB83 147 736)A05.
- UCB/EERC-82/07 "Further Study of the Earthquake Response of a Broad Cylindrical Liquid-Storage Tank Model," by Manos, G.C. and Clough, R.W., July 1982, (PB83 147 744)A11.
- UCB/EERC-82/08 "An Evaluation of the Design and Analytical Seismic Response of a Seven Story Reinforced Concrete Frame," by Charney, F.A. and Bertero, V.V., July 1982, (PB83 157 628)A09.
- UCB/EERC-82/09 "Fluid-Structure Interactions: Added Mass Computations for Incompressible Fluid," by Kuo, J.S.-H., August 1982, (PB83 156 281)A07.
- UCB/EERC-82/10 "Joint-Opening Nonlinear Mechanism: Interface Smear Crack Model," by Kuo, J.S.-H., August 1982, (PB83 149 195)A05.

- UCB/EERC-82/11 "Dynamic Response Analysis of Tchi Dam," by Clough, R.W., Stephen, R.M. and Kuo, J.S.-H., August 1982, (PB83 147 496)A06.
- UCB/EERC-82/12 "Prediction of the Seismic Response of R/C Frame-Coupled Wall Structures," by Aktan, A.E., Bertero, V.V. and Piazzi, M., August 1982, (PB83 149 203)A09.
- UCB/EERC-82/13 "Preliminary Report on the Smart 1 Strong Motion Array in Taiwan," by Bolt, B.A., Loh, C.H., Penzien, J. and Tsai, Y.B., August 1982, (PB83 159 400)A10.
- UCB/EERC-82/14 "Seismic Behavior of an Eccentrically X-Braced Steel Structure," by Yang, M.S., September 1982, (PB83 260 778)A12.
- UCB/EERC-82/15 "The Performance of Stairways in Earthquakes," by Roha, C., Axley, J.W. and Bertero, V.V., September 1982, (PB83 157 693)A07.
- UCB/EERC-82/16 "The Behavior of Submerged Multiple Bodies in Earthquakes," by Liao, W.-G., September 1982, (PB83 158 709)A07.
- UCB/EERC-82/17 "Effects of Concrete Types and Loading Conditions on Local Bond-Slip Relationships," by Cowell, A.D., Popov, E.P. and Bertero, V.V., September 1982, (PB83 153 577)A04.
- UCB/EERC-82/18 "Mechanical Behavior of Shear Wall Vertical Boundary Members: An Experimental Investigation," by Wagner, M.T. and Bertero, V.V., October 1982, (PB83 159 764)A05.
- UCB/EERC-82/19 "Experimental Studies of Multi-support Seismic Loading on Piping Systems," by Kelly, J.M. and Cowell, A.D., November 1982, (PB90 262 684)A07.
- UCB/EERC-82/20 "Generalized Plastic Hinge Concepts for 3D Beam-Column Elements," by Chen, P. F.-S. and Powell, G.H., November 1982, (PB83 247 981)A13.
- UCB/EERC-82/21 "ANSR-II: General Computer Program for Nonlinear Structural Analysis," by Oughourlian, C.V. and Powell, G.H., November 1982, (PB83 251 330)A12.
- UCB/EERC-82/22 "Solution Strategies for Statically Loaded Nonlinear Structures," by Simons, J.W. and Powell, G.H., November 1982, (PB83 197 970)A06.
- UCB/EERC-82/23 "Analytical Model of Deformed Bar Anchorages under Generalized Excitations," by Ciampi, V., Elgehausen, R., Bertero, V.V. and Popov, E.P., November 1982, (PB83 169 532)A06.
- UCB/EERC-82/24 "A Mathematical Model for the Response of Masonry Walls to Dynamic Excitations," by Sucuoglu, H., Mengi, Y. and McNiven, H.D., November 1982, (PB83 169 011)A07.
- UCB/EERC-82/25 "Earthquake Response Considerations of Broad Liquid Storage Tanks," by Cambra, F.J., November 1982, (PB83 251 215)A09.
- UCB/EERC-82/26 "Computational Models for Cyclic Plasticity, Rate Dependence and Creep," by Mosaddad, B. and Powell, G.H., November 1982, (PB83 245 829)A08.
- UCB/EERC-82/27 "Inelastic Analysis of Piping and Tubular Structures," by Mahasuverachai, M. and Powell, G.H., November 1982, (PB83 249 987)A07.
- UCB/EERC-83/01 "The Economic Feasibility of Seismic Rehabilitation of Buildings by Base Isolation," by Kelly, J.M., January 1983, (PB83 197 988)A05.
- UCB/EERC-83/02 "Seismic Moment Connections for Moment-Resisting Steel Frames," by Popov, E.P., January 1983, (PB83 195 412)A04.
- UCB/EERC-83/03 "Design of Links and Beam-to-Column Connections for Eccentrically Braced Steel Frames," by Popov, E.P. and Malley, J.O., January 1983, (PB83 194 811)A04.
- UCB/EERC-83/04 "Numerical Techniques for the Evaluation of Soil-Structure Interaction Effects in the Time Domain," by Bayo, E. and Wilson, E.L., February 1983, (PB83 245 605)A09.
- UCB/EERC-83/05 "A Transducer for Measuring the Internal Forces in the Columns of a Frame-Wall Reinforced Concrete Structure," by Sause, R. and Bertero, V.V., May 1983, (PB84 119 494)A06.
- UCB/EERC-83/06 "Dynamic Interactions Between Floating Ice and Offshore Structures," by Croteau, P., May 1983, (PB84 119 486)A16.
- UCB/EERC-83/07 "Dynamic Analysis of Multiply Tuned and Arbitrarily Supported Secondary Systems," by Igusa, T. and Der Kiureghian, A., July 1983, (PB84 118 272)A11.
- UCB/EERC-83/08 "A Laboratory Study of Submerged Multi-body Systems in Earthquakes," by Ansari, G.R., June 1983, (PB83 261 842)A17.
- UCB/EERC-83/09 "Effects of Transient Foundation Uplift on Earthquake Response of Structures," by Yim, C.-S. and Chopra, A.K., June 1983, (PB83 261 396)A07.
- UCB/EERC-83/10 "Optimal Design of Friction-Braced Frames under Seismic Loading," by Austin, M.A. and Pister, K.S., June 1983, (PB84 119 288)A06.
- UCB/EERC-83/11 "Shaking Table Study of Single-Story Masonry Houses: Dynamic Performance under Three Component Seismic Input and Recommendations," by Manos, G.C., Clough, R.W. and Mayes, R.L., July 1983, (UCB/EERC-83/11)A08.
- UCB/EERC-83/12 "Experimental Error Propagation in Pseudodynamic Testing," by Shiing, P.B. and Mahin, S.A., June 1983, (PB84 119 270)A09.
- UCB/EERC-83/13 "Experimental and Analytical Predictions of the Mechanical Characteristics of a 1/5-scale Model of a 7-story R/C Frame-Wall Building Structure," by Aktan, A.E., Bertero, V.V., Chowdhury, A.A. and Nagashima, T., June 1983, (PB84 119 213)A07.
- UCB/EERC-83/14 "Shaking Table Tests of Large-Panel Precast Concrete Building System Assemblages," by Oliva, M.G. and Clough, R.W., June 1983, (PB86 110 210/AS)A11.
- UCB/EERC-83/15 "Seismic Behavior of Active Beam Links in Eccentrically Braced Frames," by Hjelmstad, K.D. and Popov, E.P., July 1983, (PB84 119 676)A09.
- UCB/EERC-83/16 "System Identification of Structures with Joint Rotation," by Dimsdale, J.S., July 1983, (PB84 192 210)A06.
- UCB/EERC-83/17 "Construction of Inelastic Response Spectra for Single-Degree-of-Freedom Systems," by Mahin, S. and Lin, J., June 1983, (PB84 208 834)A05.
- UCB/EERC-83/18 "Interactive Computer Analysis Methods for Predicting the Inelastic Cyclic Behaviour of Structural Sections," by Kaba, S. and Mahin, S., July 1983, (PB84 192 012)A06.
- UCB/EERC-83/19 "Effects of Bond Deterioration on Hysteretic Behavior of Reinforced Concrete Joints," by Filippou, F.C., Popov, E.P. and Bertero, V.V., August 1983, (PB84 192 020)A10.

- UCB/EERC-83/20 "Correlation of Analytical and Experimental Responses of Large-Panel Precast Building Systems," by Oliva, M.G., Clough, R.W., Velkov, M. and Gavrilovic, P., May 1988, (PB90 262 692)A06.
- UCB/EERC-83/21 "Mechanical Characteristics of Materials Used in a 1/5 Scale Model of a 7-Story Reinforced Concrete Test Structure," by Bertero, V.V., Aktan, A.E., Harris, H.G. and Chowdhury, A.A., October 1983, (PB84 193 697)A05.
- UCB/EERC-83/22 "Hybrid Modelling of Soil-Structure Interaction in Layered Media," by Tzong, T.-J. and Penzien, J., October 1983, (PB84 192 178)A08.
- UCB/EERC-83/23 "Local Bond Stress-Slip Relationships of Deformed Bars under Generalized Excitations," by Elgehausen, R., Popov, E.P. and Bertero, V.V., October 1983, (PB84 192 848)A09.
- UCB/EERC-83/24 "Design Considerations for Shear Links in Eccentrically Braced Frames," by Malley, J.O. and Popov, E.P., November 1983, (PB84 192 186)A07.
- UCB/EERC-84/01 "Pseudodynamic Test Method for Seismic Performance Evaluation: Theory and Implementation," by Shing, P.-S.B. and Mahin, S.A., January 1984, (PB84 190 644)A08.
- UCB/EERC-84/02 "Dynamic Response Behavior of Kiang Hong Dian Dam," by Clough, R.W., Chang, K.-T., Chen, H.-Q. and Stephen, R.M., April 1984, (PB84 209 402)A08.
- UCB/EERC-84/03 "Refined Modelling of Reinforced Concrete Columns for Seismic Analysis," by Kaba, S.A. and Mahin, S.A., April 1984, (PB84 234 384)A06.
- UCB/EERC-84/04 "A New Floor Response Spectrum Method for Seismic Analysis of Multiply Supported Secondary Systems," by Asfura, A. and Der Kiureghian, A., June 1984, (PB84 239 417)A06.
- UCB/EERC-84/05 "Earthquake Simulation Tests and Associated Studies of a 1/5th-scale Model of a 7-Story R/C Frame-Wall Test Structure," by Bertero, V.V., Aktan, A.E., Charney, F.A. and Sause, R., June 1984, (PB84 239 409)A09.
- UCB/EERC-84/06 "Unassigned," by Unassigned, 1984.
- UCB/EERC-84/07 "Behavior of Interior and Exterior Flat-Plate Connections subjected to Inelastic Load Reversals," by Zee, H.L. and Moehle, J.P., August 1984, (PB86 117 629/AS)A07.
- UCB/EERC-84/08 "Experimental Study of the Seismic Behavior of a Two-Story Flat-Plate Structure," by Moehle, J.P. and Diebold, J.W., August 1984, (PB86 122 553/AS)A12.
- UCB/EERC-84/09 "Phenomenological Modeling of Steel Braces under Cyclic Loading," by Ikeda, K., Mahin, S.A. and Dermitzakis, S.N., May 1984, (PB86 132 198/AS)A08.
- UCB/EERC-84/10 "Earthquake Analysis and Response of Concrete Gravity Dams," by Fenves, G. and Chopra, A.K., August 1984, (PB85 193 902/AS)A11.
- UCB/EERC-84/11 "EAGD-84: A Computer Program for Earthquake Analysis of Concrete Gravity Dams," by Fenves, G. and Chopra, A.K., August 1984, (PB85 193 613/AS)A05.
- UCB/EERC-84/12 "A Refined Physical Theory Model for Predicting the Seismic Behavior of Braced Steel Frames," by Ikeda, K. and Mahin, S.A., July 1984, (PB85 191 450/AS)A09.
- UCB/EERC-84/13 "Earthquake Engineering Research at Berkeley - 1984," by EERC, August 1984, (PB85 197 341/AS)A10.
- UCB/EERC-84/14 "Moduli and Damping Factors for Dynamic Analyses of Cohesionless Soils," by Seed, H.B., Wong, R.T., Idriss, I.M. and Tokimatsu, K., September 1984, (PB85 191 468/AS)A04.
- UCB/EERC-84/15 "The Influence of SPT Procedures in Soil Liquefaction Resistance Evaluations," by Seed, H.B., Tokimatsu, K., Harder, L.F. and Chung, R.M., October 1984, (PB85 191 732/AS)A04.
- UCB/EERC-84/16 "Simplified Procedures for the Evaluation of Settlements in Sands Due to Earthquake Shaking," by Tokimatsu, K. and Seed, H.B., October 1984, (PB85 197 887/AS)A03.
- UCB/EERC-84/17 "Evaluation of Energy Absorption Characteristics of Highway Bridges Under Seismic Conditions - Volume I (PB90 262 627)A16 and Volume II (Appendices) (PB90 262 635)A13," by Imbsen, R.A. and Penzien, J., September 1986.
- UCB/EERC-84/18 "Structure-Foundation Interactions under Dynamic Loads," by Liu, W.D. and Penzien, J., November 1984, (PB87 124 889/AS)A11.
- UCB/EERC-84/19 "Seismic Modelling of Deep Foundations," by Chen, C.-H. and Penzien, J., November 1984, (PB87 124 798/AS)A07.
- UCB/EERC-84/20 "Dynamic Response Behavior of Quan Shui Dam," by Clough, R.W., Chang, K.-T., Chen, H.-Q., Stephen, R.M., Ghanaat, Y. and Qi, J.-H., November 1984, (PB86 115177/AS)A07.
- UCB/EERC-85/01 "Simplified Methods of Analysis for Earthquake Resistant Design of Buildings," by Cruz, E.F. and Chopra, A.K., February 1985, (PB86 112299/AS)A12.
- UCB/EERC-85/02 "Estimation of Seismic Wave Coherency and Rupture Velocity using the SMART 1 Strong-Motion Array Recordings," by Abrahamson, N.A., March 1985, (PB86 214 343)A07.
- UCB/EERC-85/03 "Dynamic Properties of a Thirty Story Condominium Tower Building," by Stephen, R.M., Wilson, E.L. and Stander, N., April 1985, (PB86 118965/AS)A06.
- UCB/EERC-85/04 "Development of Substructuring Techniques for On-Line Computer Controlled Seismic Performance Testing," by Dermitzakis, S. and Mahin, S., February 1985, (PB86 132941/AS)A08.
- UCB/EERC-85/05 "A Simple Model for Reinforcing Bar Anchorages under Cyclic Excitations," by Filippou, F.C., March 1985, (PB86 112 919/AS)A05.
- UCB/EERC-85/06 "Racking Behavior of Wood-framed Gypsum Panels under Dynamic Load," by Oliva, M.G., June 1985, (PB90 262 643)A04.
- UCB/EERC-85/07 "Earthquake Analysis and Response of Concrete Arch Dams," by Fok, K.-L. and Chopra, A.K., June 1985, (PB86 139672/AS)A10.
- UCB/EERC-85/08 "Effect of Inelastic Behavior on the Analysis and Design of Earthquake Resistant Structures," by Lin, J.P. and Mahin, S.A., June 1985, (PB86 135340/AS)A08.
- UCB/EERC-85/09 "Earthquake Simulator Testing of a Base-Isolated Bridge Deck," by Kelly, J.M., Buckle, I.G. and Tsai, H.-C., January 1986, (PB87 124 152/AS)A06.

- UCB/EERC-85/10 "Simplified Analysis for Earthquake Resistant Design of Concrete Gravity Dams," by Fenves, G. and Chopra, A.K., June 1986, (PB87 124 160/AS)A08.
- UCB/EERC-85/11 "Dynamic Interaction Effects in Arch Dams," by Clough, R.W., Chang, K.-T., Chen, H.-Q. and Ghanaat, Y., October 1985, (PB86 135027/AS)A05.
- UCB/EERC-85/12 "Dynamic Response of Long Valley Dam in the Mammoth Lake Earthquake Series of May 25-27, 1980," by Lai, S. and Seed, H.B., November 1985, (PB86 142304/AS)A05.
- UCB/EERC-85/13 "A Methodology for Computer-Aided Design of Earthquake-Resistant Steel Structures," by Austin, M.A., Pister, K.S. and Mahin, S.A., December 1985, (PB86 159480/AS)A10.
- UCB/EERC-85/14 "Response of Tension-Leg Platforms to Vertical Seismic Excitations," by Liou, G.-S., Penzien, J. and Yeung, R.W., December 1985, (PB87 124 871/AS)A08.
- UCB/EERC-85/15 "Cyclic Loading Tests of Masonry Single Piers: Volume 4 - Additional Tests with Height to Width Ratio of 1," by Sveinsson, B., McNiven, H.D. and Sucuoglu, H., December 1985.
- UCB/EERC-85/16 "An Experimental Program for Studying the Dynamic Response of a Steel Frame with a Variety of Infill Partitions," by Yanev, B. and McNiven, H.D., December 1985, (PB90 262 676)A05.
- UCB/EERC-86/01 "A Study of Seismically Resistant Eccentrically Braced Steel Frame Systems," by Kasai, K. and Popov, E.P., January 1986, (PB87 124 178/AS)A14.
- UCB/EERC-86/02 "Design Problems in Soil Liquefaction," by Seed, H.B., February 1986, (PB87 124 186/AS)A03.
- UCB/EERC-86/03 "Implications of Recent Earthquakes and Research on Earthquake-Resistant Design and Construction of Buildings," by Bertero, V.V., March 1986, (PB87 124 194/AS)A05.
- UCB/EERC-86/04 "The Use of Load Dependent Vectors for Dynamic and Earthquake Analyses," by Leger, P., Wilson, E.L. and Clough, R.W., March 1986, (PB87 124 202/AS)A12.
- UCB/EERC-86/05 "Two Beam-To-Column Web Connections," by Tsai, K.-C. and Popov, E.P., April 1986, (PB87 124 301/AS)A04.
- UCB/EERC-86/06 "Determination of Penetration Resistance for Coarse-Grained Soils using the Becker Hammer Drill," by Harder, L.F. and Seed, H.B., May 1986, (PB87 124 210/AS)A07.
- UCB/EERC-86/07 "A Mathematical Model for Predicting the Nonlinear Response of Unreinforced Masonry Walls to In-Plane Earthquake Excitations," by Mengi, Y. and McNiven, H.D., May 1986, (PB87 124 780/AS)A06.
- UCB/EERC-86/08 "The 19 September 1985 Mexico Earthquake: Building Behavior," by Bertero, V.V., July 1986.
- UCB/EERC-86/09 "EACD-3D: A Computer Program for Three-Dimensional Earthquake Analysis of Concrete Dams," by Fok, K.-L., Hall, J.F. and Chopra, A.K., July 1986, (PB87 124 228/AS)A08.
- UCB/EERC-86/10 "Earthquake Simulation Tests and Associated Studies of a 0.3-Scale Model of a Six-Story Concentrically Braced Steel Structure," by Uang, C.-M. and Bertero, V.V., December 1986, (PB87 163 564/AS)A17.
- UCB/EERC-86/11 "Mechanical Characteristics of Base Isolation Bearings for a Bridge Deck Model Test," by Kelly, J.M., Buckle, I.G. and Koh, C.-G., November 1987, (PB90 262 668)A04.
- UCB/EERC-86/12 "Effects of Axial Load on Elastomeric Isolation Bearings," by Koh, C.-G. and Kelly, J.M., November 1987.
- UCB/EERC-87/01 "The FPS Earthquake Resisting System: Experimental Report," by Zayas, V.A., Low, S.S. and Mahin, S.A., June 1987.
- UCB/EERC-87/02 "Earthquake Simulator Tests and Associated Studies of a 0.3-Scale Model of a Six-Story Eccentrically Braced Steel Structure," by Whitaker, A., Uang, C.-M. and Bertero, V.V., July 1987.
- UCB/EERC-87/03 "A Displacement Control and Uplift Restraint Device for Base-Isolated Structures," by Kelly, J.M., Griffith, M.C. and Aiken, I.D., April 1987.
- UCB/EERC-87/04 "Earthquake Simulator Testing of a Combined Sliding Bearing and Rubber Bearing Isolation System," by Kelly, J.M. and Chalhoub, M.S., 1987.
- UCB/EERC-87/05 "Three-Dimensional Inelastic Analysis of Reinforced Concrete Frame-Wall Structures," by Moazzami, S. and Bertero, V.V., May 1987.
- UCB/EERC-87/06 "Experiments on Eccentrically Braced Frames with Composite Floors," by Ricles, J. and Popov, E., June 1987.
- UCB/EERC-87/07 "Dynamic Analysis of Seismically Resistant Eccentrically Braced Frames," by Ricles, J. and Popov, E., June 1987.
- UCB/EERC-87/08 "Undrained Cyclic Triaxial Testing of Gravels-The Effect of Membrane Compliance," by Evans, M.D. and Seed, H.B., July 1987.
- UCB/EERC-87/09 "Hybrid Solution Techniques for Generalized Pseudo-Dynamic Testing," by Thewalt, C. and Mahin, S.A., July 1987.
- UCB/EERC-87/10 "Ultimate Behavior of Butt Welded Splices in Heavy Rolled Steel Sections," by Bruneau, M., Mahin, S.A. and Popov, E.P., September 1987.
- UCB/EERC-87/11 "Residual Strength of Sand from Dam Failures in the Chilean Earthquake of March 3, 1985," by De Alba, P., Seed, H.B., Retamal, E. and Seed, R.B., September 1987.
- UCB/EERC-87/12 "Inelastic Seismic Response of Structures with Mass or Stiffness Eccentricities in Plan," by Bruneau, M. and Mahin, S.A., September 1987, (PB90 262 650)A14.
- UCB/EERC-87/13 "CSTRUCT: An Interactive Computer Environment for the Design and Analysis of Earthquake Resistant Steel Structures," by Austin, M.A., Mahin, S.A. and Pister, K.S., September 1987.
- UCB/EERC-87/14 "Experimental Study of Reinforced Concrete Columns Subjected to Multi-Axial Loading," by Low, S.S. and Moehle, J.P., September 1987.
- UCB/EERC-87/15 "Relationships between Soil Conditions and Earthquake Ground Motions in Mexico City in the Earthquake of Sept. 19, 1985," by Seed, H.B., Romo, M.P., Sun, J., Jaime, A. and Lysmer, J., October 1987.
- UCB/EERC-87/16 "Experimental Study of Seismic Response of R. C. Setback Buildings," by Shahrooz, B.M. and Moehle, J.P., October 1987.

- UCB/EERC-87/17 "The Effect of Slabs on the Flexural Behavior of Beams," by Pantazopoulou, S.J. and Moehle, J.P., October 1987, (PB90 262 700)A07.
- UCB/EERC-87/18 "Design Procedure for R-FBI Bearings," by Mostaghel, N. and Kelly, J.M., November 1987, (PB90 262 718)A04.
- UCB/EERC-87/19 "Analytical Models for Predicting the Lateral Response of R C Shear Walls: Evaluation of their Reliability," by Vulcano, A. and Bertero, V.V., November 1987.
- UCB/EERC-87/20 "Earthquake Response of Torsionally-Coupled Buildings," by Hejal, R. and Chopra, A.K., December 1987.
- UCB/EERC-87/21 "Dynamic Reservoir Interaction with Monticello Dam," by Clough, R.W., Ghanaat, Y. and Qiu, X-F., December 1987.
- UCB/EERC-87/22 "Strength Evaluation of Coarse-Grained Soils," by Siddiqi, F.H., Seed, R.B., Chan, C.K., Seed, H.B. and Pyke, R.M., December 1987.
- UCB/EERC-88/01 "Seismic Behavior of Concentrically Braced Steel Frames," by Khatib, I., Mahin, S.A. and Pister, K.S., January 1988.
- UCB/EERC-88/02 "Experimental Evaluation of Seismic Isolation of Medium-Rise Structures Subject to Uplift," by Griffith, M.C., Kelly, J.M., Coveney, V.A. and Koh, C.G., January 1988.
- UCB/EERC-88/03 "Cyclic Behavior of Steel Double Angle Connections," by Astaneh-Asl, A. and Nader, M.N., January 1988.
- UCB/EERC-88/04 "Re-evaluation of the Slide in the Lower San Fernando Dam in the Earthquake of Feb. 9, 1971," by Seed, H.B., Seed, R.B., Harder, L.F. and Jong, H.-L., April 1988.
- UCB/EERC-88/05 "Experimental Evaluation of Seismic Isolation of a Nine-Story Braced Steel Frame Subject to Uplift," by Griffith, M.C., Kelly, J.M. and Aiken, I.D., May 1988.
- UCB/EERC-88/06 "DRAIN-2DX User Guide.," by Allahabadi, R. and Powell, G.H., March 1988.
- UCB/EERC-88/07 "Theoretical and Experimental Studies of Cylindrical Water Tanks in Base-Isolated Structures," by Chalhoub, M.S. and Kelly, J.M., April 1988.
- UCB/EERC-88/08 "Analysis of Near-Source Waves: Separation of Wave Types using Strong Motion Array Recordings," by Darragh, R.B., June 1988.
- UCB/EERC-88/09 "Alternatives to Standard Mode Superposition for Analysis of Non-Classically Damped Systems," by Kusainov, A.A. and Clough, R.W., June 1988.
- UCB/EERC-88/10 "The Landslide at the Port of Nice on October 16, 1979," by Seed, H.B., Seed, R.B., Schlosser, F., Blondeau, F. and Juran, I., June 1988.
- UCB/EERC-88/11 "Liquefaction Potential of Sand Deposits Under Low Levels of Excitation," by Carter, D.P. and Seed, H.B., August 1988.
- UCB/EERC-88/12 "Nonlinear Analysis of Reinforced Concrete Frames Under Cyclic Load Reversals," by Filiippou, F.C. and Issa, A., September 1988.
- UCB/EERC-88/13 "Implications of Recorded Earthquake Ground Motions on Seismic Design of Building Structures," by Uang, C.-M. and Bertero, V.V., November 1988.
- UCB/EERC-88/14 "An Experimental Study of the Behavior of Dual Steel Systems," by Whittaker, A.S., Uang, C.-M. and Bertero, V.V., September 1988.
- UCB/EERC-88/15 "Dynamic Moduli and Damping Ratios for Cohesive Soils," by Sun, J.I., Golezorkhi, R. and Seed, H.B., August 1988.
- UCB/EERC-88/16 "Reinforced Concrete Flat Plates Under Lateral Load: An Experimental Study Including Biaxial Effects," by Pan, A. and Moehle, J., October 1988.
- UCB/EERC-88/17 "Earthquake Engineering Research at Berkeley - 1988," by EERC, November 1988.
- UCB/EERC-88/18 "Use of Energy as a Design Criterion in Earthquake-Resistant Design," by Uang, C.-M. and Bertero, V.V., November 1988.
- UCB/EERC-88/19 "Steel Beam-Column Joints in Seismic Moment Resisting Frames," by Tsai, K.-C. and Popov, E.P., November 1988.
- UCB/EERC-88/20 "Base Isolation in Japan, 1988," by Kelly, J.M., December 1988.
- UCB/EERC-89/01 "Behavior of Long Links in Eccentrically Braced Frames," by Engelhardt, M.D. and Popov, E.P., January 1989.
- UCB/EERC-89/02 "Earthquake Simulator Testing of Steel Plate Added Damping and Stiffness Elements," by Whittaker, A., Bertero, V.V., Alonso, J. and Thompson, C., January 1989.
- UCB/EERC-89/03 "Implications of Site Effects in the Mexico City Earthquake of Sept. 19, 1985 for Earthquake-Resistant Design Criteria in the San Francisco Bay Area of California," by Seed, H.B. and Sun, J.I., March 1989.
- UCB/EERC-89/04 "Earthquake Analysis and Response of Intake-Outlet Towers," by Goyal, A. and Chopra, A.K., July 1989.
- UCB/EERC-89/05 "The 1985 Chile Earthquake: An Evaluation of Structural Requirements for Bearing Wall Buildings," by Wallace, J.W. and Moehle, J.P., July 1989.
- UCB/EERC-89/06 "Effects of Spatial Variation of Ground Motions on Large Multiply-Supported Structures," by Hao, H., July 1989.
- UCB/EERC-89/07 "EADAP - Enhanced Arch Dam Analysis Program: Users's Manual," by Ghanaat, Y. and Clough, R.W., August 1989.
- UCB/EERC-89/08 "Seismic Performance of Steel Moment Frames Plastically Designed by Least Squares Stress Fields," by Ohi, K. and Mahin, S.A., August 1989.
- UCB/EERC-89/09 "Feasibility and Performance Studies on Improving the Earthquake Resistance of New and Existing Buildings Using the Friction Pendulum System," by Zayas, V., Low, S., Mahin, S.A. and Bozzo, L., July 1989.
- UCB/EERC-89/10 "Measurement and Elimination of Membrane Compliance Effects in Undrained Triaxial Testing," by Nicholson, P.G., Seed, R.B. and Anwar, H., September 1989.
- UCB/EERC-89/11 "Static Tilt Behavior of Unanchored Cylindrical Tanks," by Lau, D.T. and Clough, R.W., September 1989.
- UCB/EERC-89/12 "ADAP-88: A Computer Program for Nonlinear Earthquake Analysis of Concrete Arch Dams," by Fenves, G.L., Mojtahedi, S. and Reimer, R.B., September 1989.
- UCB/EERC-89/13 "Mechanics of Low Shape Factor Elastomeric Seismic Isolation Bearings," by Aiken, I.D., Kelly, J.M. and Tajirian, F.F., November 1989.
- UCB/EERC-89/14 "Preliminary Report on the Seismological and Engineering Aspects of the October 17, 1989 Santa Cruz (Loma Prieta) Earthquake," by EERC, October 1989.

- UCB/EERC-89/15 "Experimental Studies of a Single Story Steel Structure Tested with Fixed, Semi-Rigid and Flexible Connections," by Nader, M.N. and Astaneh-Asl, A., August 1989.
- UCB/EERC-89/16 "Collapse of the Cypress Street Viaduct as a Result of the Loma Prieta Earthquake," by Nims, D.K., Miranda, E., Aiken, I.D., Whitaker, A.S. and Bertero, V.V., November 1989.
- UCB/EERC-90/01 "Mechanics of High-Shape Factor Elastomeric Seismic Isolation Bearings," by Kelly, J.M., Aiken, I.D. and Tajirian, F.F., March 1990.
- UCB/EERC-90/02 "Javid's Paradox: The Influence of Preform on the Modes of Vibrating Beams," by Kelly, J.M., Sackman, J.L. and Javid, A., May 1990.
- UCB/EERC-90/03 "Earthquake Simulator Testing and Analytical Studies of Two Energy-Absorbing Systems for Multistory Structures," by Aiken, I.D. and Kelly, J.M., October 1990.
- UCB/EERC-90/04 "Damage to the San Francisco-Oakland Bay Bridge During the October 17, 1989 Earthquake," by Astaneh, A., June 1990.
- UCB/EERC-90/05 "Preliminary Report on the Principal Geotechnical Aspects of the October 17, 1989 Loma Prieta Earthquake," by Seed, R.B., Dickenson, S.E., Riemer, M.F., Bray, J.D., Sitar, N., Mitchell, J.K., Idriss, I.M., Kayen, R.E., Kropp, A., Harder, L.F., Jr. and Power, M.S., April 1990.
- UCB/EERC-90/06 "Models of Critical Regions in Reinforced Concrete Frames Under Seismic Excitations," by Zulfiqar, N. and Filippou, F., May 1990.
- UCB/EERC-90/07 "A Unified Earthquake-Resistant Design Method for Steel Frames Using ARMA Models," by Takewaki, I., Conte, J.P., Mahin, S.A. and Pister, K.S., June 1990.
- UCB/EERC-90/08 "Soil Conditions and Earthquake Hazard Mitigation in the Marina District of San Francisco," by Mitchell, J.K., Masood, T., Kayen, R.E. and Seed, R.B., May 1990.
- UCB/EERC-90/09 "Influence of the Earthquake Ground Motion Process and Structural Properties on Response Characteristics of Simple Structures," by Conte, J.P., Pister, K.S. and Mahin, S.A., July 1990.
- UCB/EERC-90/10 "Experimental Testing of the Resilient-Friction Base Isolation System," by Clark, P.W. and Kelly, J.M., July 1990.
- UCB/EERC-90/11 "Seismic Hazard Analysis: Improved Models, Uncertainties and Sensitivities," by Araya, R. and Der Kiureghian, A., March 1988.
- UCB/EERC-90/12 "Effects of Torsion on the Linear and Nonlinear Seismic Response of Structures," by Sedarat, H. and Bertero, V.V., September 1989.
- UCB/EERC-90/13 "The Effects of Tectonic Movements on Stresses and Deformations in Earth Embankments," by Bray, J. D., Seed, R. B. and Seed, H. B., September 1989.
- UCB/EERC-90/14 "Inelastic Seismic Response of One-Story, Asymmetric-Plan Systems," by Goel, R.K. and Chopra, A.K., October 1990.
- UCB/EERC-90/15 "Dynamic Crack Propagation: A Model for Near-Field Ground Motion," by Seyyedian, H. and Kelly, J.M., 1990.
- UCB/EERC-90/16 "Sensitivity of Long-Period Response Spectra to System Initial Conditions," by Blasquez, R., Ventura, C. and Kelly, J.M., 1990.
- UCB/EERC-90/17 "Behavior of Peak Values and Spectral Ordinates of Near-Source Strong Ground-Motion over a Dense Array," by Niazi, M., June 1990.
- UCB/EERC-90/18 "Material Characterization of Elastomers used in Earthquake Base Isolation," by Papoulia, K.D. and Kelly, J.M., 1990.
- UCB/EERC-90/19 "Cyclic Behavior of Steel Top-and-Bottom Plate Moment Connections," by Harriott, J.D. and Astaneh, A., August 1990.
- UCB/EERC-90/20 "Seismic Response Evaluation of an Instrumented Six Story Steel Building," by Shen, J.-H. and Astaneh, A., December 1990.
- UCB/EERC-90/21 "Observations and Implications of Tests on the Cypress Street Viaduct Test Structure," by Bollo, M., Mahin, S.A., Moehle, J.P., Stephen, R.M. and Qi, X., December 1990.
- UCB/EERC-91/01 "Experimental Evaluation of Nitinol for Energy Dissipation in Structures," by Nims, D.K., Sasaki, K.K. and Kelly, J.M., 1991.
- UCB/EERC-91/02 "Displacement Design Approach for Reinforced Concrete Structures Subjected to Earthquakes," by Qi, X. and Moehle, J.P., January 1991.
- UCB/EERC-91/03 "Shake Table Tests of Long Period Isolation System for Nuclear Facilities at Soft Soil Sites," by Kelly, J.M., March 1991.
- UCB/EERC-91/04 "Dynamic and Failure Characteristics of Bridgestone Isolation Bearings," by Kelly, J.M., April 1991.
- UCB/EERC-91/05 "Base Sliding Response of Concrete Gravity Dams to Earthquakes," by Chopra, A.K. and Zhang, L., May 1991.
- UCB/EERC-91/06 "Computation of Spatially Varying Ground Motion and Foundation-Rock Impedance Matrices for Seismic Analysis of Arch Dams," by Zhang, L. and Chopra, A.K., May 1991.
- UCB/EERC-91/07 "Estimation of Seismic Source Processes Using Strong Motion Array Data," by Chiou, S.-J., July 1991.